Natural Resources Canada | Ressources naturelles Canada

GEOLOGICAL SURVEY OF CANADA
OPEN FILE 8763

Mineralogical properties of Champlain Sea sediments and their effects on borehole geophysical logs, western Quebec

H.L. Crow, R.J. Enkin, J.B. Percival, and O.N. Al-Mufti

2021

Canada

GEOLOGICAL SURVEY OF CANADA
OPEN FILE 8763

Mineralogical properties of Champlain Sea sediments and their effects on borehole geophysical logs, western Quebec

H.L. Crow[1], R.J. Enkin[2], J.B. Percival[1], and O.N. Al-Mufti[3]

[1]Geological Survey of Canada, 601 Booth Street, Ottawa, Ontario
[2]Geological Survey of Canada, 9860 West Saanich Road, Sidney, British Columbia
[3]Department of Earth and Environmental Sciences, University of Ottawa, 150 Louis-Pasteur Private, Ottawa, Ontario

2021

Permanent link: https://doi.org/10.4095/327855

This publication is available for free download through GEOSCAN (https://geoscan.nrcan.gc.ca/).

Recommended citation
Crow, H.L., Enkin, R.J., Percival, J.B., and Al-Mufti, O.N., 2021. Mineralogical properties of Champlain Sea sediments and their effects on borehole geophysical logs, western Quebec; Geological Survey of Canada, Open File 8763, 72 p. https://doi.org/10.4095/327855

Publications in this series have not been edited; they are released as submitted by the author.

ABSTRACT

The Geological Survey of Canada is conducting geoscientific investigations in Breckenridge Creek Valley (Municipality of Pontiac, western Quebec) where ancient and modern landslides have occurred in the fine-grained, post-glacial sediments of the former Champlain Sea. Multidisciplinary studies aim to gain a better understanding of how these sediments respond to earthquake shaking, and what factors increase their susceptibility to retrogressive landslides. As part of these investigations, downhole geophysical logs collected in a 75-m borehole displayed relatively low and unvarying gamma-ray responses, downward increasing density and velocity trends, and variable magnetic susceptibility responses. Laboratory analyses of existing cores were undertaken to better understand these geophysical log responses, and relate them to depositional and post-depositional characteristics of the sediments.

The relatively low gamma log responses were found to result from the low quantities of potassium-bearing clay minerals. While clay-size grains made up 30 – 57% by volume of the samples tested, X-ray diffraction analyses revealed clay minerals made up only 20 – 45% by weight of the clay-size fraction.

Polished thin sections were prepared from three core samples at the top, middle, and bottom of the borehole. Scanning electron microscopy (SEM) imaged diverse grain orientations, sizes, and textures in each of these intervals, and evidence for compaction was observed in the middle sample where biotite grains were observed to be aligned around larger grains. A downhole trend of increasing bulk density and shear wave velocity is primarily accounted for by a relatively consistent grain density and a reduction in water content with depth as pore water was expelled by compaction under the weight of the overlying sediment column.

Concentration and grain size of magnetic minerals influence magnetic susceptibility and nuclear magnetic resonance (NMR) log responses, but little was known about these properties as the minerals are present at trace levels (<3%). Magnetic properties of iron oxides in clay- to silt-size grains were examined in seven core samples using a coercivity spectrometer and a thermomagnetic susceptibility meter in step-wise heating experiments. Results indicate that magnetite is present in varying concentrations and grain sizes in all samples tested, ranging from silt- and clay-size detrital particles down to nanoparticles. The presence of superparamagnetic nanoparticles identified in the three lower-most samples in the borehole coincided with an observed shortening of downhole NMR relaxation times.

This Open File Report summarizes the laboratory methods and datasets resulting from new analyses of sediment cores, and discusses the results in the context of the geophysical log responses. New insights on broader sedimentological and geochemical conditions in Champlain Sea sediments are also discussed.

TABLE OF CONTENTS

INTRODUCTION

In 2010, the Geological Survey of Canada (GSC) began conducting geophysical investigations in western Quebec in the municipality of Pontiac. A study area was established in the Breckenridge Creek Valley where numerous landslides, both ancient and modern, have been identified in the fine-grained Champlain Sea sediments of the region (e.g. Eden and Mitchell, 1970; Mitchell, 1970; Brooks et al., 2013). Four of these landslides in the study area have the age signature of a paleoseismic event ~1020 calibrated years before present (Brooks, 2013), indicating that the sediments are susceptible to earthquake-triggered ground failure. Additionally, the low shear wave velocities of these soft sediments, which overlie high velocity bedrock, create conditions leading to significant amplification of earthquake shaking (e.g. Kramer, 1996; Hunter et al., 2010; Crow et al., 2011; Khaheshi Banab et al., 2012).

The GSC studies investigated geophysical, geotechnical, and geochemical properties of the sediments, and the shape of the underlying bedrock basin. Surface geophysical surveys allowed for the selection of a drilling site near the centre of a bedrock basin, where a 75-m borehole was advanced for geophysical logging and undisturbed sediment sample recovery. The purpose of this multidisciplinary approach was to gain a better understanding of how the sediments might respond to earthquake shaking, and how hydrogeological/hydrogeochemical factors affect the development of geotechnical sensitivity, which leads to increased susceptibility to retrogressive landslides (Torrance, 1979; L'Heureux et al., 2013; Hinton and Alpay, 2020). Summaries of the geophysical surveys, borehole drilling, sediment sampling, and subsequent lab analyses of cores are provided in Crow et al. (2017).

Since these results were released in Crow et al. (2017), new analyses of mineralogy and grain texture have been undertaken to relate geophysical log responses in fine-grained Champlain Sea deposits to depositional and post-depositional characteristics of the sediments. A trend of increasing log density with depth, coupled with decreasing water content, was interpreted primarily as evidence of compaction as pore fluids were expelled by the weight of the overlying sediment column. To explore this idea, polished thin sections were prepared from cores collected at the top, middle, and bottom of the borehole to investigate grain mineralogy, shape, and orientation under a scanning electron microscope (SEM). Gamma-ray logs collect relatively low and unvarying responses in the fine-grained Champlain Sea sediments, prompting a new analysis of the types and abundance of clay minerals in the clay-size fraction (<2 μm) using X-ray diffraction (XRD) analyses. Conversely, relatively elevated magnetic susceptibility log responses were recorded downhole, but iron oxides are below XRD detection limits of about 3%, providing little information about magnetic mineral type and grain size distribution. Seven samples were selected for sediment magnetism analyses to investigate the mineralogy, grain size, and relative abundances of ferromagnetic minerals in the silt and clay fractions (<63 μm). These results support recent downhole experiments in Champlain Sea sediments using newly developed slim-hole nuclear magnetic resonance (NMR) tools, which require an understanding of the magnetic mineralogy and grain size in the sediment profile (Crow et al., 2020). Additionally, the presence of magnetite nanoparticles as a potential cementation agent has been recently revived in discussion, creating a renewed call to understand the role magnetite may play in sediment behaviour (Sangrey, 1972; Torrance, 2017).

This open file summarizes the laboratory methods and the datasets resulting from new analyses of Champlain Sea sediments from a borehole in Breckenridge Valley, Quebec. The results provide insight into the geophysical log responses, and more broadly, into the sedimentological and mineralogical properties of Champlain Sea sediments. These new datasets are contributing to ongoing research into the hydrogeological and hydrogeochemical conditions that influence sediment stability and landslide susceptibility.

GEOLOGICAL SETTING

The Champlain Sea formed an ice marginal glaciomarine setting following retreat of the Laurentide ice sheet when the continent was isostatically depressed (Figure 1A). Marine water extended westward from the north Atlantic during 11,500 - 10,000 ^{14}C years BP (Anderson, 1988) and millions of cubic meters of silt and clay (mud) were deposited from meltwater as the glaciers retreated. As the crust rebounded, the sea retreated (Rust and Romanelli, 1975) with a subsequent transition from glaciomarine conditions to the fluvial estuary of the early Ottawa and St. Lawrence rivers (MacPherson, 1968).

Paleozoic carbonate is the predominant subcropping bedrock under much of the Champlain Sea basin (Armstrong and Dodge, 2007), with the Precambrian Shield forming the northern border of the basin. A relatively thin veneer of till overlies the bedrock, which is typically 4 m thick (Hunter et al., 2010). Within the overlying glaciomarine Champlain Sea sediments, several units are identified which reflect (from bottom to top) an upward fining rhythmite sequence containing sand; a massive, grey, mud sequence; and an upward coarsening grey and red mud rhythmite sequence (Gadd, 1986; Percival et al., 2003; Cummings et al., 2011; Medioli et al., 2012).

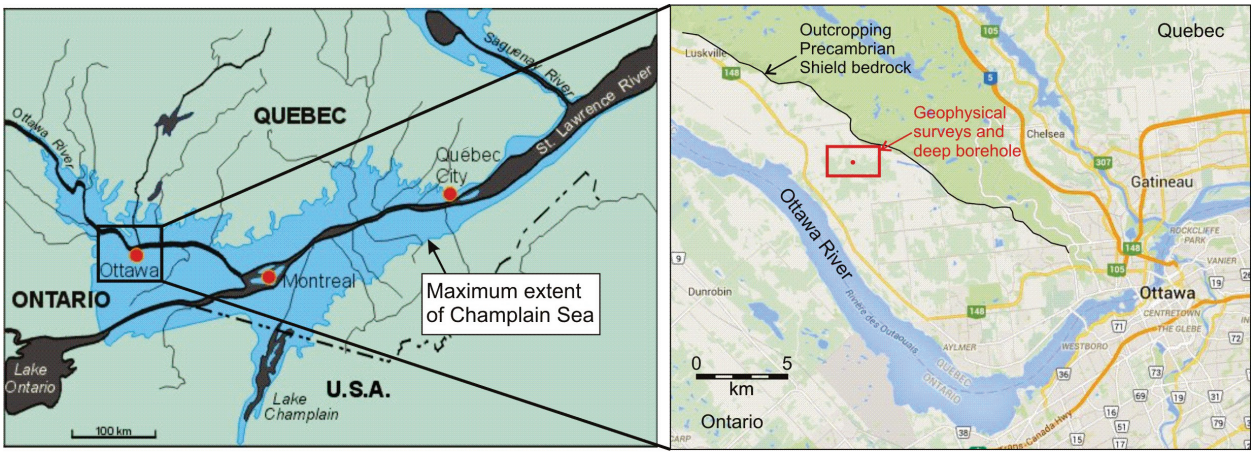

Figure 1. (A) Extent of the proglacial Champlain Sea in which fine-grained glaciomarine sediments were deposited throughout the Ottawa and St. Lawrence valleys in eastern Ontario and western Quebec. (B) The study site in the Breckenridge Valley of western Quebec is located within the western arm of the former sea basin near Ottawa, ON.

Breckenridge Creek Valley borehole

The deep borehole in the study area (GSC-BH-BRK-03) is located about 1.5 km from the outcropping Precambrian Shield (locally termed the Eardley Escarpment) in the western arm of

the Champlain Sea basin (Figure 1B). Sediment samples were collected using an Osterberg hydraulic piston, recovering 76 mm-diameter undisturbed cores in thin-walled Shelby tubes at 3-m intervals to a depth of 63.90 m. Due to the increasing presence of sand at that depth, sampling and flushing were stopped and drill rods were slowly advanced, carefully assessing for indications of artesian conditions. The borehole was deepened to 75 m and a PVC casing was installed for geophysical logging.

Downhole logging techniques included gamma (natural gamma and gamma-gamma density), induction (apparent bulk electrical conductivity and magnetic susceptibility), and downhole seismic (shear wave velocity). In 2018, an experimental downhole nuclear magnetic resonance (NMR) survey was also conducted to measure *in situ* porosity. These logs are presented in Figure 2 and include an interpretation of well completion conditions to indicate where the gamma, magnetic susceptibility, and NMR logs were influenced by an increased thickness of grout around the casing in the upper 22 m. Descriptions of the drilling and downhole logging techniques can be found in Crow et al. (2017), and the subsequent NMR surveys in Crow et al. (2020).

Sediment cores, labeled Segments 1 to 23, were subsampled and tested in the laboratory for grain size, gravimetric water content, Atterberg limits, and shear strengths using a fall cone. Pore water was centrifuged from subsamples for measurements of fluid conductivity, ionic concentration of sea water ions, and isotopic ratios. XRD analyses were conducted on subsamples from the top, middle, and bottom of the borehole to examine sediment mineralogy of the muds (Table 1). Results of these lab analyses are presented in Crow et al. (2017). Measurement of overconsolidation ratio was completed by Duguay-Blanchette (2016).

The multidisciplinary datasets collected from this borehole exemplify the wide range of physical and chemical properties of Champlain Sea sediments in the Ottawa Valley. Core and downhole geophysical data are presented together in Figure 2, with key properties summarized below:

Gravimetric water content: Gravimetric water contents measured on cores (ratio of mass of water to mass of dry sediment) ranged from 40 - 99%, generally decreasing with depth. The water content shows an inverse relationship with density (1.5 – 2.0 g/cm^3) and shear wave velocity (80 – 375 m/s). Within intervals in the upper 30 m of the borehole, the water content exceeds the liquid limit, indicating the sediment may behave as a liquid when disturbed. The large retrogressive landslides around the Breckenridge Creek Valley provide empirical evidence of this occurrence. Volumetric water contents (porosities in saturated conditions below the water table at ~5 m depth) were calculated from the gravimetric water contents using a specific gravity of 2.76 (measured during the current study). Core porosities ranged from 52% to 73%.

NMR volumetric water content: NMR logs were collected in this, and three other plastic-cased boreholes, to evaluate the performance of newly developed slim-hole NMR tools in Champlain Sea muds. Downhole NMR measures the decay (or relaxation) time of hydrogen proton spins in pore fluids when subjected to varying magnetic fields generated by a radio-frequency antenna in the tool. The initial amplitude and decay time of the measured signal allows for the calculation of total volumetric water content (porosity in saturated sediments) and estimation of other hydrogeological parameters. For details of the physics and technology of NMR measurements, readers are referred to books by Coates et al. (1999) and Dunn et al. (2002). The NMR and core

porosities were generally in good agreement (± 5% porosity) where the borehole was not affected by (1) well completion issues or (2) elevated internal magnetic gradients interpreted below 56 m.

Sensitivity: Geotechnical sensitivity of a sediment is defined as the ratio of its remoulded to undisturbed strengths (Skempton and Northey, 1952). Fall cone testing of the Breckenridge samples indicated a sensitivity range of 5 to 42. By the standards of the Canadian Foundation Engineering Manual (CFEM, 2006), sediments at the site are within the ranges of high and medium sensitivities in the near surface (8 – 18 m depth) where the water content exceeds the liquid limits, and medium to low sensitivities below 20 m depth. Sediments in the surface crust (<5 m depth) are of low to medium-low sensitivity. Isotopic studies are underway at this and other borehole sites intersecting Champlain Sea muds near Ottawa to investigate the evolution of pore water geochemistry and its influence on sediment sensitivity (Hinton and Alpay, 2020).

Grain size analyses: Grain size analyses show the sediment samples are predominantly a mix of silt- (2 – 63 μm) and clay-size (≤2 μm) particles (both typically ranging between 30 – 70%). Sand was detected in small amounts in Samples 1 and 2 (5%), and in Samples 15 to 23 (1 – 4%). The sediments examined in the core were massive (lacking visible bedding or laminae) with a dark grey to greenish-grey colour. The sediment is more silt-rich (65 – 70%) in the lower half of the borehole (40 – 65 m) with a higher sand content than in the upper half. Occasionally, heterogeneous fine sand partings are observed in this lower interval. Upward from 40 m, clay and silt are present (both typically 45 – 55%), with negligible sand detected until the top 3 m. The presence of coarser grains (silt and sand) in the lower half of the borehole suggests a more proximal depositional setting, whereas the finer grain sizes (fine silt and clay) in the upper half of the borehole suggest a more distal depositional setting.

Clay and silt mineralogy: The primary minerals in the sediment, as determined from XRD analysis, are plagioclase (35%), biotite (18%), quartz (15%), amphibole (13%), and potassium feldspar (11%). These proportions remain relatively consistent along the borehole (see Table 4). The mineralogy reflects the origin of the sediment as glacial rock flour eroded from granitic-gneissic bedrock of the Precambrian Shield that was transported into the Champlain Sea by meltwater.

Electrical conductivity: The electrical conductivity of the centrifuged pore water increased smoothly from 176 μS/cm at 2.8 m to 38,500 μS/cm at 64.1 m, indicating that pore water in the deepest samples retained a high proportion of relic sea water. Downhole bulk conductivity logs (responding to both sediment grains and pore water) mirror this trend, ranging from 25 mS/m at the top of the hole to 1000 mS/m at 65 m. Below this depth, the conductivity log decreases, indicating that the lowermost core segment represents peak pore water conductivity.

Magnetic susceptibility: The magnetic susceptibility log response increases in the presence of magnetic minerals in the sediments surrounding the borehole. This log, alongside the sand fraction analysis, was used to infer the presence of increasing sand content near the base of the borehole, where heavier (denser) iron oxides are found in greater concentrations than in the fine-grained fraction. However, iron oxides were also seen under the SEM as clay- and silt-size grains, so these logs can also be useful to infer local and regional changes in magnetite content in the fine-grained fraction.

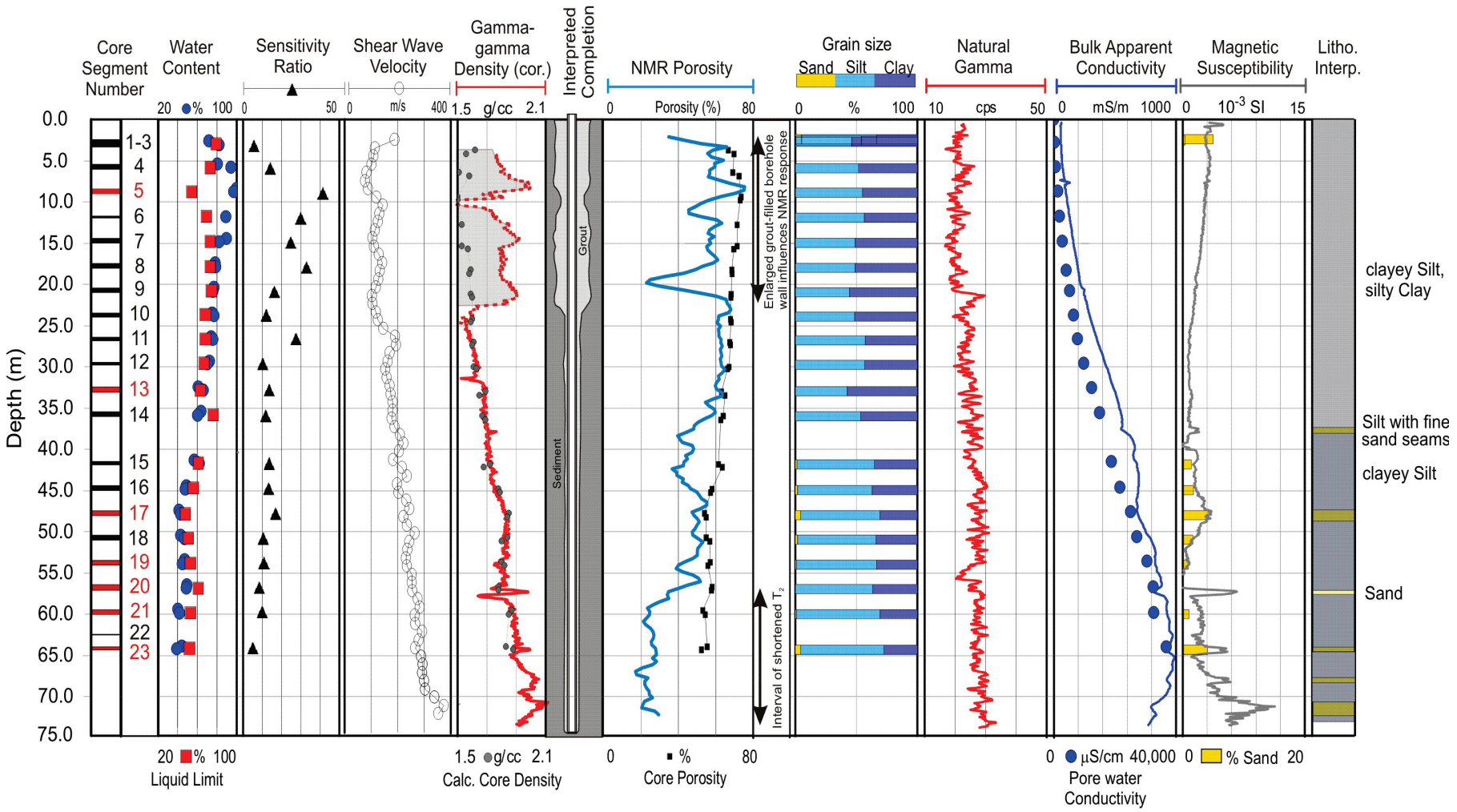

Figure 2. Geophysical logs (continuous lines) shown alongside selected core analyses (discrete points) from borehole GSC-BH-BRK-03. Samples from core segment numbers shown in red were analysed during this study. Grain size measurements of sand are redisplayed at an expanded scale to show the influence of fluctuating sand content on the magnetic susceptibility log. Adapted from Crow et al. (2017, 2020).

LABORATORY METHODS

The following section summarizes the laboratory methods used to investigate the mineralogical and textural properties of selected sediment samples in this study. Depths for all cores tested are provided in Table 1. For brevity, subsamples selected from the core segments are called 'Samples' in the report, and are denoted by the core segment number and their depths in Tables 1 to 4 (e.g., a subsample from core segment 5 would be referred to simply as 'Sample 5' in the text). Sample preparations and specific gravity analyses were performed at the GSC Sedimentology Laboratory in Ottawa, ON. XRD and SEM analyses were conducted at the GSC Mineralogy Laboratories in Ottawa, ON. Magnetism measurements were conducted at the GSC Paleomagnetism and Petrophysics Laboratory in Sidney, BC.

Table 1. Intervals for mineralogical analyses on the Breckenridge borehole cores.

Core Segment	Depth (m)	Analysis Method	Reference
5	8.63	XRD – silt- and clay-size	Crow et al., 2017
13	32.83	XRD – silt- and clay-size	
21	59.61	XRD – silty sand seam	
22	62.42	XRD – silt- and clay-size	
23	64.16	XRD – silty sand seam	
5	8.70	Specific gravity (grain density) (silt- and clay-size)	This publication
13	32.88		
21	59.83		
5	8.80 – 8.87	XRD (clay-size)	
13	32.91 – 32.98		
21	59.86 – 59.93		
5	8.50 – 8.56	SEM - polished thin section (silt- and clay-size)	
13	32.72 - 32.77		
21	59.55 – 59.59		
5	8.63	FE-SEM – coated grain mount (silt- and clay-size)	
13	32.63		
21	59.49		
5	8.87 - 8.90	Magnetic susceptibility and sediment magnetism (silt- and clay-size)	
13	32.88 - 32.91		
17	47.87 - 47.90		
19	53.92 – 53.95		
20	56.95 - 56.98		
21	59.93 - 59.96		
23	64.27 – 64.30		

Sample Preparations

Samples were selected from preserved core segments stored in walk-in soil refrigerators (maintained at 5°C) in the Sedimentology Lab. Selection was based on observations from the geophysical logs suggesting variation in density or mineralogy was occurring in intervals near the sampled cores. Sample preparation for the various physical property analyses were performed by the Sedimentology Lab following procedures outlined in Girard et al. (2004).

Oven drying for specific gravity

Three core samples from the top, middle, and bottom of the borehole (approx. 20 - 30 cm^3) were selected for specific gravity (G_S) analyses. Samples were oven-dried for 24 hours at 105°C, disaggregated, and placed back in the oven until a constant mass was obtained. Specimens were placed into a desiccator until the samples were cooled to room temperature and ready for pycnometer analyses.

Clay-size fractionation for XRD analyses

Three samples of core from the top, middle, and bottom of the borehole were selected as close to the depth intervals of the original XRD measurements as possible. Each sample was prepared by placing it in a stainless steel mixer and adding enough distilled water (DW) to form a slurry. The sample and water were mixed for approximately 30 seconds and allowed to sit for 10 seconds for the sand grains to settle. The suspension was decanted into a 1000 mL centrifuge bottle. Another 250 mL of DW was added to the slurry and the process was repeated two additional times. The bottles were vigorously shaken to suspend all of the sediment and centrifuged at 750 rpm. Bottles were decanted once more and centrifuged a final time at 2800 rpm. The supernatant solution was discarded, and the settled clay fraction (≤ 2 μm) was liquefied and poured into disposable weigh boats. Each wet sample was subsampled and freeze-dried to prepare 'smear' (oriented) mounts for X-ray diffraction analysis.

Thin section preparation for SEM analyses

Three samples of core, representing a variety of physical and chemical properties, were selected from the top, middle, and bottom of the borehole. A 2-cm^3 block was cut from the centre of each undisturbed core, with the stratigraphic top carefully marked. Samples were thoroughly dried in a 110 °C oven for 48 hours. A mixture of 120 g of Petropoxy 154 resin and 13 g of the Petropoxy 154 curing agent (Burnham Petrographics LLC, Rathdrum, Idaho, USA) was prepared. This mixture was painted on each sample block and allowed to soak in, then placed in a 130°C vacuum oven to harden. This process was repeated until no more resin mixture could be absorbed. Samples were then cured for several hours in the vacuum oven before trimming. The impregnated samples were sent to Vancouver Petrographics for polished thin section preparation.

Grain mounts for SEM analyses

Grain mounts were prepared for SEM analyses to verify the presence of trace minerals. A minute amount of the clay-size material was mixed in a vial with DW until the suspension became slightly cloudy. A large drop of the suspension was pipetted onto a carbon-coated stub and allowed to dry overnight. Three additional grain mounts were created by smearing a dab of wet core (silt- and clay-size) on carbon-coated stubs for examination under the Field Emission (FE)-SEM. All mounts were carbon-coated in a Leica EM ACE600 dual filament carbon – palladium coater for examination.

Freeze drying for magnetism analyses

Seven samples were selected for sediment magnetism analyses from intervals of varying downhole magnetic susceptibility response (low, moderate, and elevated). Samples (~2 g/cm^3) were freeze-dried to avoid sample oxidation during drying. As magnetism analyses did not require intact cores, samples of remoulded sediment preserved in a soil fridge in air-tight sediment bags were used. A

small amount of DW was added to each sample to produce a smooth paste in a freeze-drying flask. Each flask was sealed with a rubber cap, gently shaken, and placed in a shell freezer until the sample was frozen. The flasks were then moved into a low-temperature freezer (-50°C) where each flask was placed under a vacuum (of less than 170 x 10^{-3} mBar) for 12 hours. The dried samples were removed from the flasks and transferred to the GSC in Sidney, BC.

Analytical Methods

Specific gravity

Specific gravity (G_S) measures the ratio of the density of mineral grains to the density of water at 20°C. Analyses were performed on oven-dried samples following ASTM-D5550-00 (ASTM, 2014) procedures using the Micromeritics AccuPyc 1330 gas pycnometer (10 cm^3 model). Prior to sample testing, pycnometer chamber O-ring seals were checked, followed by daily volume calibrations using calibration spheres. The tare of a 10 cm^3 sample cup was weighed, and dried sample was transferred into the cup, filling it at least 2/3 full. The cup was wiped clean and reweighed to obtain the sample mass. The sample cup was then sealed inside the pycnometer chamber for volume analysis. The pressure drop that occurred after helium at a known pressure flowed into a second chamber in the pycnometer was related to the volume of sediment in the sample cup, as determined through the calibration procedure. The instrument microprocessor calculated particle density by dividing the mass of the sample by its measured sample volume. G_S was measured by dividing this result by the density of distilled water at 20°C (0.998 g/cm^3).

XRD

The mineralogy of the three samples of clay-size separates was determined by XRD analysis. Clay particles (40 mg samples) were suspended in distilled water, thoroughly agitated using a Vortex mixer, pipetted onto glass slides, and air-dried overnight to produce oriented mounts. X-ray patterns of the samples were recorded on a Bruker D8 Advance Powder Diffractometer equipped with a Lynx-Eye Detector, Co Kα radiation set at 35 kV and 35 mA. The clay-size samples were analysed after air-drying, glycol saturation, and heat treatment (550 °C for 2 hours). Initial identification of minerals was made using EVA (Bruker Nano Inc.) software with comparison to reference mineral patterns using Powder Diffraction Files (PDF) of the International Centre for Diffraction Data (ICDD) and other available databases. Semi-quantitative analyses are provided for the clay-size fraction based on the Reference Intensity Ratio (RIR) method (EVA software; Bruker Nano, Inc.).

SEM

SEM analyses were performed at the GSC Microbeam Laboratory in Ottawa. Preliminary imaging and mineral identification were done on a Zeiss EVO50 variable-pressure SEM fitted with a tungsten filament, with follow-up work performed on a TESCAN Mira3 XMH field emission SEM (FE-SEM). Both instruments are capable of secondary electron (SE), backscattered electron (BSE), and cathodoluminescence (CL) imaging modes, while the Zeiss EVO50 is also equipped with a variable pressure secondary electron (VPSE) detector for imaging of non-conductive samples in extended variable pressure (XVP) mode. Chemical analyses for mineral identification purposes were performed using energy-dispersive X-ray spectroscopy (EDS), with both SEMs equipped with X-Max silicon drift detectors from Oxford Instruments. Analytical conditions used

for EDS analyses included an accelerating voltage of 20 kV, probe currents of 1 nA, and a working distance of 8.5 mm (for the Zeiss SEM) or 15 mm (for the Tescan FE-SEM).

Sediment magnetism

Magnetic susceptibility (MS) measurements were collected on the seven core samples using three different instruments: two handheld meters (GF Instruments SM-20; Geoinstruments JH-8) and one benchtop instrument (the Sapphire SI2B). Measurements using the JH-8 (1 kHz, ~7 cm coil diameter) were collected in the GSC Sedimentology Laboratory using palm-sized bags of wet core, and re-measured following the freeze-drying. Measurements were recorded six times over various parts of each sample and averaged. Freeze-dried samples were then transferred to the GSC Paleomagnetism and Petrophysics Laboratory and re-measured using the SM-20 (10 kHz, 5 cm coil diameter). This is the preferred field-deployable susceptibility meter by the GSC Paleomagnetism and Petrophysics Laboratory due to its smaller coil diameter and higher operating frequency. The samples were then measured in the Sapphire SI2B meter which operates at 19 kHz. It is more sensitive than the field-deployable susceptibility meters, but can only measure samples that can be placed within its 4.5 cm diameter coil. The freeze-dried samples were packed into a 6.3 cm^3 plastic cylinder, and the sediment mass and density were used to calculate the grain susceptibility. This independently measured susceptibility was then used to determine the bulk susceptibility using the nearest core porosity measurement (within 10 cm of the sample depth).

Ferromagnetic mineral content in the sediment samples was interpreted from magnetic hysteresis cycles and isothermal remanence magnetization (IRM) curves measured by a J-Meter coercivity spectrometer (Enkin et al., 2007). Chips of freeze-dried sample (1 - 2 g) were placed in a 7 mm × 10 mm × 22mm box and immobilized with cotton. The box was placed in the instrument's sample holder and spun around a 50 cm acrylic disk at 17.5 Hz through the pole pieces of an electromagnet. During each rotation, the induced magnetism (M_I) and remanence (M_R) were measured by two sets of coils inside the instrument. The magnetic field was slowly ramped up and then down (from ambient to +500 mT, then down to -500 mT) during continuous recording of the hysteresis cycle and the IRM acquisition and remagnetization curves. The curves were analysed in the LabView program JMP, developed in-house for J-Meter data interpretation.

A Bartington MS2WF thermomagnetic susceptibility meter was used to determine Curie temperatures of the magnetic minerals present in the samples. Chips of the freeze-dried samples were placed in a crucible inside a furnace surrounded by a water-cooled susceptibility meter sensor. The furnace was heated to 700°C while MS was continuously monitored. As the Curie temperature of particular minerals was reached and exceeded, or when magnetic minerals were chemically altered by oxidation or reduction, a susceptibility drop was recorded by the meter. The MS was also recorded as the temperature cooled to ambient levels. The temperature profiles were recorded and analysed using LabView software.

To recognize and identify magnetic mineralogical transformations, detailed step-heating experiments were performed on two samples using the Bartington MS2WF. While measuring MS continuously, the furnace was heated up to a suite of increasing temperatures at steps of 100°C or 50°C up to 700°C, and then cooled back to ambient temperature with repeat measurements at each step. The sample in its crucible was weighed between each heating step to quantify the loss of water and other volatiles.

RESULTS

Specific gravity

Results indicate specific gravities (G_S) of the clay- and silt-size fraction remain relatively consistent along the borehole (Table 2). Grain densities are also shown, calculated by multiplying G_S by the density of water (0.99823 g/cm^3 at 20°C).

Table 2. Specific gravity test results using oven-dried samples.

Core Segment	Depth (m)	Specific Gravity at 20 °C	Grain Density (g/cm^3)
5	8.70	2.76	2.76
13	32.88	2.75	2.74
21	59.83	2.77	2.76

These grain densities are consistent with the XRD-measured mineralogy proportions, and fall within the range of densities typical for continental shield rock and eroded orogenic belts (2.6 - 2.8 g/cm^3) (Enkin et al., 2020).

XRD

The objectives of the XRD work were to determine the type and amount of clay minerals present in the clay-size fraction. Results indicate each sample contains a different abundant mineral (Table 3). Sample 5 is dominated by a biotitic illite with subordinate K-feldspar and plagioclase feldspar, minor quartz, amphibole and chlorite and traces of a muscovitic illite. No carbonates were detected. Sample 13 is more abundant in chlorite and plagioclase feldspar, with minor quartz, K-feldspar, amphibole and both biotitic and muscovitic illite. Traces of calcite and dolomite were detected. Sample 21 is dominated by plagioclase feldspar with minor amphibole, biotitic illite, quartz, K-feldspar and chlorite. Traces of carbonate minerals were also detected.

Biotitic illite is differentiated from muscovitic illite by the differences in intensity of the 5 Å X-ray peak. Muscovite is nominally around 50% intensity compared to the 10 Å (100% intensity) X-ray peak, and biotite is 5% intensity. Where the 5 Å peak is more intense than 5%, it is likely a mixture of the two phases.

The diffractogram for Sample 13 is shown in Figure 3 with background removed. Note the intense 10 Å X-ray peak (left-hand side, labelled Ill) and the 5 Å illite peak (~20 degrees 2 Theta) indicating a mixture of biotitic and muscovitic illite. The carbonate minerals, calcite (not labelled) and dolomite, occur in trace amounts. The stacked diffractograms (background not removed) for Sample 5 are shown in Figure 4. There is no evidence for a mixed-layer clay mineral (glycol pattern) and the presence of chlorite is confirmed in the heat-treated pattern with the increase in the 14 Å peak (left-hand side, labelled Chl) and the disappearance of the other chlorite peaks.

The XRD results obtained from the earlier silt- and clay-size fraction analyses (located at slightly different depths in the core segments) indicate similar mineral phases to the clay fraction, but different abundant minerals (Table 4). For example, in Sample 5, plagioclase feldspar is most abundant in the silt- and clay-size fraction, whereas biotitic illite is most abundant in the clay-fraction. When comparing these two datasets, it is important to consider the percentage of the

clay-size grains relative to the total sample. During the clay fractionation, the grain size distribution in each sample was not determined. Therefore, the nearest grain size analysis (performed within 4.5 cm of Samples 5 and 21, and within 7.5 cm from Sample 13) provide guidance on the volume of clay-size particles in relation to the total sample, ranging from 30.5% clay-size in Sample 21, to 57.3% clay-size in Sample 13 (Table 3). These numbers provide insight into the relatively low percentages of clay minerals present in the total sample volumes.

Table 3. Semi-quantitative mineralogy (wt%) of clay-size fraction, smear (oriented) mount samples.

Core Segment	Depth (m)	Qtz	Pl	Kfs	Amp	Ill/Ms	Ill/Bt	Chl	Cal	Dol	% Clay
5	8.80 - 8.87	12	18	19	12	tr	29	10			45.0
13	32.91 – 32.98	10	23	10	11	12	11	22	tr	1	57.3
21	59.86 – 59.93	11	40	11	16		14	6	1	1	30.5

Qtz: quartz; Pl: plagioclase; Kfs: K-feldspar; Amp: amphibole; Ill/Ms: illite (muscovitic); Ill/Bt: illite (biotitic); Chl: chlorite; Cal: calcite; Dol: dolomite; tr: trace; % Clay: volumetric percentage of clay-size grains in total mud sample.

Table 4. Semi-quantitative mineralogy (wt%) of silt- and clay-size fraction, smear (oriented) mount samples (adapted from Crow et al., 2017: Table 9).

Core Segment	Depth (m)	Qtz	Pl	Kfs	Amp	Cpx	Bt	Chl	Cal	FAp	Py
5	8.56 – 8.70	15	32	11	12	3	20	7	tr		
13	32.78 – 32.88	14	35	12	15	3	17	4	tr		
22	62.40 – 62.45	15	37	10	13	3	18	4		tr	tr

Qtz: quartz; Pl: plagioclase; Kfs: K-feldspar; Amp: amphibole; Cpx: clinopyroxene; Bt: biotite; Chl: chlorite; Cal: calcite; FAp: fluorapatite; Py: pyrite, tr: trace

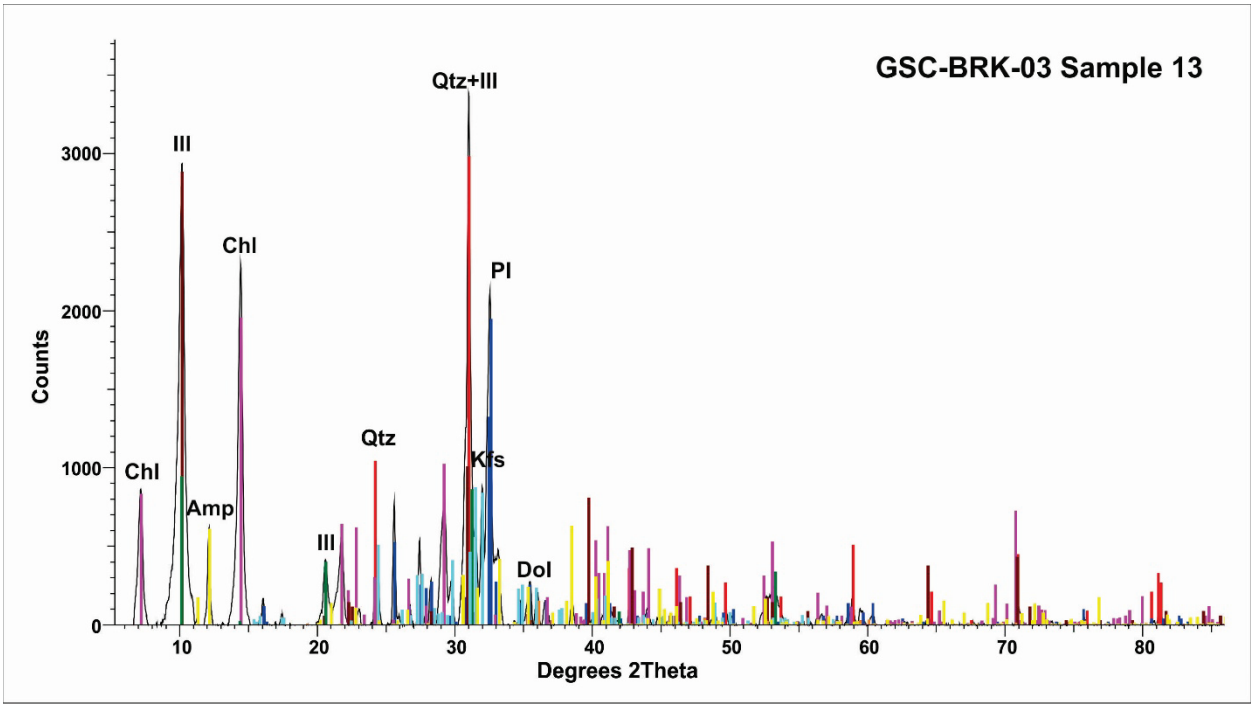

Figure 3. Diffractogram of the clay-size fraction of Sample 13 based on EVA (Bruker) software. Major X-ray peaks are labelled.

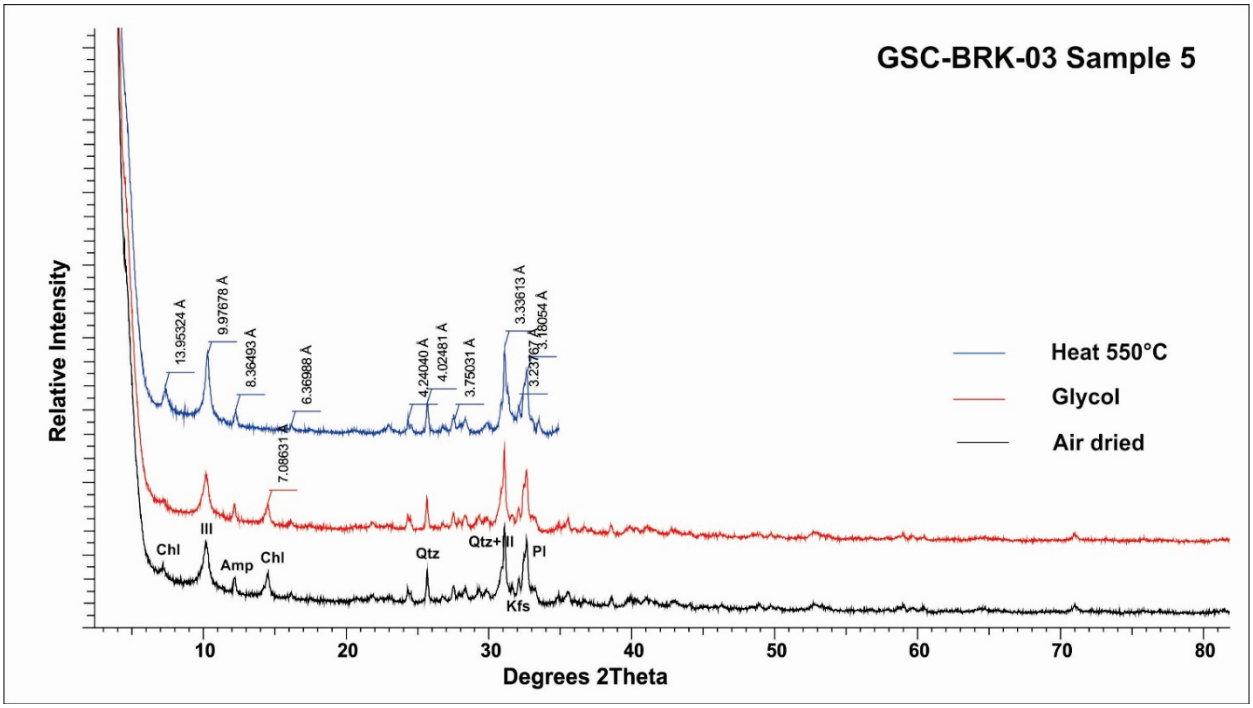

Figure 4. Stacked diffractograms of the air-dried, glycol saturated and heat-treated clay-size fraction of Sample 5 based on EVA (Bruker) software. Major X-ray peaks are labelled.

SEM

Three core samples were selected for thin section analysis from the top, middle, and bottom of the borehole based primarily on changes in density trends observed in the geophysical logs and core tests. The objectives of the SEM work were to examine downhole variations in:

- size and shape of silt- and clay-size grains,
- grain orientation (horizontally oriented versus randomly-oriented),
- grain distribution (laminated versus massive textures),
- mineralogy of the grains, and
- evidence of compaction (phyllosilicates deformed around denser minerals).

Representative images of these features from the three depth intervals are presented, with additional images provided in Appendix A. Several areas on each slide were chosen for examination under the SEM, creating a convention for image naming (e.g., Sample **5 -** Area **1 -** Image **A**). Certain areas were selected for follow-up with the FE-SEM to obtain higher resolution images of the clay-size grains. These images were denoted with the letters "FE". All images are presented in an upwards orientation. FE-SEM images from unoriented grain mounts from the three samples were also collected to examine the relief (shape) of the clay-size platelets and grains, which were masked by the presence of the petropoxy in the thin sections. Images are denoted as being captured in either backscattered electron (BSE) or secondary electron (SE) modes.

Sample 5 – depth range: 8.50 – 8.56 m

One thin section was produced from Sample 5, with three areas on the slide selected for analyses. Alternating coarse- to fine-grained, horizontal to sub-horizontal laminae are commonly visible in this interval (Figure 5). Coarse-grained laminae are of variable thickness (approximately 30 µm to 130 µm in Figure 5) with poorly-sorted angular to sub-angular clasts, ranging from clast- to matrix-supported (Figure 6). Fine-grained laminae are poorly-sorted and consist of mostly clay-size grains and dispersed clay- to medium silt-size silicate minerals. Silt-size grains are oriented mostly sub-horizontal to bedding, whereas most clay-size grains are unoriented. Silt-size platelets of biotite occur throughout the images and are oriented mostly sub-horizontal to bedding. These platelets appear "needle-like" in thin section as their edges are being viewed in cross section (Figure 7).

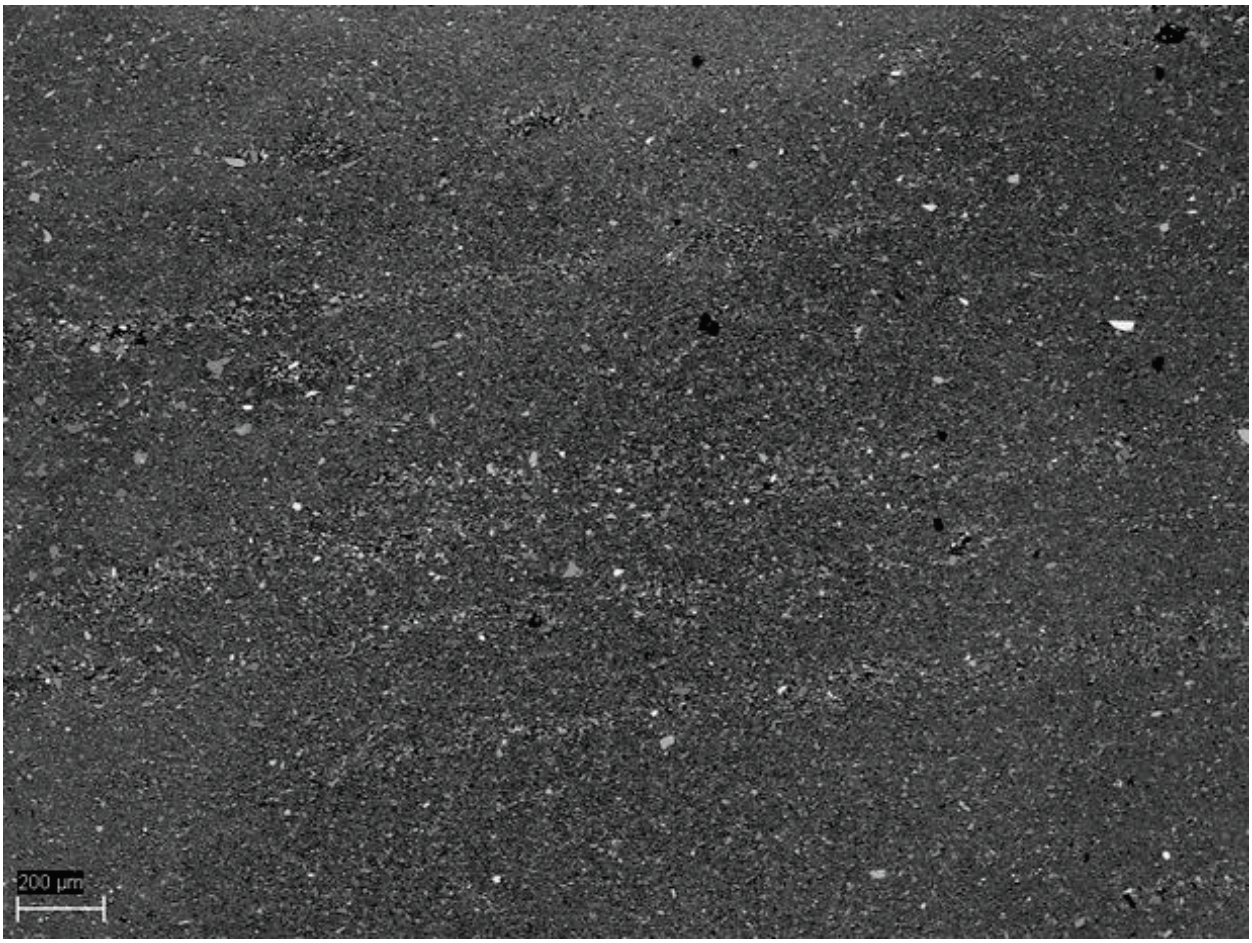

Figure 5. (Image 5-1-A, BSE) At this scale, sub-horizontal laminae are visible in the silt- and clay-size fraction (very few grains are very fine to fine sand). Coarse laminae are of variable thickness with poorly-sorted angular to sub-angular clasts which are matrix- to clast-supported.

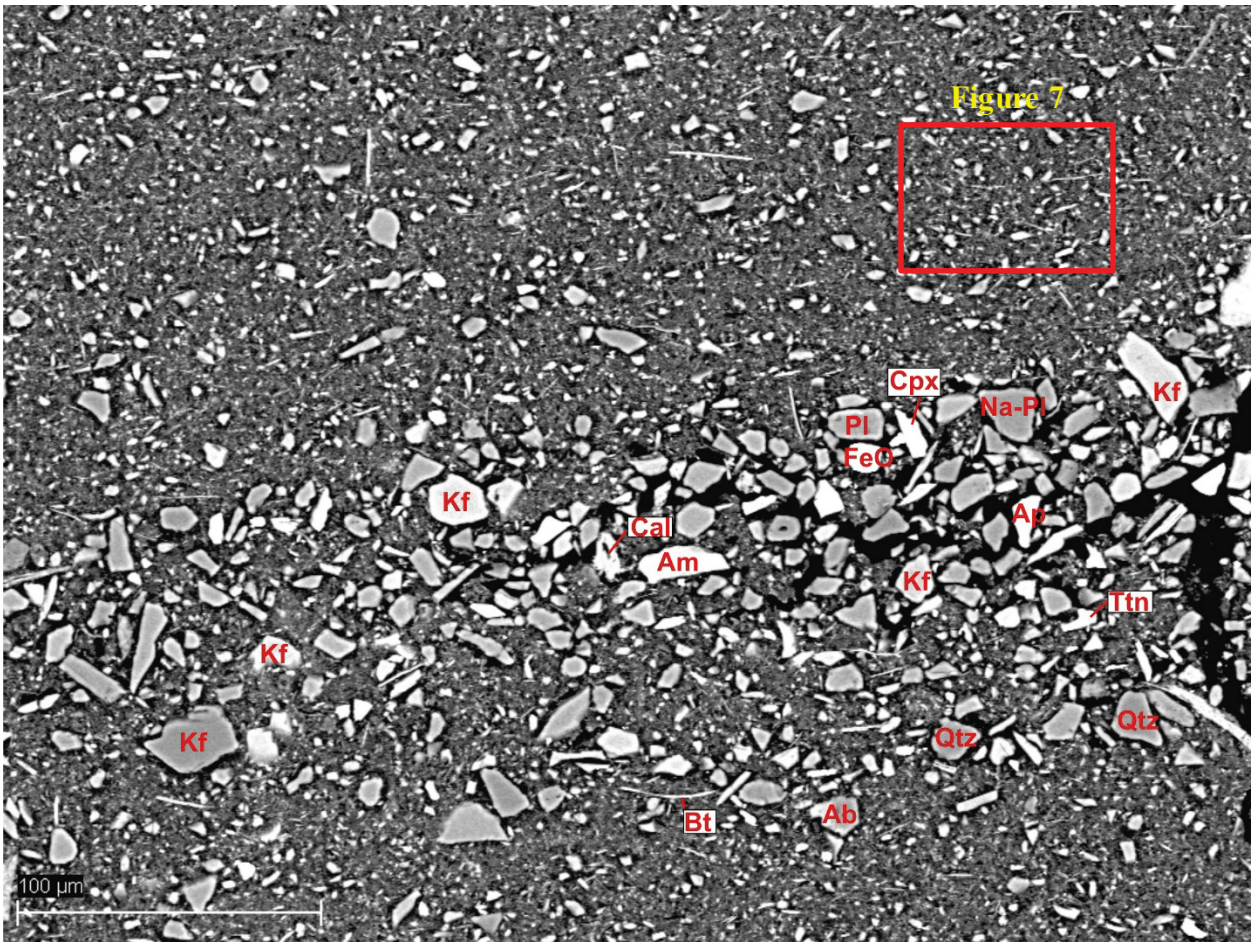

Figure 6. (Image 5-1-D, BSE) Detail of a silt lamina where grains are angular to sub-angular, and the layer ranges from matrix- to clast-supported. Within the fine-grained matrix directly above the silt lamina (see Figure 7), fine platelets of biotite grains appear randomly-oriented. (Ab=albite, Am=Amphibole, Ap=apatite, Bt=biotite, Cal=calcite, Cpx=clinopyroxene, Fe=iron oxide, (likely hematite), Kf=potassium feldspar, Na-Pl=sodic plagioclase, Pl=plagioclase, Qtz=Quartz, Ttn=titanite)

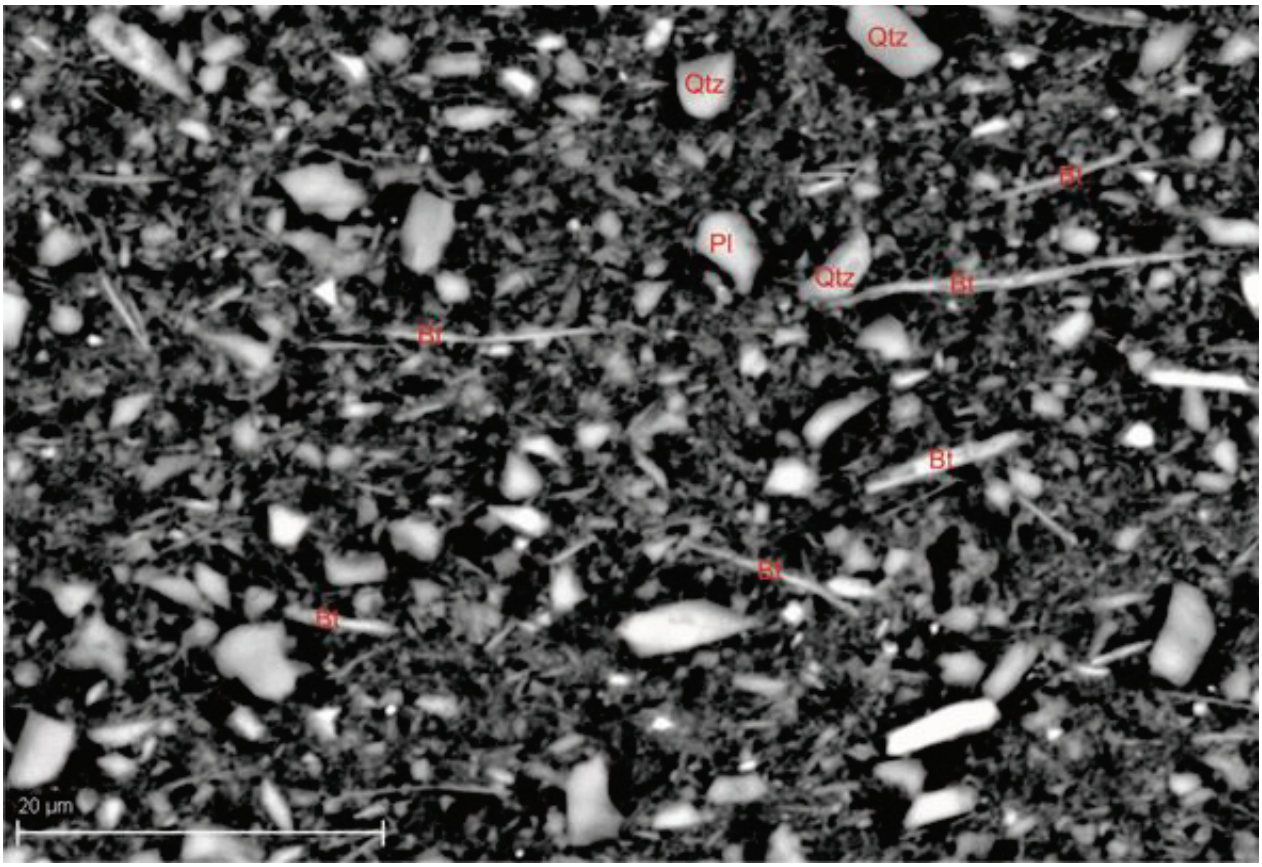

Figure 7. (Image 5-1-E, BSE) Area boxed in Figure 6 showing that the clay-size matrix is composed primarily of biotite and amphibole with fine to medium silt-size grains of biotite (Bt), quartz (Qtz), and plagioclase (Pl). Thin plates of biotite are primarily oriented sub-parallel to bedding.

Sample 13 – depth range: 32.72 – 32.77 m

One thin section was produced from Sample 13 with three areas on the slide selected for SEM analyses. Sample 13 is primarily massive in texture with coarse to fine silt-size grains which are angular to sub-angular and dispersed within a clay-size matrix (Figure 8; Appendix A: Figures A-17 to A-31). Only in a few locations on the thin section are lenses of silt observed (Appendix A: Figure A-24). An FE-SEM image from a grain mount shows how platelets from larger grains are 'flaking' to produce clay-size grains (Figure 9).

Biotite and amphibole grains generally appear more horizontally to sub-horizontally oriented than in the images of Sample 5, where grains of biotite are more randomly-oriented (sub-horizontal to vertical). Evidence for post-depositional compaction is observed where biotite grains are aligned around coarser grains. There is a rare occurrence of a biotite grain that is curved around the outer margin of a plagioclase grain (Figure 10).

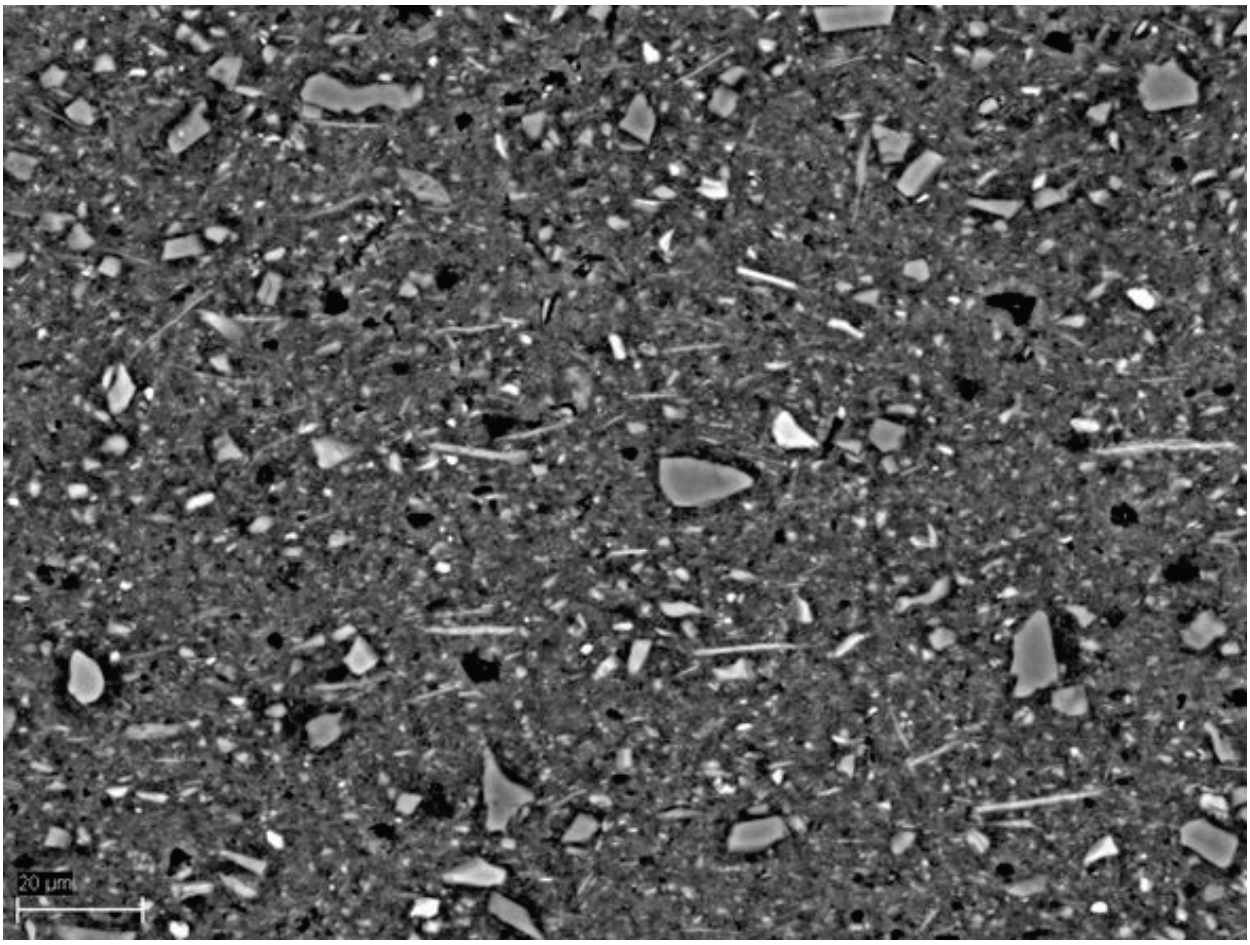

Figure 8. (Image 13-3-F, BSE) Image showing mostly horizontally to sub-horizontally aligned thin plates of biotite. The black features are pits and are an artifact of thin section polishing.

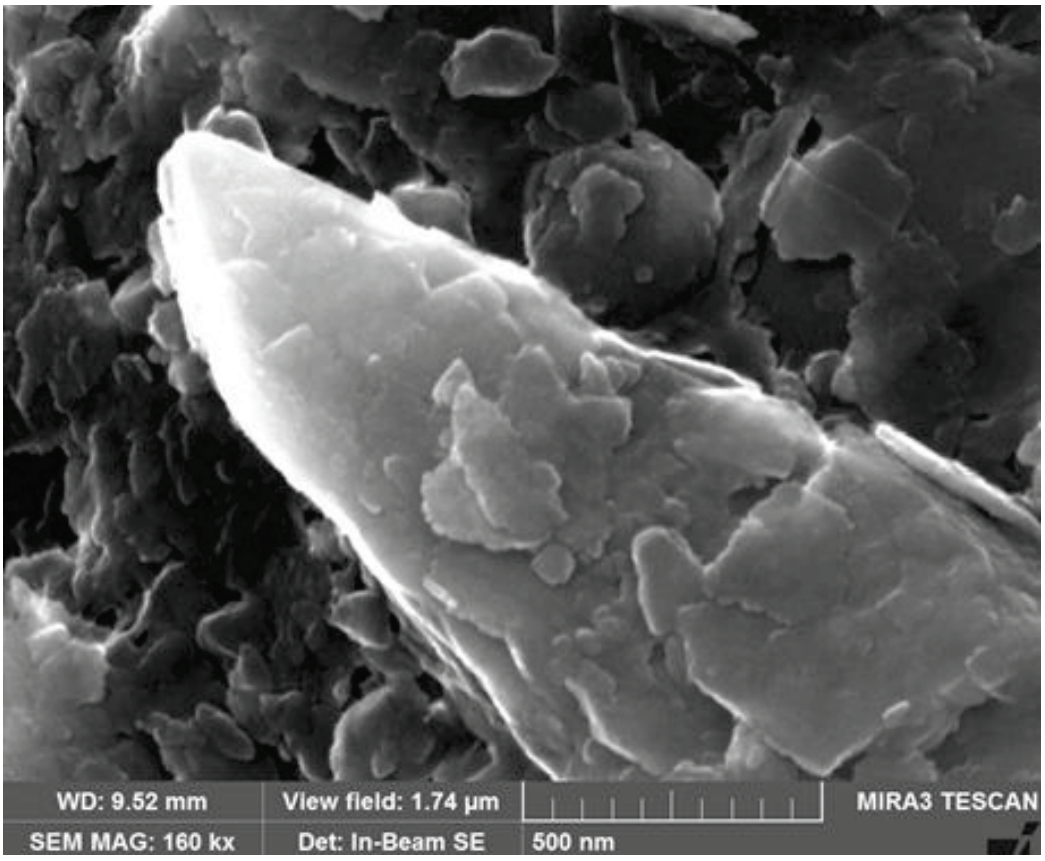

Figure 9. (Grain Mount Image 13-5, SE) FE-SEM image showing a fine silt-size grain consisting of numerous clay-size plates. These plates appear to be susceptible to "flaking off", resulting in clay-size particles with thicknesses of approximately 10 nm.

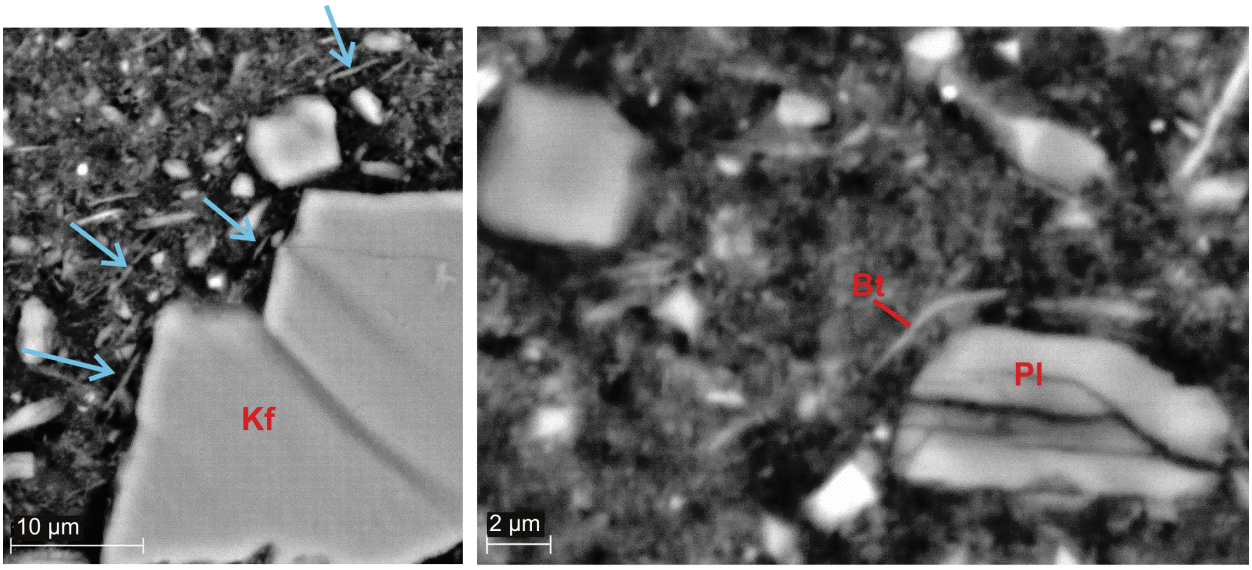

A B

Figure 10. Biotite (Bt) grains shown (A) aligning (blue arrows), or (B) curving around the margins of larger grains of potassium feldspar (Kf) and plagioclase (Pl). (Images 13-2-D and 13-2-C, BSE).

Sample 21 – depth range: 59.55 – 59.59 m

Four slides were created from Sample 21: Slides 21-A1, -A2, -B1, and -B2, with four areas selected for analyses among the four slides. There are two primary textures observed in Sample 21: massive and laminated (Figure 11). Both types contain angular to sub-angular, coarse to fine silt-size grains with dispersed fine sand grains. Irregular upper contacts observed in some laminae may provide evidence for bioturbation. The massive texture (Figure 12; Appendix A: Figures A-39 to A-41) exhibits randomly-oriented grains within a silty-clay matrix. The laminated unit consists of medium silt- to fine sand-size grains which are angular to sub-angular, randomly-distributed, and clast- to matrix-supported (Appendix A: Figures A-33, A-35, A-36). The fine-grained matrix in both textures contains biotite grains that are oriented sub-parallel to bedding, appearing similar to the images observed in Sample 5.

Also present are light and dark intervals of sub-horizontal laminae or lenses (Appendix A: Figure A-32). Typically, the darker bands contain fewer clasts and the matrix is richer in potassium (biotite). Lighter bands contain more clasts and the matrix tends to be more calcium-rich (amphibole).

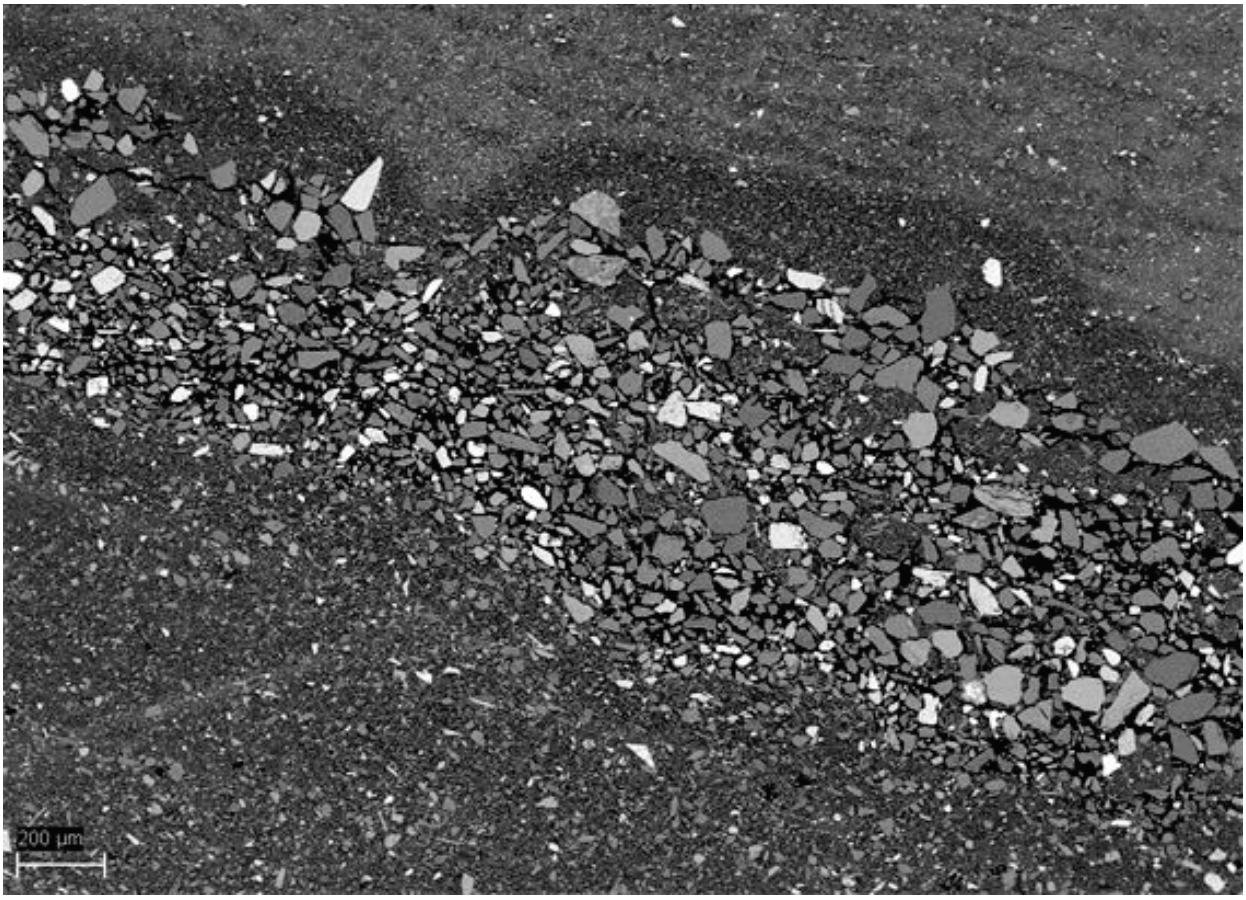

Figure 11. (Image 21-B1-2-A, BSE) Coarse layer within a finer-grained matrix. The irregular upper contact may be due to bioturbation.

Clasts are composed of a broad range of mineral types. Iron oxides are distinct under the SEM (Figure 13) and are present as ilmenite (titanium iron-oxide) and other iron oxide minerals not differentiated (i.e., magnetite, hematite, etc). Sub-micron-size, euhedral iron sulfide crystals were observed within chlorite grains (Figure 14; Appendix A: Figures A-44, A-45). Shells are noted (Appendix A, Figure TT). Amphibole and pyroxene are abundant and occur as silt- to clay-size grains. More rarely, epidote and allanite (containing rare earth elements) are observed.

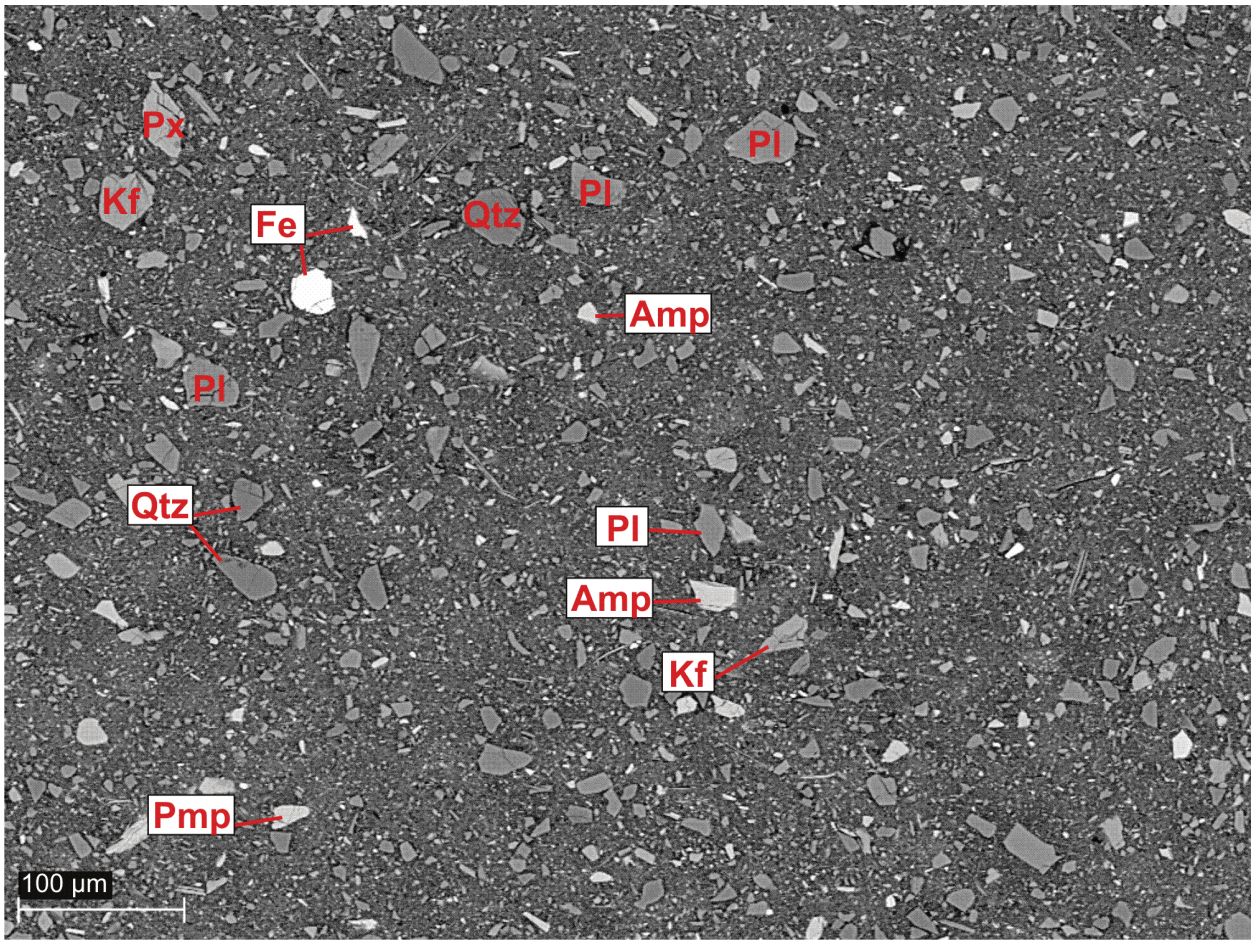

Figure 12. (Image 21-B1-1-B, BSE) Area displaying massive texture showing random orientation of angular to sub-angular silt-size clasts (Am=amphibole, Pmp=possibly pumpellyite, an epidote-group mineral, Fe=iron oxide, Kf=potassium feldspar, Pl=plagioclase, Px=pyroxene, Qtz=quartz).

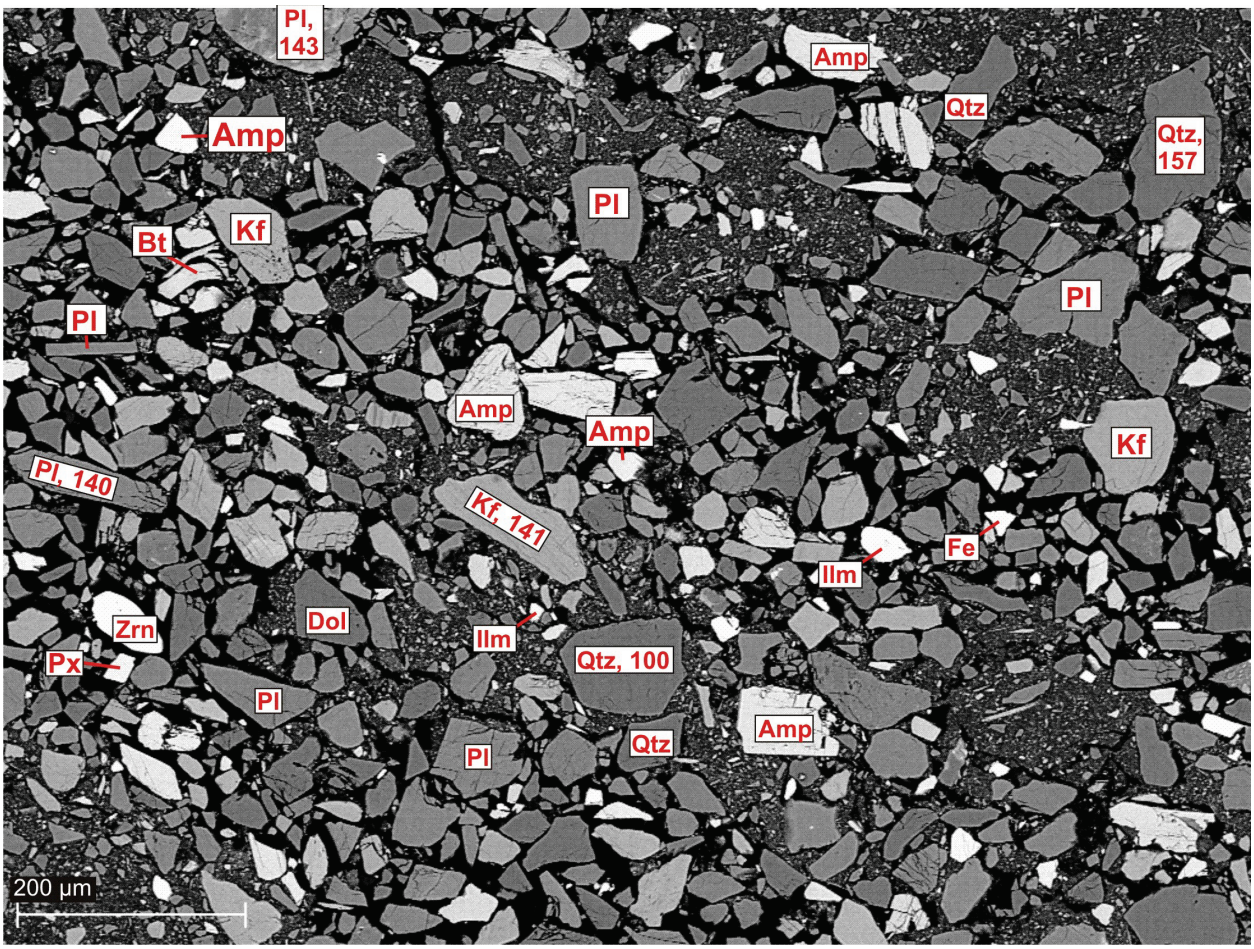

Figure 13. (Image 21-B1-2-B, BSE) Magnified view of upper part of the silt lamina in Figure 11. Grains are angular to sub-angular and occur up to fine sand-size. Numbers on selected grains represent grain lengths in µm (Amp=amphibole, Dol=dolomite, Fe=iron oxide, Ilm=ilmenite, Kf=potassium feldspar, Pl=plagioclase, Px=pyroxene, Qtz=quartz, Zrn=zircon).

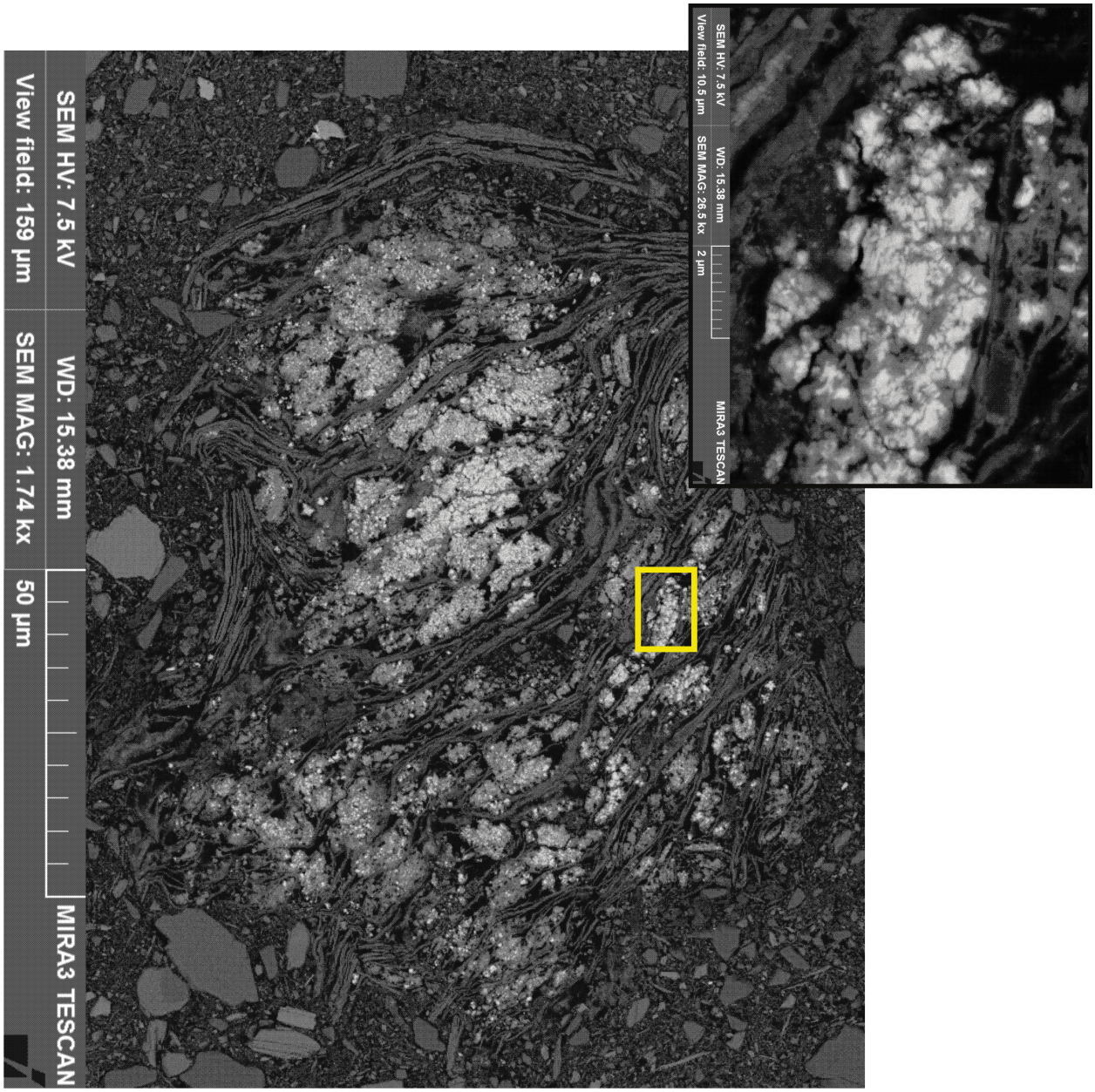

Figure 14. (Image 21-B1-FE-1, BSE) Iron sulfide crystals within chlorite grains. Inset (Image 21-B1-FE-3, BSE) shows detail of area boxed in yellow. Images are rotated to show the upward direction.

Magnetic Properties

Lab and downhole magnetic susceptibility measurements indicate variability in bulk susceptibility of the sediments (i.e., magnetic mineral content), but the amount of magnetite in all samples tested was predictably below the XRD's level of detection (~3%). For context, 3% magnetite would produce a magnetic susceptibility of approximately 10^{-1} SI (Enkin et al., 2020), which is an order of magnitude higher than the highest observed susceptibility in this borehole. Backscatter SEM analyses identified iron oxides and sulfides, but could neither differentiate the mineral form (e.g., hematite - Fe_2O_3, versus magnetite - Fe_3O_4), nor identify the presence of ferromagnetic grains at the nanoparticle scale. The analyses of the magnetic properties using coercivity and thermal susceptibility methods filled these gaps, providing missing information about the mineralogy, grain size, and concentration of the magnetic grains in the sediment samples. Results reveal an interesting variability in these parameters from sample to sample.

Magnetic Susceptibility

Magnetic susceptibility (MS) measurements were acquired on seven core samples using three lab instruments to compare responses to one another, and to the downhole log. In principle, the benchtop SI2B should produce more accurate measurements due to the insertion of the sample inside the sensing coils, and to its higher operating frequency which provides higher sensitivity.

The borehole log was collected using an EM39S downhole induction magnetic susceptibility instrument, manufactured by Geonics Limited. The instrument operates at a frequency of 39.2 kHz, and the configuration of the coils provide a radial sensitivity from approximately 5 to 25 cm outside the axis of the borehole and a vertical resolution of approximately 65 cm (McNeill et al., 1996). Due to the elevated bulk conductivity from relic seawater concentrations at this site, the magnetic susceptibility log was corrected using conductivity curves provided in McNeill (1986) and discussed in McNeill et al. (1996). For logging in unconsolidated sediments of low susceptibilities, the instrument is designed with a high degree of temperature compensation for downhole conditions. Prior to logging, calibrations were carefully carried out after the instrument had thermally equilibrated downhole for over 30 minutes and were rechecked at the end of the logging for drift.

In comparing the datasets in Table 5, the best agreement is observed between the downhole tool and the SI2B bulk susceptibility readings. The JH-8 and SM-20 instruments have relatively large coils and assume that the measured volume is a uniform half space. Placing small bags of sediment under the instruments' relatively large sensing region tends to underestimate the magnetic susceptibility by a factor of two when compared to the SI2B bulk values. The SI2B bulk susceptibility and the downhole susceptibility are generally very close, with variations accounted for by a difference in vertical scale. The small core samples selected (approx. 3 vertical cm) were unsieved silt and clay, whereas a much larger volume is sensed by the downhole tool. This is particularly important if the sensing volume contains increased sand content, as is the case with Samples 17 and 23. Differences in response between Samples 5 and 19 are primarily interpreted to be due to borehole completion conditions. In the upper 22 m, an increased width of the grout around the PVC casing appears to be influencing the magnetic susceptibility response with an increasing rise toward surface. Sample 19 is located just above an interval where all the logs record a small dip in readings, suggesting an enlargement exists in the borehole wall behind the

casing. Overall, the lab tests using the SI2B provide confidence in the response from the downhole susceptibility tool when the instrument is carefully calibrated prior to logging.

Table 5. Comparison of magnetic susceptibility measurements; refer to Table 1 for sample depths. JH-8 measurements were recorded six times over various parts of the palm-sized sample and averaged (uncertainty = 1 standard deviation). SI2B sample measurements were converted to grain susceptibilities using an average grain density of 2.76 g/cm^3, and to bulk susceptibility using nearest core-measured porosities.

Core Seg.	JH-8 Wet Mag. Susc. (x10^{-4} SI)	JH-8 Freeze-dried Mag. Susc. (x10^{-4} SI)	SM-20 Freeze-dried Mag. Susc. (x10^{-4} SI)	SI2B Grain Mag. Susc. (x10^{-4} SI)	Porosity (%)	SI2B Bulk Mag. Susc. (x10^{-4} SI)	Downhole Bulk Mag. Susc. (x10^{-4} SI)
5	4.8 ± 1.0	4.1 ± 0.7	4.7	25.3	72.9	6.9	29.8
13	3.8 ± 0.6	3.5 ± 0.4	4.5	22.5	64.6	8.0	10.5
17	11.5 ± 3.1	9.3 ± 2.0	12.4	51.3	54.6	23.3	35.3
19	9.5 ± 0.8	8.0 ± 2.1	10.7	44.4	55.5	19.8	9.2
20	6.3 ± 0.8	6.0 ± 0.9	7.8	38.7	57.4	16.5	24.2
21	14.7 ± 2.3	10.7 ± 2.3	15.1	60.7	54.0	27.9	24.7
23	16.3 ± 3.1	13.8 ± 3.0	14.6	68.6	52.1	32.9	46.4

Coercivity analyses

The magnetic hysteresis cycles and isothermal remanence magnetization curves from the J-Meter coercivity spectrometer (Figure 15) were analysed to provide the standard hysteresis parameters of saturation magnetization (M_S), remanence of saturation (M_{RS}), coercive force (H_C), and the remanent coercive force (H_{CR}). A graph of the magnetization ratio (M_{RS}/M_S) against the coercivity ratio (H_{CR}/H_C) is known as the Day plot (Day et al., 1977; Dunlop, 2002) and provides information about the grain sizes in a sample (Enkin et al., 2012). The Day plot for the seven samples tested displays points falling on a mixing line, suggesting the magnetic grain populations are a mixture of more stable (e.g., detrital) grains (possibly iron oxide magnetite) and less stable grains (possibly iron monosulfide greigite) (Figure 16).

Below 56 m, unusually rapid decays of NMR signal were observed, resulting in a significant underestimation of NMR porosities compared to the core porosities (Figure 2). The magnetic hysteresis parameters which appear to correlate best with this change in NMR behaviour are the M_{RS} and the M_{SP}. M_{RS} is a proxy measure of the volume concentration of fine stable magnetic grains and the M_{SP} is a proxy measure of the volume concentration of superfine, nanoparticle-scale, unstable magnetic grains (Figure 17). In both cases, the measurements suggest that there are more fine magnetic grains in the core below 56 m (thus increasing grain surface area), and these grains can produce strong magnetic gradients in the clay-bound water sites. These gradients appear to interfere with the NMR relaxation times from which the NMR porosities are calculated. See Crow et al. (2020) for more detail.

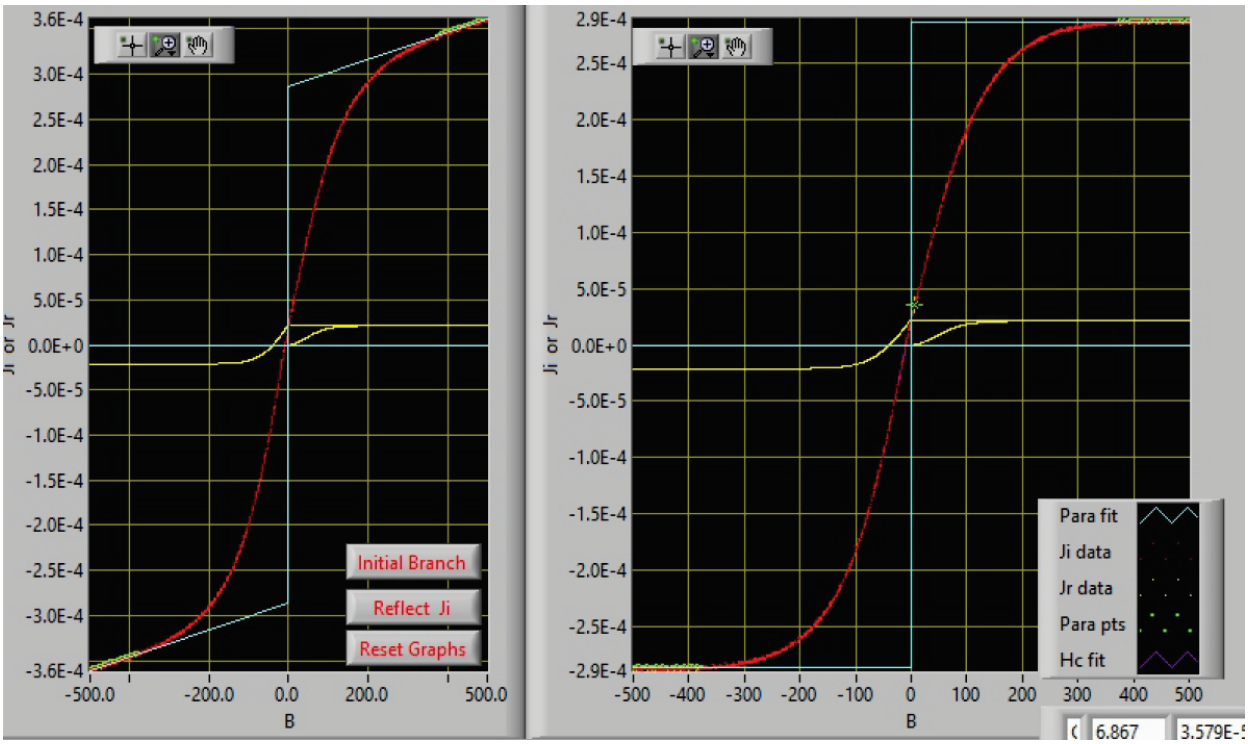

Figure 15. Sample analysis of J-Meter Coercivity Spectrometer data from Sample 17, showing the induced (red trace) and remanent (yellow trace) magnetization. The left panel shows the raw data, and the right panel shows the paramagnetic susceptibility (blue trace) removed, providing the ferromagnetic hysteresis curve. Enkin et al. (2007, 2012) provide more details of the analysis methods and applications.

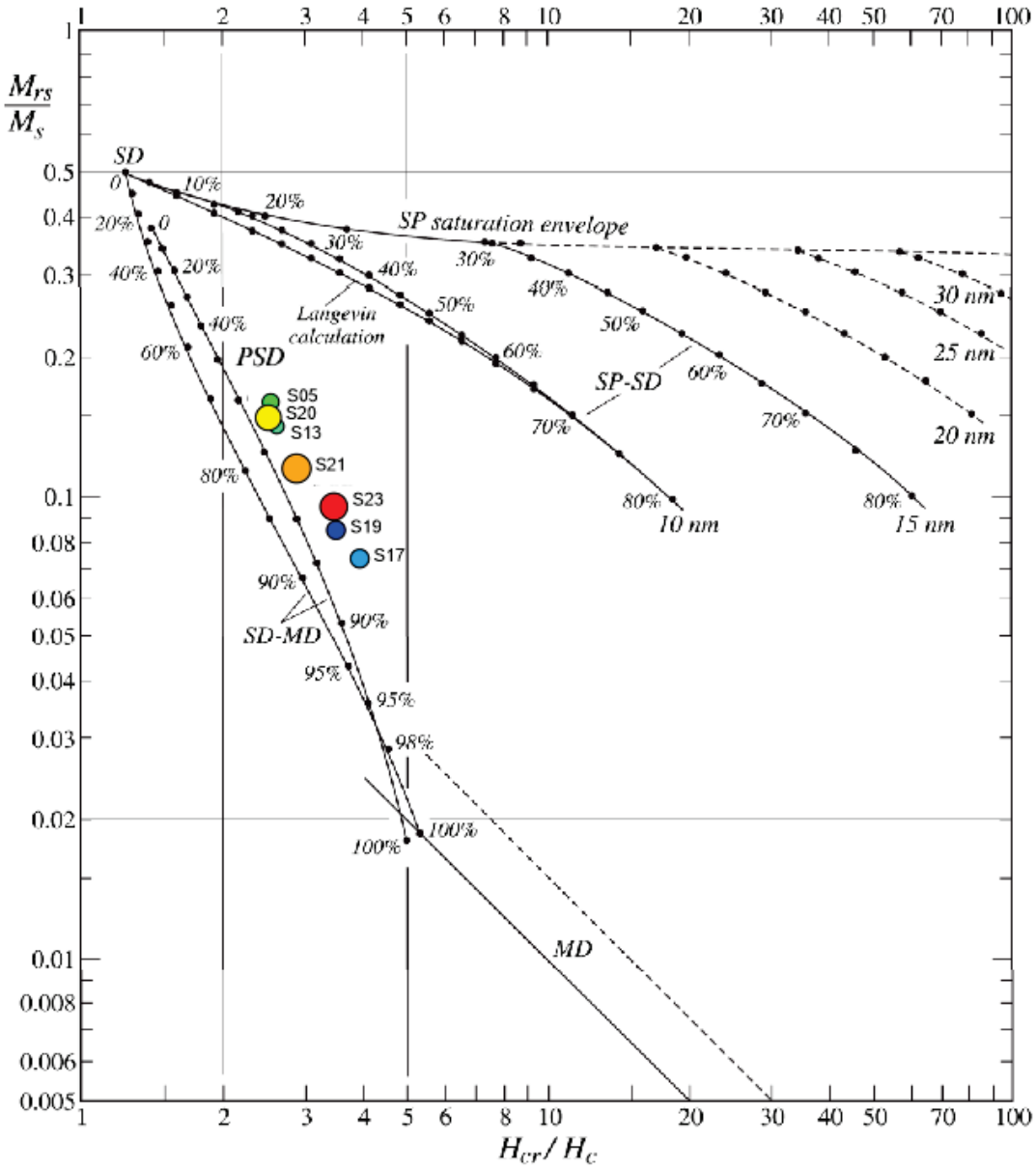

Figure 16. The Day plot (on a base plot developed by Dunlop, 2002) showing the position of all seven samples tested. Measurements are labelled with the sample number (Table 1) prefixed with "S". The size of each dot is proportional to the logarithm of the remanence of saturation magnetization (M_{RS}) and the colour reports the degree of superparamagnetic magnetization (M_{SP}), where the warm colours (yellow, orange, red) indicate the highest concentration of these unstably magnetized grains.

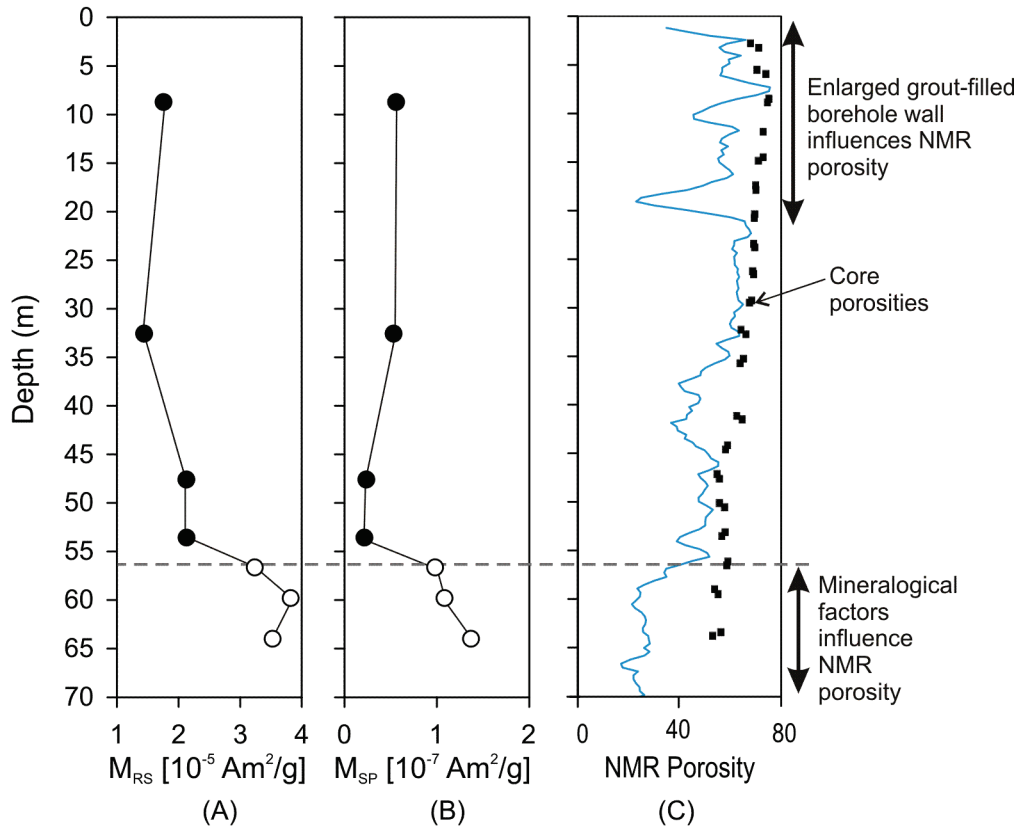

Figure 17. Magnetic properties from the coercivity analyses of seven core samples. The top four samples (filled symbols) are from depths where the NMR porosity measurements were acceptably accurate, whereas the bottom three samples (open symbols) were collected from depths which resulted in anomalously rapid NMR relaxation times resulting in low porosity estimates. (A) M_{RS}=remanent magnetization after saturation (0.5 T field). (B) M_{SP}=superparamagnetic magnetization, which is the remanent magnetization viscously lost while the applied field is reduced to zero over 1 minute. See text for physical interpretation. (C) Superparamagnetic nanoparticles are interpreted to cause rapid NMR signal relaxation, resulting in an apparent NMR porosity decrease in measurements taken below 56 m (dashed line).

Thermal susceptibility analyses

The thermomagnetic data indicate changes (decreases) in susceptibility over particular temperature ranges (Figure 18) related to the properties of certain magnetic minerals (e.g., magnetite with rapid decrease of susceptibility around 580°C, or sulfides around 350°C), and to mineralogical changes during heating (e.g., oxidation of magnetite to hematite). These response trends are generally consistent for all samples, but the steepness of the drop changes from sample to sample, suggesting variations in mineral concentrations. Results indicate a fundamental change occurs across the boundary between Samples 19 and 20. The deeper samples demonstrate the presence of sulfides particularly visible in the dashed cooling curves of samples 20 (green), 21 (red), and 23 (black). Samples 21 and 23 have by far the highest susceptibility.

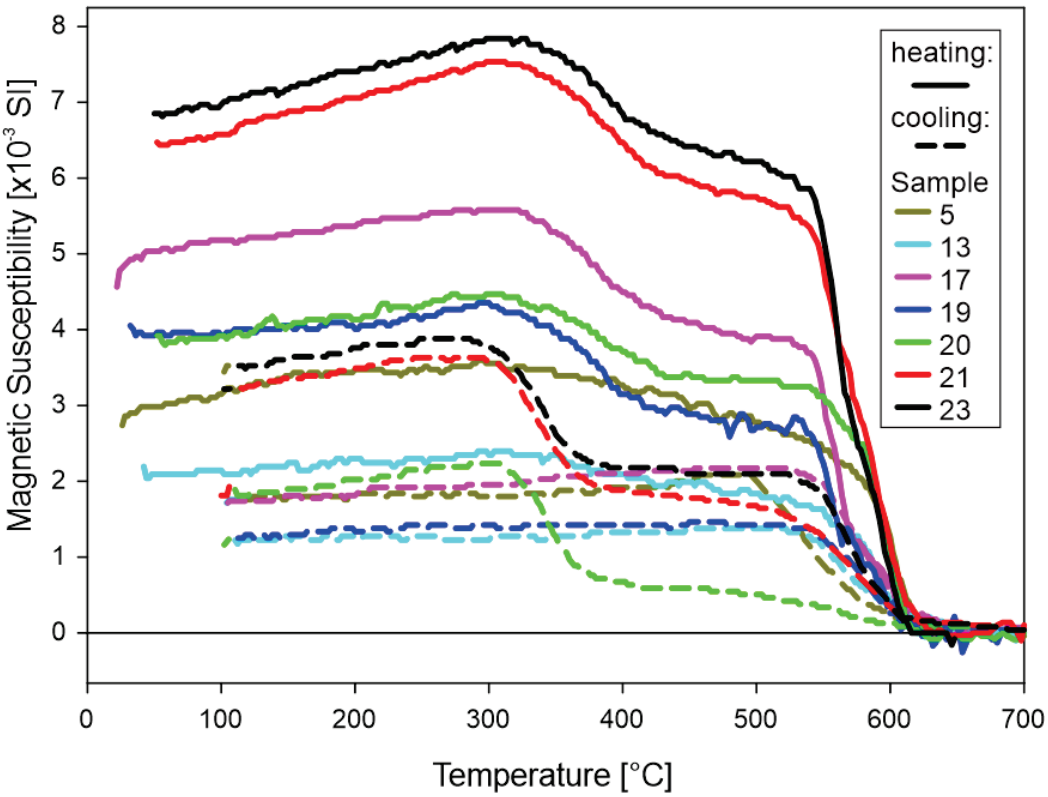

Figure 18. Thermomagnetic susceptibility meter output for the seven samples. The common features include a slow rise to 350° followed by a rapid decrease interpreted to be due to magnetic transformations. The rapid decay around 580° is likely from magnetite. On cooling, the deepest three samples (20, 21, and 23) display an increase around 350°C interpreted to be due to the formation of pyrrhotite from reactions with excess sulfide.

More insights into the magnetic mineral transformations are provided by the stepwise heating measurements with the thermosusceptibility meter. Two samples were chosen: Sample 17 from above the anomalous zone, and Sample 20 from within it (Figure 19). They demonstrate that the susceptibility drop at 350°C is due to the transformation of a high susceptibility mineral, likely magnetite, to a less magnetic mineral, likely hematite. This mineral transformation continues to higher temperatures and is superposed on the Curie Temperature susceptibility loss around 580°. The most important observation is the growth of the sulfide mineral (likely pyrhhotite) in Sample 20, after the 600°C heating step and increasing from the 650°C to the 700°C heating step.

For both samples, weight was lost each heating step but at different rates depending on the temperature. The weight loss was rapid at 100° C and 200°C possibly due to interstitial water loss. It picked up again at 550° C, likely due to dehydration of clays.

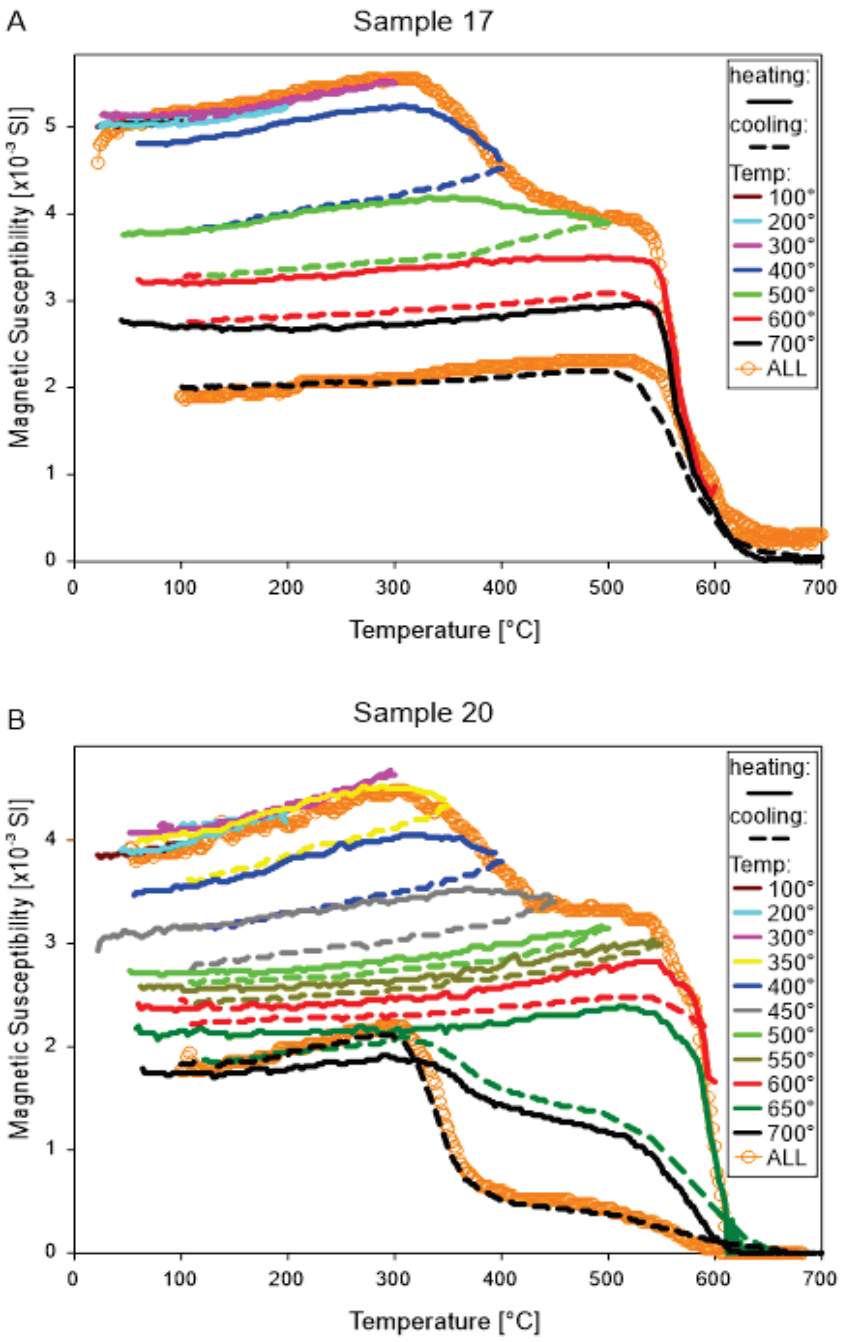

Figure 19. Stepwise thermomagnetic susceptibility curves for two samples. Each sample was heated then cooled to incrementally higher temperatures to determine the temperatures at which irreversible changes occurred. The orange curves are identical to the corresponding curves in a full heating-cooling cycle illustrated in Figure 18. In both samples, the magnetic susceptibility decrease observed between 350°C and 450°C is shown to be an irreversible mineralogical transformation, likely the oxidation of magnetite to hematite. A) In Sample 17, from above the 56 m depth transition, the sample displays a largely reversible Curie temperature decrease at 580° due to magnetite. B) Sample 20, from below the 56 m depth transition, displays a slightly higher Curie Temperature (magnetite plus maghemite?), and the growth of pyrrhotite after heating to 650° as seen by the extra susceptibility below 400°C.

DISCUSSION

New imagery and mineralogical analyses of Champlain Sea mud cores have provided insight into the geophysical log responses recorded in these fine-grained deposits. More broadly, the results provide context for ongoing interpretation of depositional and post-depositional characteristics of the sediments.

Gamma-ray measurements detect variations in the natural radioactivity originating from changes in concentration of the major rock forming element potassium (K), but also from the trace elements uranium (U) and thorium (Th). In sedimentary settings, potassium is generally the principal source of natural gamma radiation, primarily originating from clay minerals (although exceptions do occur where uranium is present (e.g., organic-rich mudstones). Gamma logs are commonly used to distinguish clay-rich strata (e.g., shales) from coarser-grained strata (e.g., sandstones), but the distinction between clay minerals and clay-size grains is often overlooked. In Champlain Sea muds, the distinction is needed as the clay mineralogy contributing to the overall gamma response is shown here to be low, resulting in relatively low and unvarying gamma ray responses, despite variations in clay-size grains. XRD analyses of the mud and sand fractions in the top, middle, and bottom of the borehole indicate the mineralogy remains fairly consistent. Analyses of the clay-size fraction indicate the mineralogy is composed of muscovitic and biotitic illite and chlorite. By weight percent, these clay minerals form 20 – 45% of the clay fraction, but the clay-size fraction forms only 30 – 57 % of the total grain size by volume – therefore, there is a paucity of clay minerals in these muds. The other mineral contributing to the gamma response, potassium feldspar, is observed to range between 10 – 20% by weight in the muds, and 10 – 12% by weight in the clay-size fraction. Regionally, sites may differ, based on the source area of the sediment, but typically, the dominance of plagioclase and quartz in the sediments observed throughout the Champlain Sea basin will control the relatively low levels of gamma counts recorded during logging.

A trend of increasing density and shear wave velocity with depth was recorded in the borehole logs of GSC-BH-BRK-03. Grain density and mineralogy for the silt and clay grain sizes are shown to remain fairly consistent along the borehole, indicating that changes in bulk density largely reflect changes in water content of the sediment column as it was expelled by compaction under the weight of the overlying material. This is supported by observations from the thin section work in the middle of the borehole, where platey biotite grains are observed to be oriented around the margins of larger grains, providing some evidence for compaction after deposition. Biotite and amphibole grains appear more horizontally to sub-horizontally oriented in the middle of the borehole versus the top, where grains of biotite are more randomly-oriented (sub-horizontal to vertical). Increases in density near the base of the well is also linked to an increase in coarse silt laminae, and particularly, to sand content.

The magnetic susceptibility, density, and grain size analyses, along with core segment observations, reveal an upward transition from silt-dominated strata containing sand lenses into a more massive mud. In the bottom of the borehole, electron micrographs show both massive and laminated textures with randomly-oriented grains. The laminae consist of medium silt- to fine sand-size grains, which are angular to sub-angular, randomly-distributed, and clast- to matrix-supported. The presence of laminae suggests that grains were hydraulically-sorted and segregated during sediment transport. The fine-grained matrix in both textures contains thin plates of biotite

grains that are sub-parallel to bedding. In the middle of the borehole, electron micrographs reveal a finer-grained and more massive texture, but with platey biotite and amphibole grains appearing more horizontally to sub-horizontally oriented than in the sample below. The textural changes observed from the bottom to the middle of the borehole may record a transition from a proximal to a more distal depositional setting in the basin, and is the topic of ongoing research. In the shallowest sample, alternating coarse- to fine-grained, horizontal to sub-horizontal laminae were again observed. Silt-size platelets of biotite occur throughout the thin section and are oriented mostly sub-horizontal to vertical to bedding, appearing closer in orientation to those observed in the deepest sample.

Downhole magnetic susceptibility logs have been used for many decades by the GSC for lithological interpretation in unconsolidated sediments of low susceptibilities (McNeill et al, 1996; Crow et al., 2018). In glacial sediments containing source material from the Canadian Shield, variation in grain size is particularly well captured by the susceptibility log where coarser-grained materials (sands) have retained a higher percentage of heavier, detrital magnetic minerals than in the fine-grained fraction (silts and clays). This is observed in GSC-BH-BRK-03 where increases in sand content are reflected by increases in the magnetic susceptibility log. The sediment magnetism analyses conducted as part of this study contribute new information about the nature of the magnetic minerals in the silt and clay fraction.

Analyses of bulk magnetic susceptibility using the SI2B meter in seven unsieved samples of mud along the borehole reveal a range of bulk susceptibilities between 7 and 34 $\times 10^{-4}$ SI, increasing downward with increasing silt content. The downhole log responses are in very close agreement with these values, providing greater confidence in the instrument performance in this operating range. Iron oxide minerals are observed in clay- to silt-size grains in all samples examined under the SEM. Tests with the thermomagnetic susceptibility meter identified the presence of magnetite in all seven samples. A plot of grain density versus magnetic susceptibility (Enkin et al., 2020) suggests that the range of magnetic susceptibilities in the borehole corresponds to a volume of magnetite in the massive muds that is approximately 100 ppm (0.01%). This increases to approximately 0.3% in the deepest part of the borehole (71.5 m), where susceptibilities measured by the downhole tool reach 10^{-2} SI as sand content increases. The sensitivity of the downhole instrument to variations in magnetite concentration could more broadly be applied to investigate the idea of magnetite nanoparticles as a cementing agent (Torrance et al, 2017). Downhole instrument calibration would be a key aspect of this work, as the response measured in the massive muds (e.g. 10^{-4} SI) would be in the lower end of the sensitivity range for most tools, requiring an instrument with adequate temperature compensation.

While the magnetic susceptibility log varies with the volume of magnetic minerals (primarily magnetite), the NMR log also responds to the surface area of the magnetic minerals and the magnitude of internal magnetic gradients, both of which increase as pore size decreases (Fay et al., 2015). Studies by Keating and Knight (2007a, b) and Keating et al. (2020) show that magnetite nanoparticles can dramatically shorten relaxation times, even in very small concentrations. Anomalously short NMR relaxation times were observed below 56 m, but at levels of magnetic susceptibility that were encountered at shallower depths without the short relaxation. Analyses of the coercivity measurements reveal a change in the mineralogy and concentration of the magnetite grains occurs between core samples tested at 53.94 m (Sample 19) and 56.97 m (Sample 20).

Below this transition, the magnetic remanence of saturation (M_{RS}) is higher, indicating more magnetic minerals, and the superparamagnetic magnetization (M_{SP}) is higher, indicating that a high proportion of the magnetic grains are highly magnetic nanoparticles. This change in magnetic granulometry explains why the magnetic susceptibility log is equally elevated above and below 56 m (30 x 10^{-4} SI), but the NMR relaxation times decreases abruptly below 56 m.

This change in grain size is interpreted to relate to a transition across the sulfate-methane transition zone, where methane from below the boundary is oxidized by oceanic sulfate from above the boundary. Iron sulfides in framboidal form are commonly seen as a result of the sulfide ions combining with iron. Further mineralogical studies may be able to confirm the presence of greigite or other iron sulfide mineral growths in these features. The integration of pore water chemistry into these analyses is a topic of ongoing research at the GSC.

SUMMARY

New lab analyses of core samples from a GSC borehole in Breckenridge Creek Valley, Pontiac, Quebec provided insights into downhole geophysical log responses in Champlain Sea muds. Key observations include:

- Mineralogical analyses on the clay-size fraction confirm that the lack of potassium-rich minerals (i.e., clay minerals and potassium feldspar) result in the relatively low and unvarying gamma log responses observed;
- SEM images from the top, middle, and bottom of the borehole identified diverse grain orientations, sizes, and textures in each interval, and provided some evidence for compaction where biotite grains were observed to align or curve around the outer margins of larger grains in the middle sample;
- A consistent grain density in the muds, coupled with a reduction in water content with depth, primarily accounts for a trend of increasing bulk density and shear wave velocity logs with depth;
- Mineral identification using energy-dispersive X-ray spectroscopy under the SEM indicated that iron oxides were present in clay- to silt-size grains;
- Magnetism studies indicated the iron oxide, magnetite, is present in varying concentrations and grain sizes in all samples, ranging from silt- and clay-size detrital grains down to nanoparticles;
- These highly magnetic nanoparticles coincided with an observed shortening of downhole NMR relaxation times near the base of the borehole. They are interpreted to have created elevated internal magnetic gradients during the logging that interfered with NMR porosity estimations;
- The change in grain size is interpreted to relate to crossing the sulfate-methane transition zone and is the subject of ongoing study.

These results provide context for geophysical log interpretation in fine-grained post-glacial sediments at other locations throughout the Ottawa and St Lawrence valleys. The results also raised fundamental questions about depositional (sedimentological) and post-depositional (geochemical) processes in these sediments. Ongoing GSC research, integrating pore water chemistry and the role of hydrogeological conditions, is underway at this and other cored borehole sites in the Ottawa area to improve our understanding of the conditions that influence sediment stability and landslide susceptibility.

ACKNOWLEDGMENTS

The authors gratefully acknowledge the contributions of Igor Bilot, Tark Hamilton, Pat Hunt, Ian Jonasson, Shauna Madore, Meghan Mohar, Matthew Polivchuk, Miriam Wygergangs, and Kyle Yun during the laboratory analyses of the samples, and we sincerely thank Sam Alpay for her review of this report. Funding for this project was provided through the GSC's Public Safety Geoscience Program under the Intraplate Earthquake Project.

REFERENCES

Anderson, T.W., 1988. Late Quaternary pollen stratigraphy of the Ottawa Valley–Lake Ontario region and its application in dating the Champlain Sea, in Gadd N.R. (ed.) The Late Quaternary Development of the Champlain Sea basin, Geological Association of Canada, Special Paper 35, p. 207-224.

ASTM (American Society for Testing and Materials), 2014. ASTM D5550-06. Standard test method for specific gravity of soils by gas pycnometer, ASTM International, West Conshohocken, PA.

Armstrong, D.K., and Dodge, J.E.P., 2007. Paleozoic geology of southern Ontario; Ontario Geological Survey, Miscellaneous Release - Data 219.

Brooks, G.R., 2013. A massive sensitive clay landslide, Quyon Valley, southwestern Quebec, Canada, and evidence for a paleoearthquake triggering mechanism; Quaternary Research (New York) v. 80, n. 3, p. 425-434. https://doi.org/10.1016/j.yqres.2013.07.008

Brooks, G.R., Medioli, B.E., Aylsworth, J.M., and Lawrence, D.E., 2013. A compilation of radiocarbon dates relating to the age of sensitive clay landslides in the Ottawa Valley, Ontario-Québec; Geological Survey of Canada, Open File 7432, 62 p. https://doi.org/10.4095/292913

CFEM, 2006. Canadian Foundation Engineering Manual, 4th Edition, Canadian Geotechnical Society, BiTech Publishers, 488 p.

Coates, G.R., Xiao, L., and Prammer, M.G., 1999. NMR Logging: Principles & Applications. Halliburton Energy Services Publication H02308. 234 p.

Crow, H.L., Hunter, J.A., and Motazedian, D., 2011. Monofrequency Insitu damping measurements in Ottawa area soft soils; Journal of Soil Dynamics and Earthquake Engineering, v. 31, p. 1669-1677.

Crow, H.L., Alpay, S., Hinton, M.J., Knight, R.D., Oldenborger, G.A., Percival, J.B., Pugin, A.J.-M., and Pelchat, P., 2017. Geophysical, geotechnical, geochemical, and mineralogical data sets collected in Champlain Sea sediments in the Municipality of Pontiac, Québec; Geological Survey of Canada, Open File 7881, 51 p. https://doi.org/10.4095/301664

Crow, H.L., Hunter, J.A., Olson, L., Pugin, A.J.-M., and Russell, H.A.J., 2018. Borehole geophysical log signatures and stratigraphic assessment in a glacial basin, southern Ontario; Canadian Journal of Earth Sciences, v. 55(7), p. 829-845. https://doi.org/10.1139/cjes-2017-0016

Crow, H.L., Enkin, R.J., Percival, J.B., and Russell, H.A.J., 2020. Downhole nuclear magnetic resonance logging in glaciomarine sediments near Ottawa, Ontario, Canada; Journal of Near Surface Geophysics. https://doi.org/10.1002/nsg.12120

Cummings, D.I., Gorrell, G., Guilbault, J.-P., Hunter, J.A., Logan, C., Ponomarenko, D., Pugin, A.J.-M., Pullan, S.E., Russell, H.A.J., Sharpe, D.R., 2011. Sequence stratigraphy of a glaciated basin fill, with a focus on esker sedimentation; Geological Society of America Bulletin, v. 123, p. 1478-1496.

Day, R., Fuller, M., and Schmidt, V.A., 1977. Hysteresis properties of titanomagnetites: Grain size and composition dependence; Physics of the Earth and Planetary Interiors, v. 13, p. 260–267.

Duguay-Blanchette, J., 2016. Étude du comportement statique et cyclique de deux argiles sensibles de l'est du Canada. Master's thesis, Université Laval, Québec, Canada, 254 p.

Dunlop, D.J., 2002. Theory and application of the Day plot (Mrs/Ms versus Hcr/Hc) 1. Theoretical curves and tests using titanomagnetite data; Journal of Geophysical Research, v. 107, 2056, 22 p. https://doi:10.1029/2001JB000486

Dunn, K.J., Bergman, D.J., and Latorraca, G.A., 2002. Nuclear Magnetic Resonance Petrophysical and Logging Applications. Oxford, United Kingdom, Elsevier Science, 293 p.

Eden, W.J., and Mitchell, R.J., 1970. The mechanics of landslides in Leda clay. Canadian Geotechnical

Journal, v. 7, p. 285-296.

Enkin, R.J., Hamilton, T.S., and Morris, W.A., 2020. The Henkel petrophysical plot: Mineralogy and lithology from physical properties. Geochemistry, Geophysics, Geosystems, v. 20, e2019GC008818. https://doi.org/10.1029/2019GC008818

Enkin, R.J., Baker, J., Nourgaliev, D., Iassonov, P., and Hamilton, T.S., 2007. Magnetic hysteresis parameters and Dayplot analysis to characterize diagenetic alteration in gas hydrate bearing sediments; Journal of Geophysical Research, v. 112, B06S90. https://doi:10.1029/2006JB004638

Enkin, R.J., Cowan, D., Tigner J., Severide, A., Gilmour, D., Tkachyk, A., Kilduff, M., Vidal, B., and Baker, J., 2012. Physical property measurements at the GSC Paleomagnetism and Petrophysics Laboratory, including electric impedance spectrum methodology and analysis; Geological Survey of Canada, Open File 7227, 42 p. https://doi:10.4095/291564

Fay, E.L., Knight, R., and Song, Y.-Q., 2015. Investigating internal magnetic field gradients in aquifer sediments. Geophysics, v. 80, p. 281-294.

Gadd, N.R., 1986. Lithofacies of Leda clay in the Ottawa basin of the Champlain Sea. Geological Survey of Canada Paper 85-21, 44 p.

Girard, I., Klassen, R.A., and Laframboise, R.R., 2004. Sedimentology laboratory manual, Terrain Sciences Division; Geological Survey of Canada, Open File 4823, 134 p.

Hinton, M.J., and Alpay, S., 2020. Constraining groundwater flow in Champlain Sea muds; in Southern Ontario groundwater project 2014-2019: in Summary Report; Russell, H. A. J. and Kjarsgaard, B. A. (eds.); Geological Survey of Canada, Open File 8536, p. 203-215. https://doi.org/10.4095/321106

Hunter, J.A., Crow, H.L., Brooks, G.R., Pyne, M., Motazedian, D., Lamontagne, M., Pugin, A.J.-M., Pullan, S.E., Cartwright, T., Douma, M., Burns, R.A., Good, R.L., Kaheshi-Banab, K., Caron, R., Kolaj, M., Folahan, I., Dixon, L., Dion, K., Duxbury, A., Landriault, A., Ter-Emmanuil, V., Jones, A., Plastow, G., and Muir, D., 2010. Seismic site classification and site period mapping in the Ottawa area using geophysical methods; Geological Survey of Canada, Open File 6273, 1 DVD.

Keating, K., and Knight, R., 2007a. A laboratory study on the effect of magnetite on NMR relaxation rates; Journal of Applied Geophysics, v. 66, p. 188-196.

Keating, K., and Knight, R., 2007b. A laboratory study to determine the effects of iron oxides on proton NMR measurements; Geophysics, v. 72, p. E27-E32.

Keating, K., Walsh, D.O., and Grunewald, E., 2020. The effect of magnetic susceptibility and magnetic field strength on porosity estimates determined from low-field nuclear magnetic resonance; Journal of Applied Geophysics, v. 179. https://doi.org/10.1016/j.jappgeo.2020.104096

Khaheshi Banab, K., Kolaj, M., Motazedian, D., Sivathayalan, S., Hunter, J.A., Crow, H.L., Pugin, A.J.-M., and Brooks, G., 2012. Seismic site analysis for Ottawa, Canada: A comprehensive study using measurements and numerical simulations; Bulletin of the Seismological Society of America, Vol. 102, No. 5, p. 1976–1993. https://doi: 10.1785/0120110248

Kramer, S.L., 1996. Geotechnical Earthquake Engineering, Prentice Hall, 653 p.

L'Heureux, J.-S., Locat, A., Leroueuil, S., Demers, D., and Locat, J., 2013. Landslides in sensitive clays: From geosciences to risk management; Advances in Natural and Technological Hazards Research, v. 36, Springer Science+Business Media Dordrecht. https://doi 10.1007/978-94-007-7079-9

MacPherson, J.B., 1968. The physiographic evolution of the Montreal archipelago. The Canadian Geographer, v. 12, p. 254–265.

McNeill, J.D., 1986. Geonics EM39 borehole conductivity meter: Theory of operation, Technical Note TN-20, 18 p. http://www.geonics.com/pdfs/technicalnotes/tn20.pdf.

McNeill, J.D., Hunter, J.A., and Bosnar, M., 1996. Application of a borehole induction magnetic susceptibility logger to shallow lithological mapping. Journal of Environmental and Engineering Geophysics, v. 0, p. 77-90.

Medioli, B.E., Alpay, S., Crow, H.L., Cummings, D.I., Hinton, M.J., Knight, R.D., Logan, C., Pugin, A.J.-M., Russell, H.A.J., and Sharpe, D.R., 2012. Integrated data sets from a buried valley borehole, Champlain Sea basin, Kinburn, Ontario. Geological Survey of Canada, Current Research (Online) no. 2012-3, 2012, 20 p. https://doi.org/10.4095/289597

Mitchell, R.J., 1970. Landslides at Breckenridge, Pineview Golf Club, and Rockcliffe; Technical Paper No. 322, Division of Building Research, National Research Council of Canada, Ottawa, June 1970.

Percival, J.B., Aylsworth, J.M. and Fritz, A., 2003. Analysis of colour rhythmites in sensitive marine clays (Leda Clay) from eastern Canada; in Dominguez, E.A., Mas, G.R. and Cravero, F. (eds.), 2001: A Clay Odyssey. Proceedings of the 12th International Clay Conference, Bahia Blanca, Argentina, Elsevier, p. 147-154.

Rust, B.R., and Romanelli, R., 1975. Late Quaternary subaqueous outwash deposits near Ottawa, Canada; in Jopling A.V. and McDonald B.C. (eds) Glaciofluvial and Glaciolacustrine Sedimentation. Society for Sedimentary Geology Special Publication 23, p. 177–192.

Sangrey, D.A., 1972. Naturally cemented sensitive soils. Géotechnique, v. 22, No.1, p. 139-152.

Skempton, R.W., and Northey, A.D., 1952. The sensitivity of clays. Géotechnique, v 3, p. 30-53.

Torrance, J.K., 1979. Post-depositional changes in the pore water chemistry of the sensitive marine clays of the Ottawa area, eastern Canada. Engineering Geology, v. 14, p. 135-147.

Torrance, J. K., 2017. Chemistry: An essential key to understanding high-sensitivity and quick clays and to addressing landslide risk. in Thakur, V., L'Heureux, J.-S., and Locat, A. (eds.), Landslides in Sensitive Clays: From Geosciences to Risk Management, Advances in Natural and Technological Hazards Research, v. 46, p. 35 – 44, DOI 10.1007/978-3-319-56487-6_3

APPENDIX A

Scanning Electron Microscope Images

Samples 5, 13 and 21

Sample 5 – depth range: 8.50 – 8.56 m

Image 5-1-A

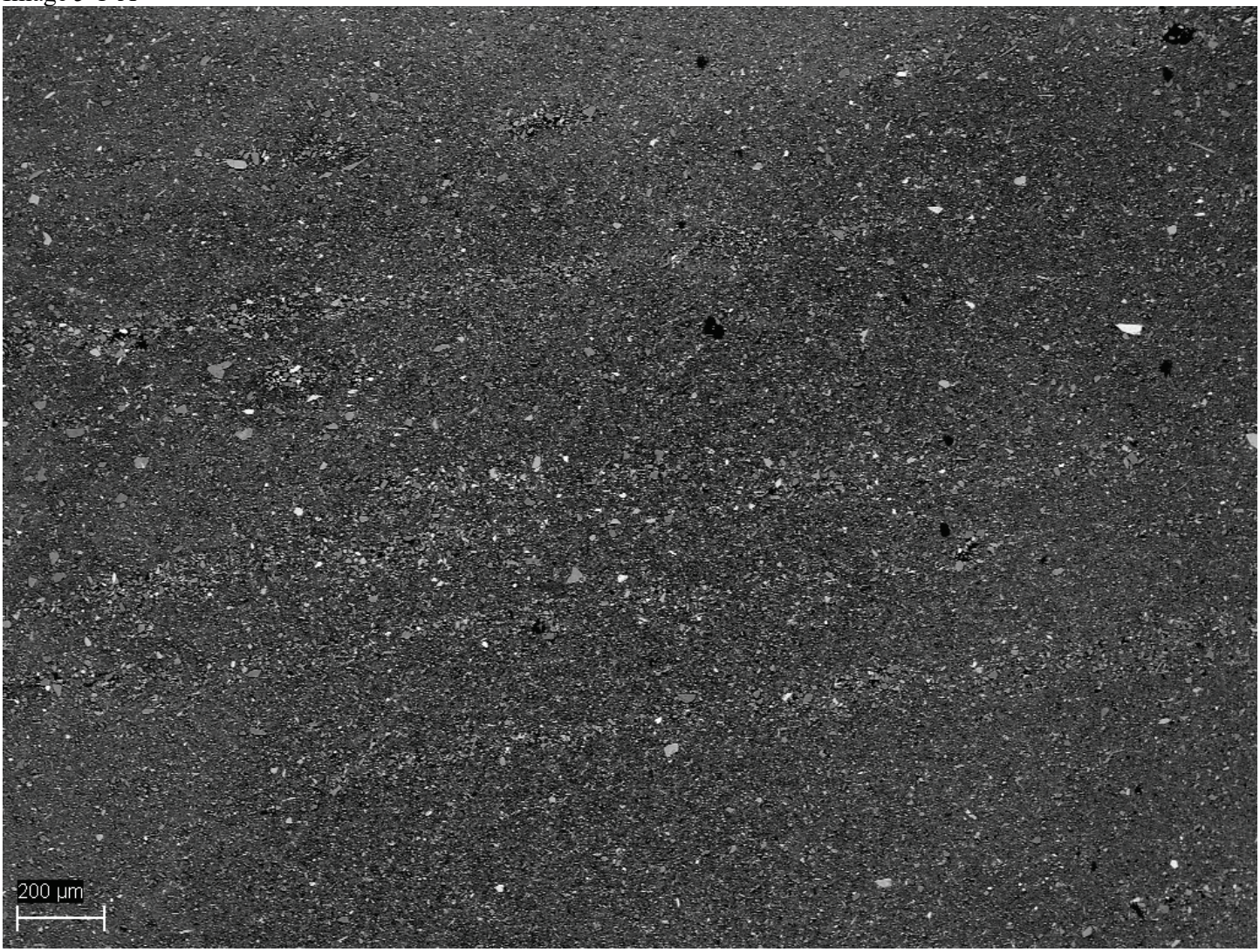

Figure A-1. Backscattered electron (BSE) micrograph showing sub-horizontal laminae in the silt- and clay-size fraction with few grains of very fine to fine sand-size. Coarse laminae are laterally discontinuous and are of variable thickness with poorly-sorted angular to sub-angular, matrix-supported clasts. The presence of laminae suggests that grains were hydraulically sorted and segregated during sediment transport.

Image 5-1-C

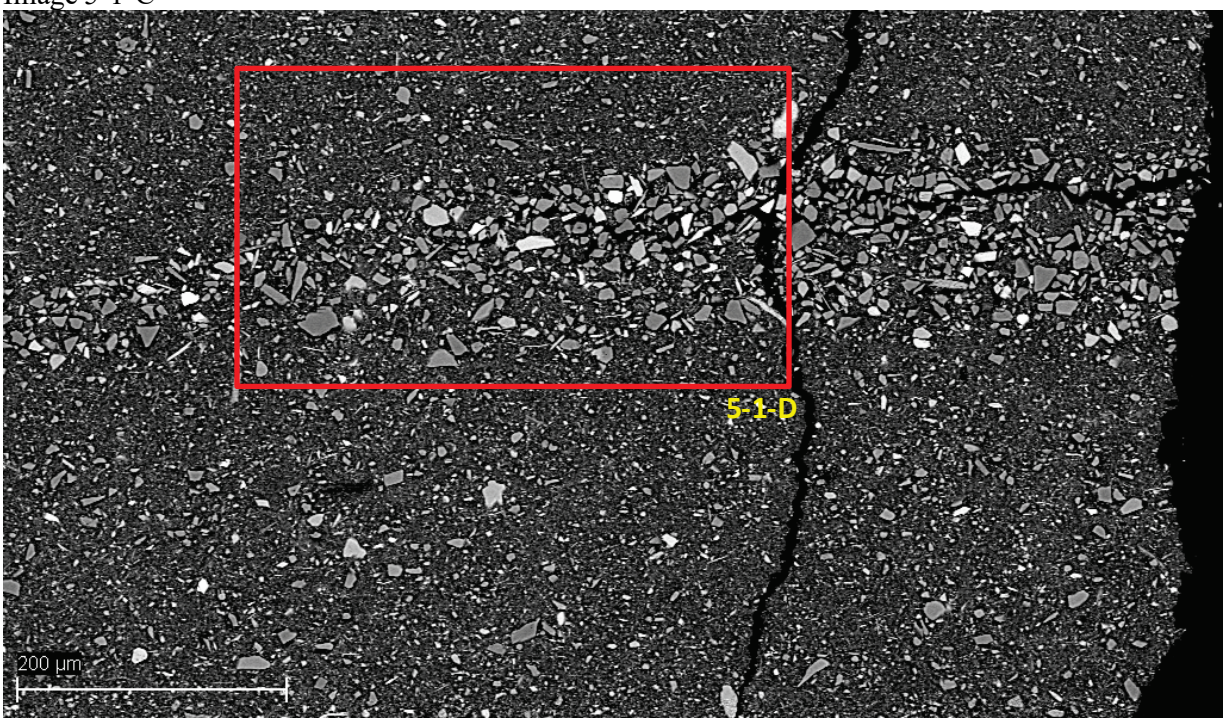

Figure A-2. BSE micrograph showing sub-horizontal coarse silt lamina of variable thickness with poorly-sorted angular to sub-angular clasts. Cracks induced from impregnation and thin section preparation.

Image 5-1-D

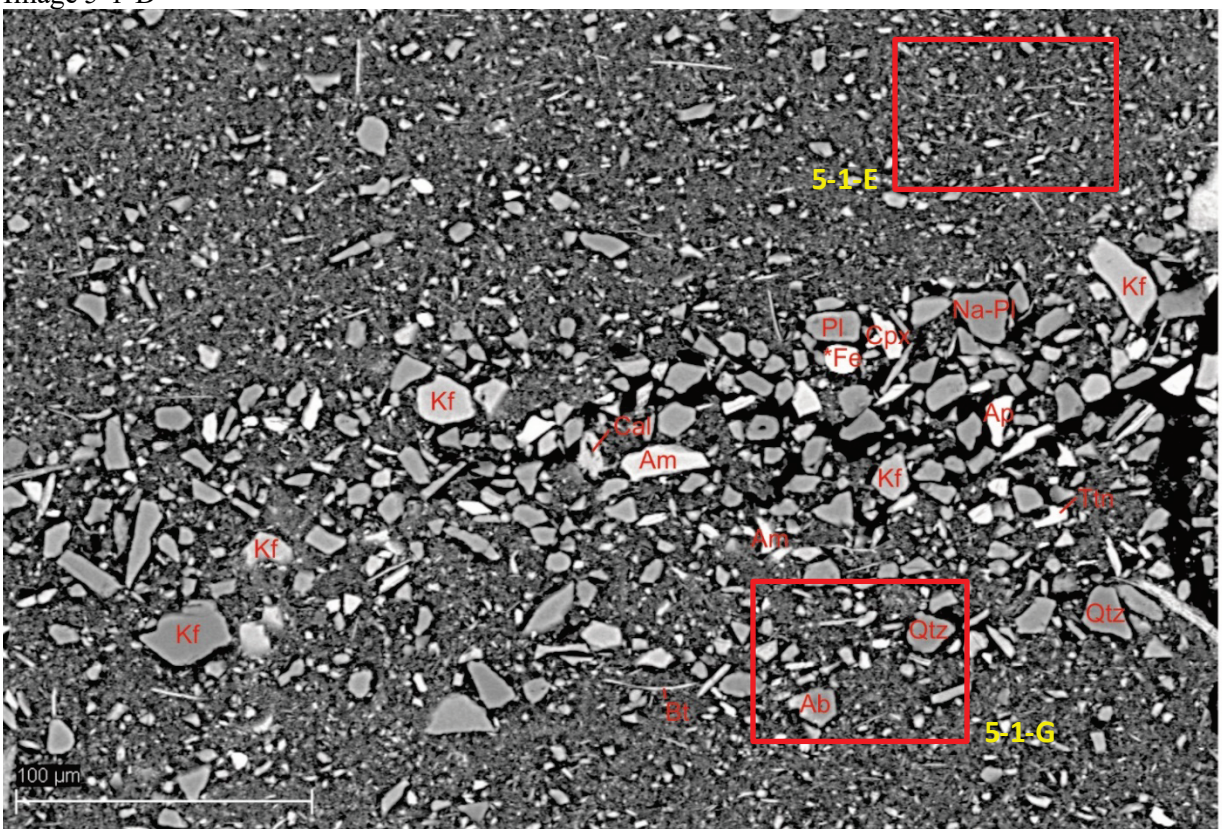

Figure A-3. BSE micrograph showing detail of silt lamina boxed in Figure A-2. The silt lamina ranges from matrix- to clast-supported, with grains that are angular to sub-angular and randomly-oriented. The fine-grained matrix within the silt lamina consists of both unoriented and sub-horizontal biotite grains (Ab=albite, Am=Amphibole, Ap=apatite, Bt=biotite, Cal=calcite, Cpx=clinopyroxene, Fe=iron oxide, Kf=potassium feldspar, Na-Pl=sodic plagioclase, Pl=plagioclase, Qtz=Quartz, Ttn=titanite).

Image 5-1-E

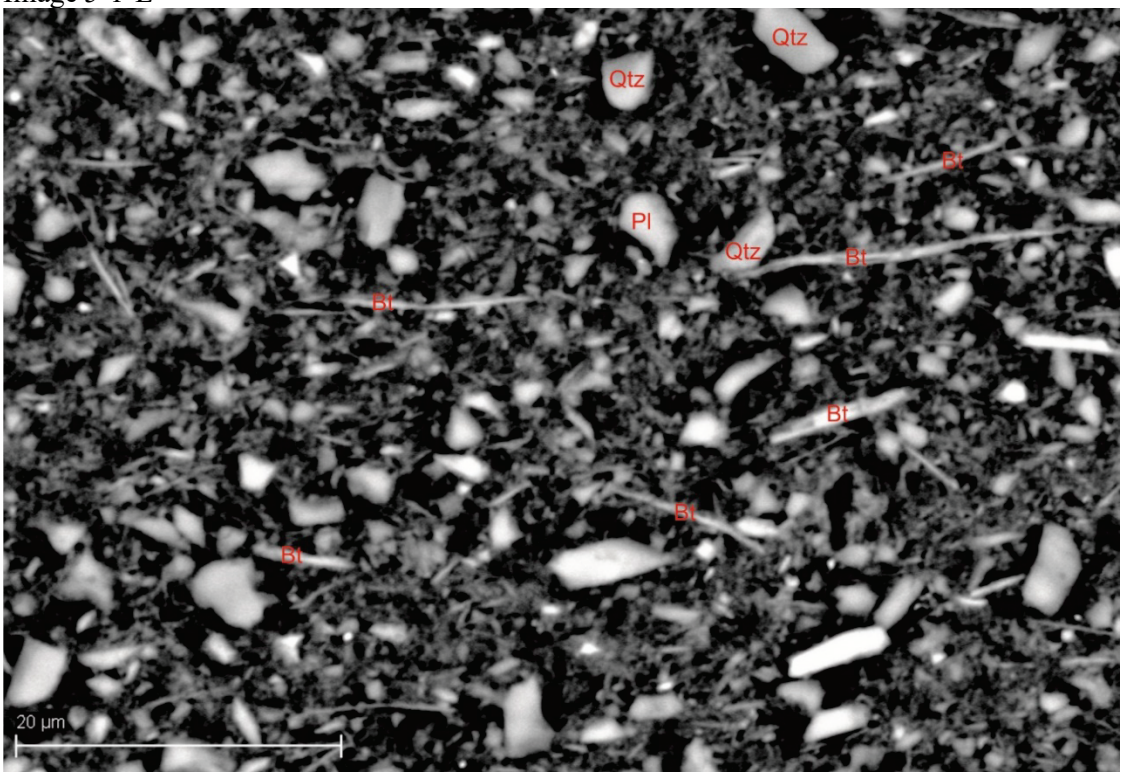

Figure A-4. BSE micrograph showing detail of clay matrix (upper box in Figure A-3). Biotite grains are primarily sub-horizontal and other silt-size silicate minerals appear randomly-oriented. Matrix composed primarily of biotite and amphibole with fine to medium silt grains of biotite (Bt), quartz (Qtz) and plagioclase (Pl) identified.

Image 5-1-G

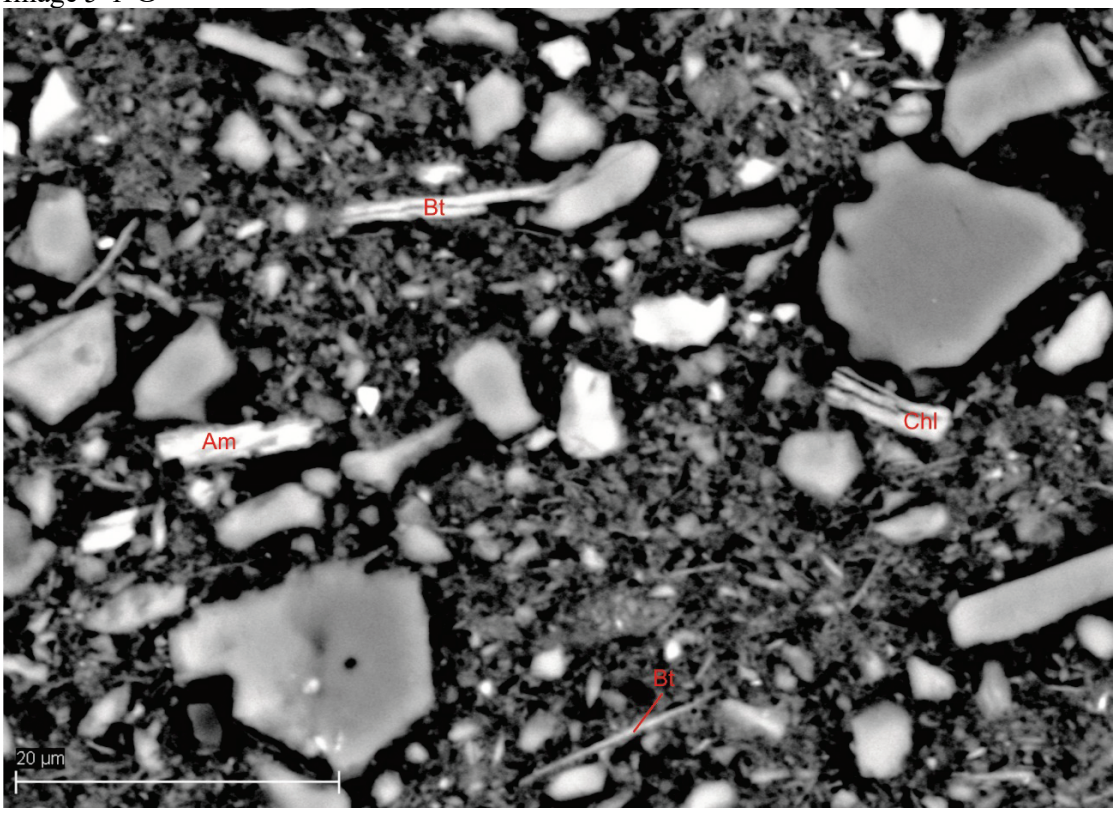

Figure A-5. BSE micrograph showing detail of clay matrix (lower box in Figure A-3). Grains within clay-size matrix appear randomly-oriented and are composed mostly of biotite and amphibole. Silt-size biotite grains are primarily sub-horizontal (Am=amphibole, Bt=biotite, Chl=chlorite).

Image 5-1-H

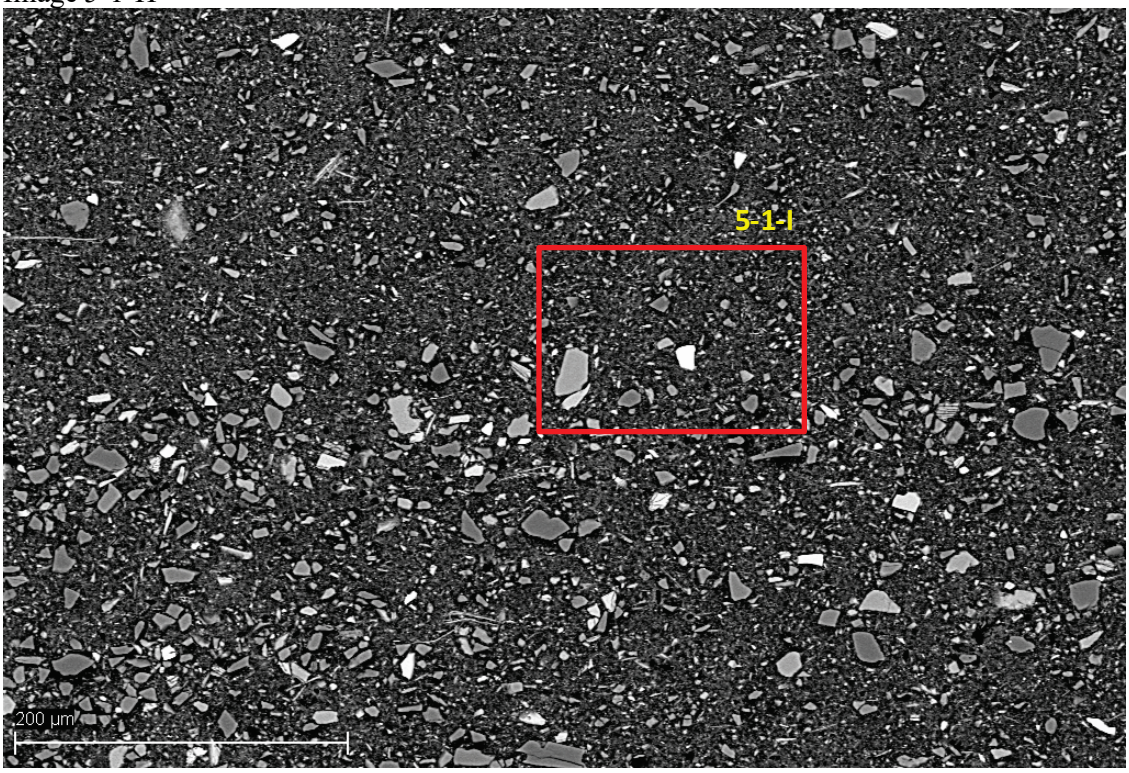

Figure A-6. BSE micrograph showing detail of an area containing laterally discontinuous silt laminae.

Image 5-1-I

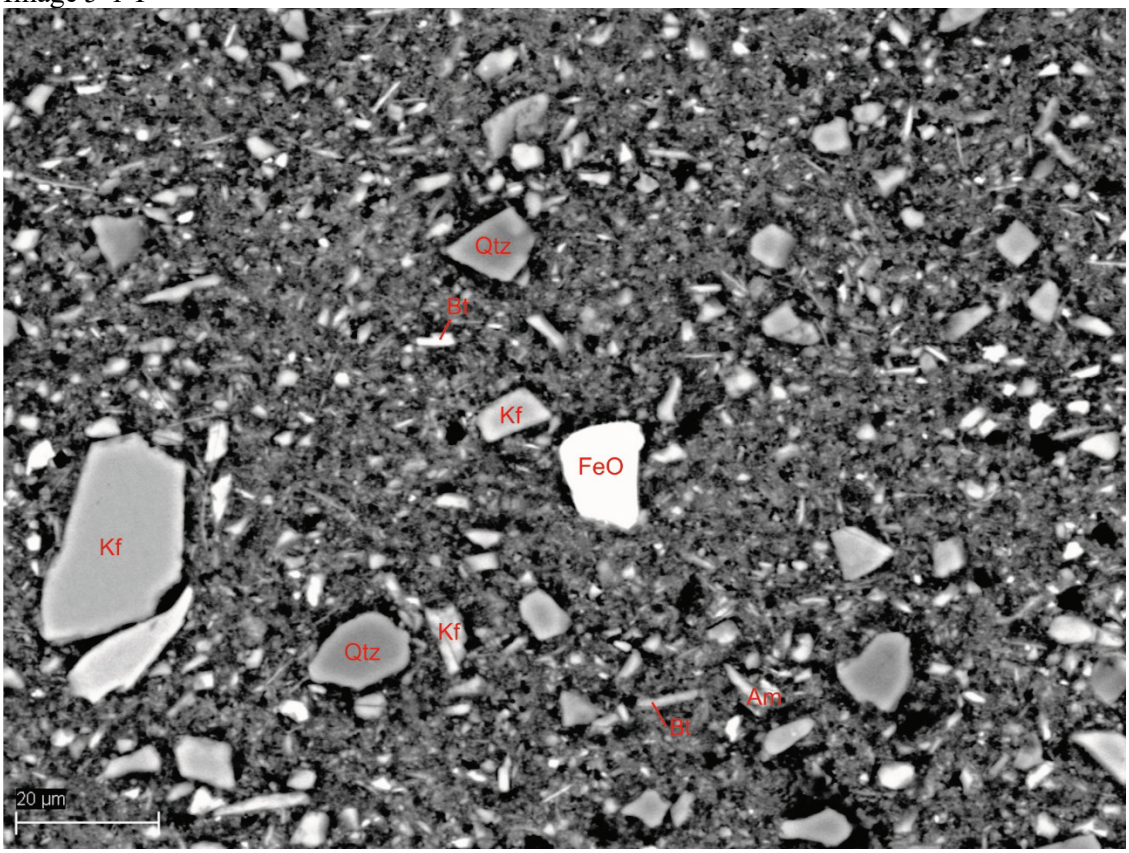

Figure A-7. BSE micrograph showing detail of clay matrix (area boxed in Figure A-6). Grains appear randomly-oriented within clay-size matrix, which is primarily composed of biotite and amphibole (Am=Amphibole, Bt=biotite, Fe=iron oxide, Kf=potassium feldspar, Qtz=Quartz).

Image 5-1-J

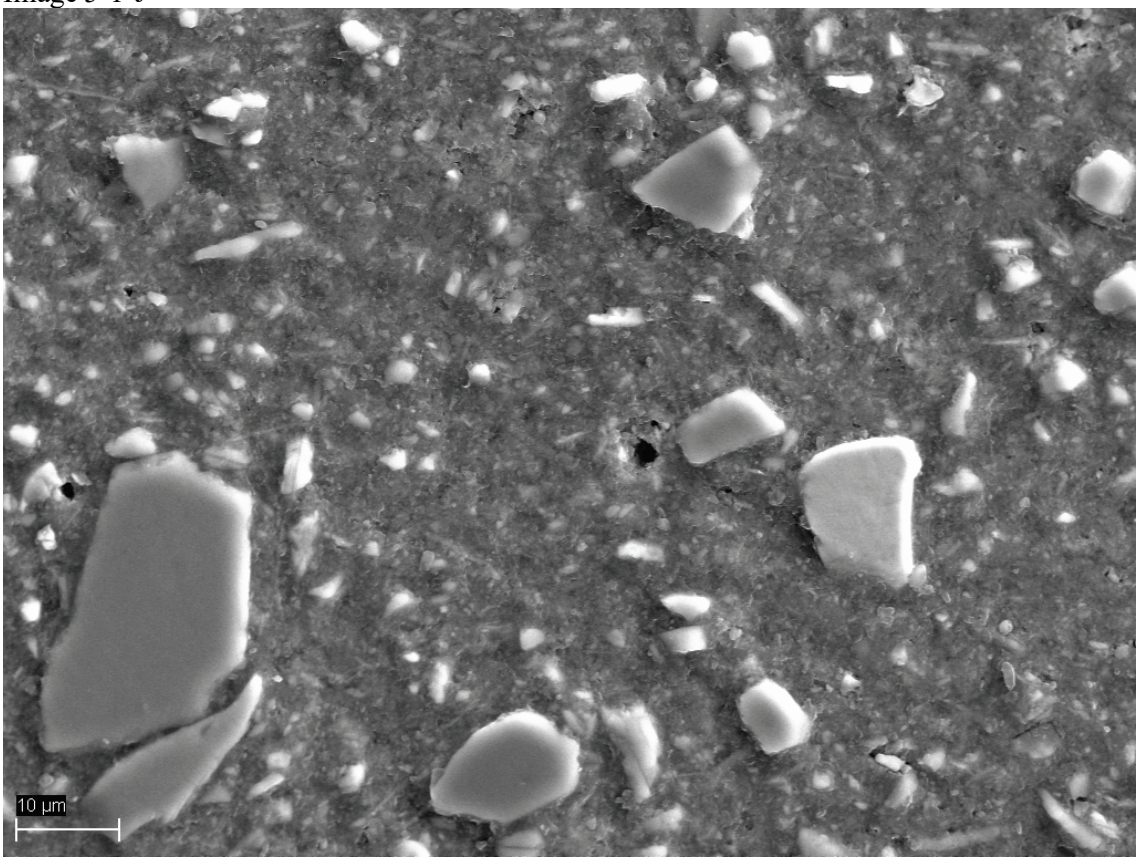

Figure A-8. Secondary electron (SE) micrograph (of Figure A-7) showing a topographical relief of the surface of the polished thin section. The silt-size particles with higher density are differentiated from the softer matrix. A black pit can be seen in the middle of the thin section where a grain was likely plucked out during polishing.

Image 5-2-A

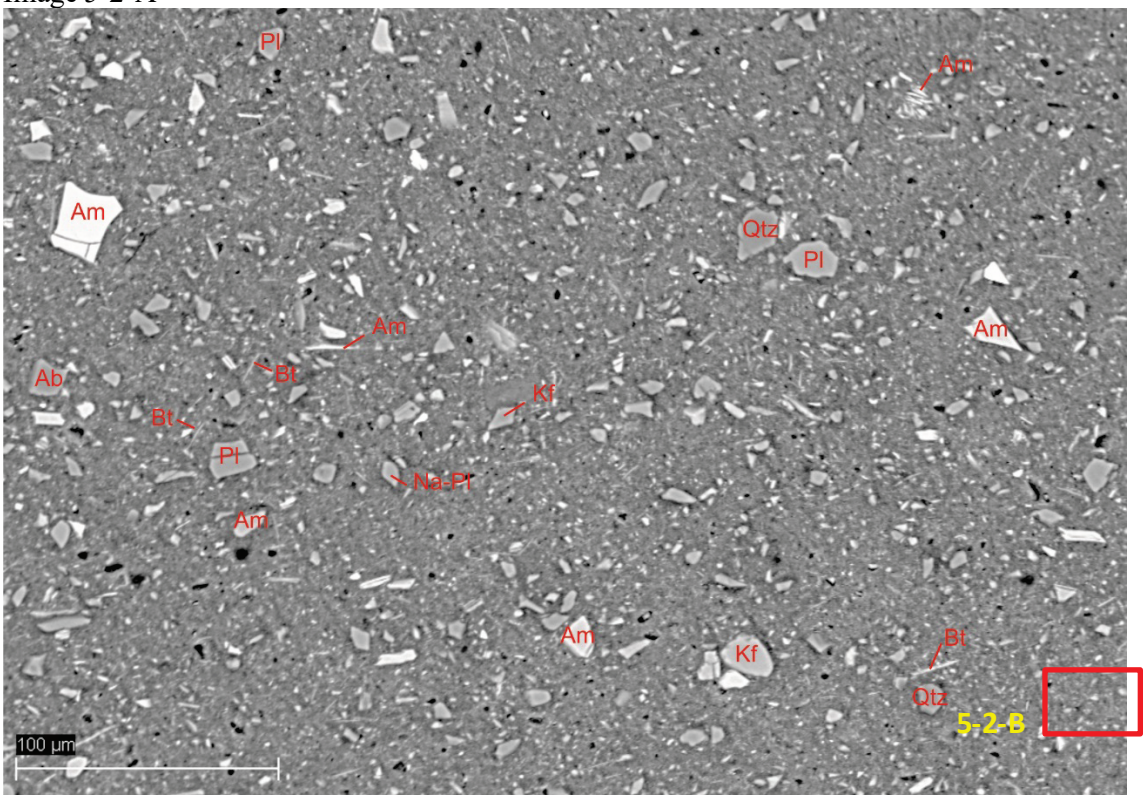

Figure A-9. BSE micrograph showing massive texture consisting of randomly-oriented detrital grains (Ab=albite, Am=Amphibole, Bt=biotite, Kf=potassium feldspar, Na-Pl=sodic plagioclase, Pl=plagioclase, Qtz=Quartz).

Image 5-2-B

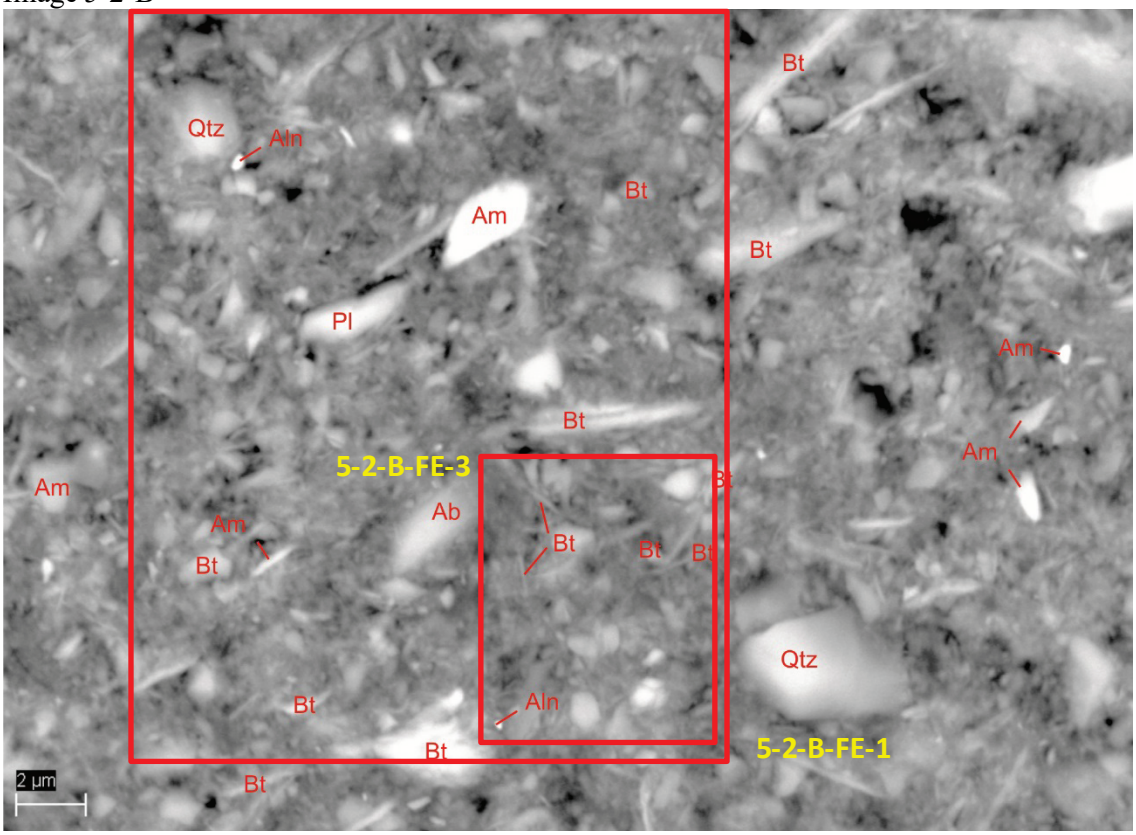

Figure A-10. BSE micrograph showing detail of randomly-oriented clay matrix (area boxed in Figure A-9). Matrix is primarily composed of biotite and amphibole (Ab=albite, Aln=allanite, Am=Amphibole, Bt=biotite, Qtz=Quartz).

Image 5-2-B-FE-1

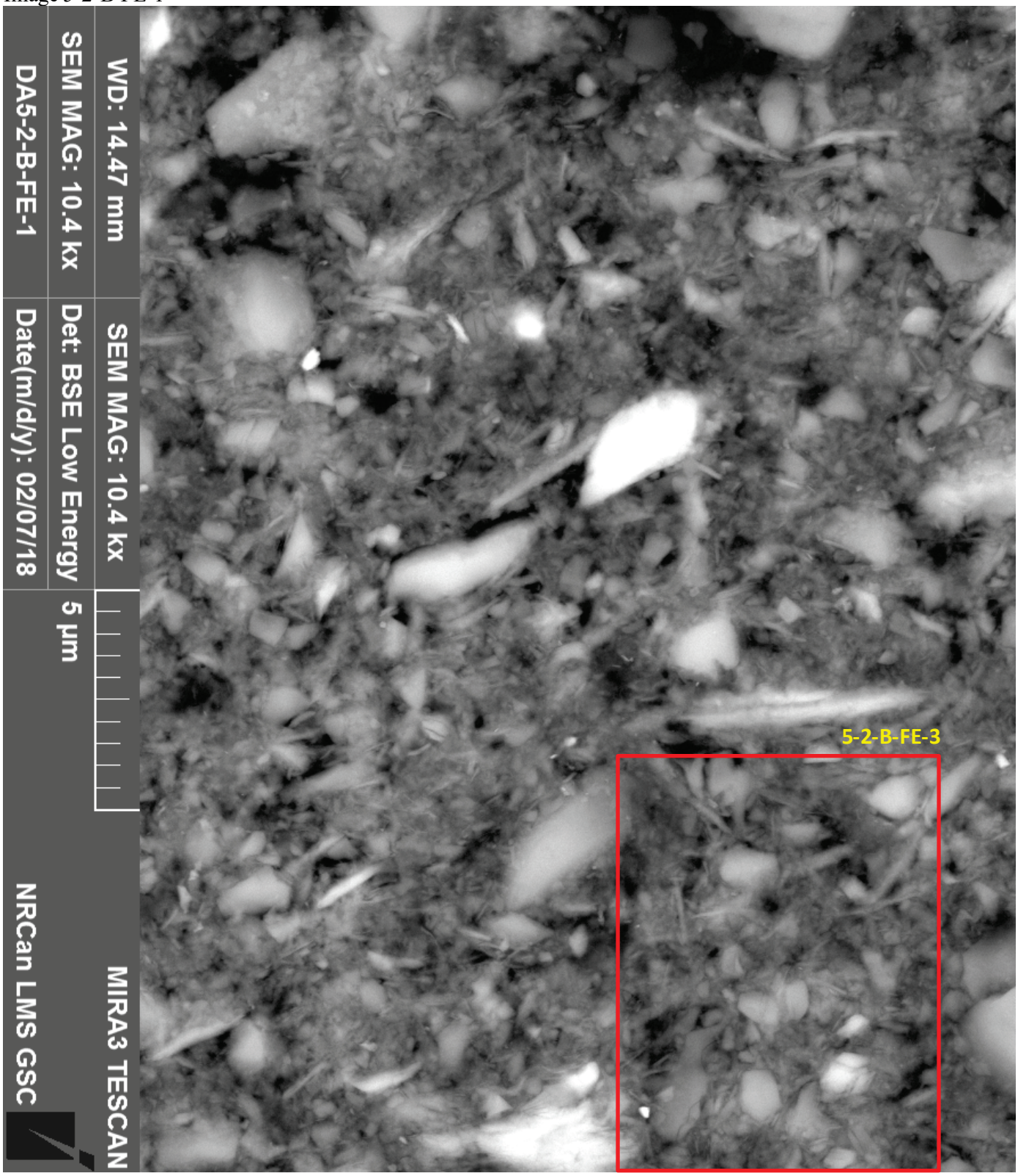

Figure A-11. BSE-Field Emission (FE) micrograph of area boxed in Figure A-10, showing increased resolution of randomly-oriented fine silt grains in a clay-size matrix. Image is oriented to show the upward direction.

Image 5-2-B-FE-3

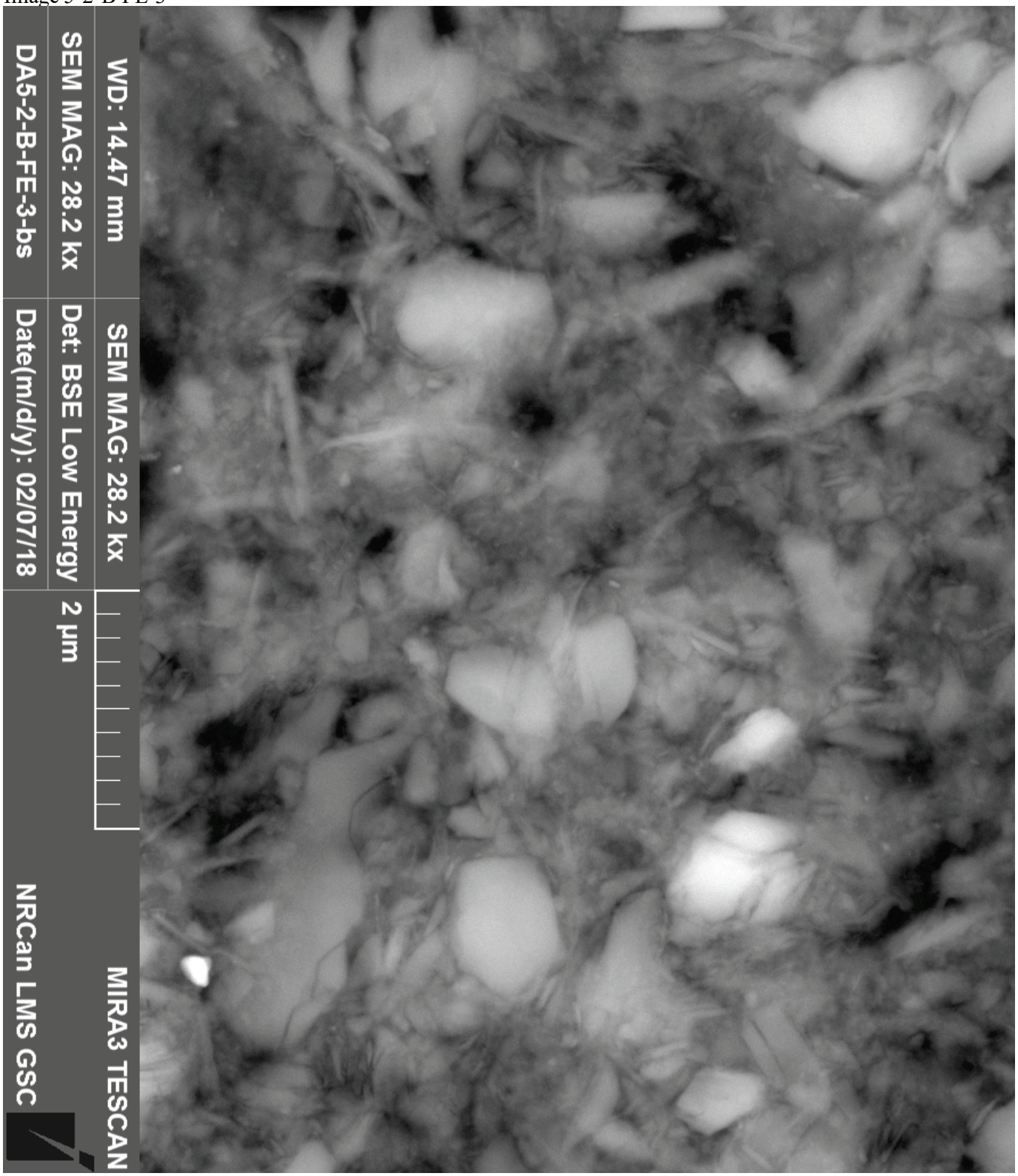

Figure A-12. BSE-FE micrograph of area boxed in Figures A-10 and A-11, showing highest resolution (sub-micron-scale) of randomly-oriented clay-size grains. Image is oriented to show the upward direction.

Image 5-3-A

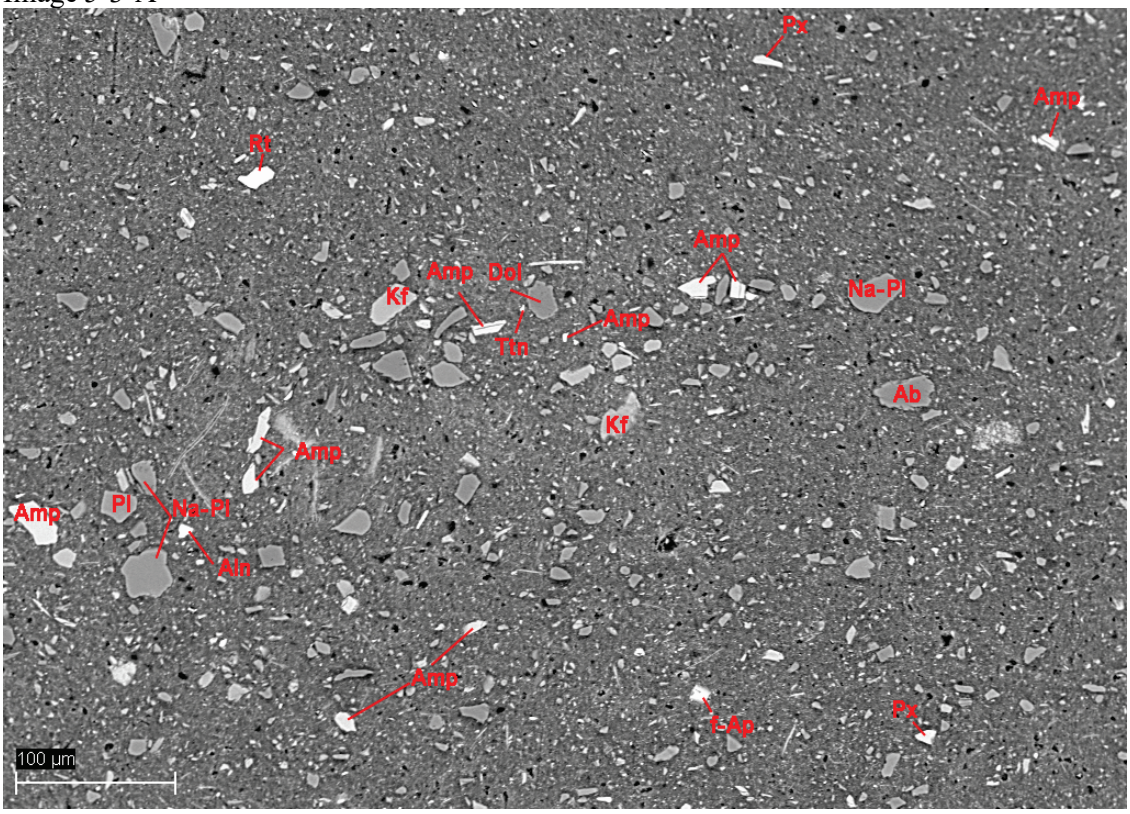

Figure A-13. BSE micrograph showing an area containing silt lenses within clay matrix (Ab=albite, Aln=allanite, Am=Amphibole, Bt=biotite, Dol=dolomite, fAp=fluoroapatite, Kf=potassium feldspar, Na-Pl=sodic plagioclase, Pl=plagioclase, Px=pyroxene, Qtz=Quartz, Rt=rutile, Ttn=titanite).

Image 5-3-C

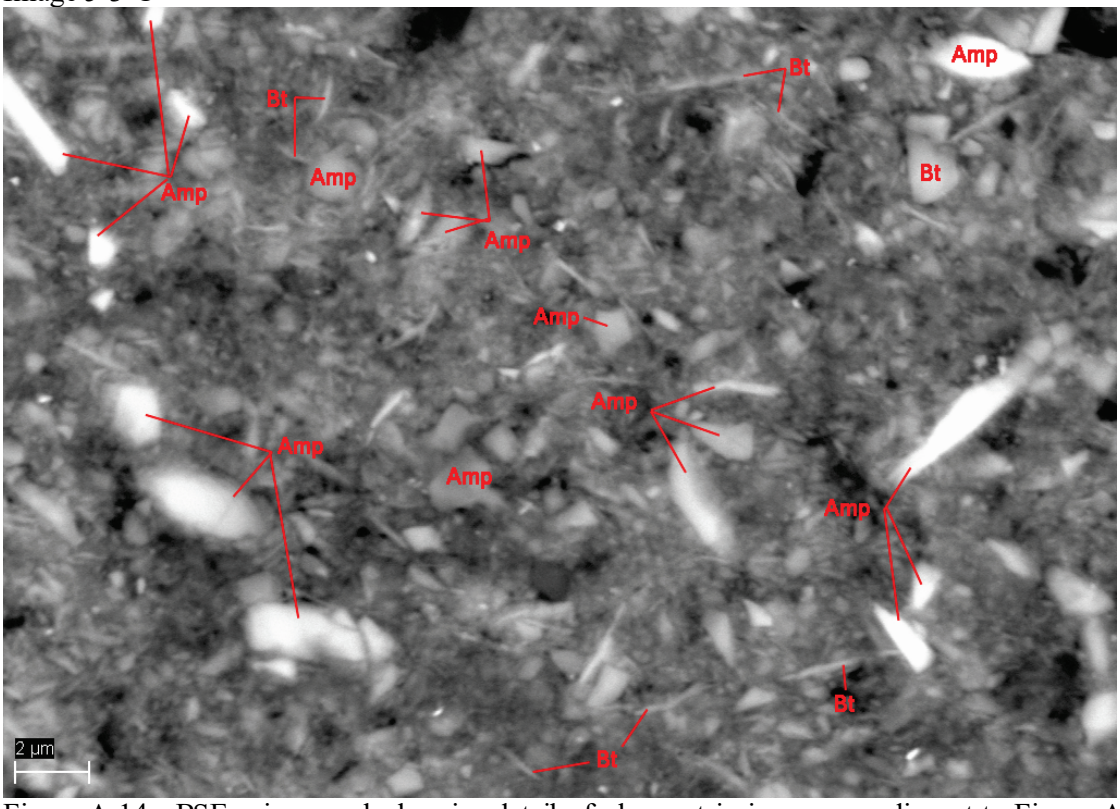

Figure A-14. BSE micrograph showing detail of clay matrix in an area adjacent to Figure A-13. Grains are randomly-oriented and are primarily biotite (Bt) and amphibole (Amp).

Grain Mount Image 5-1

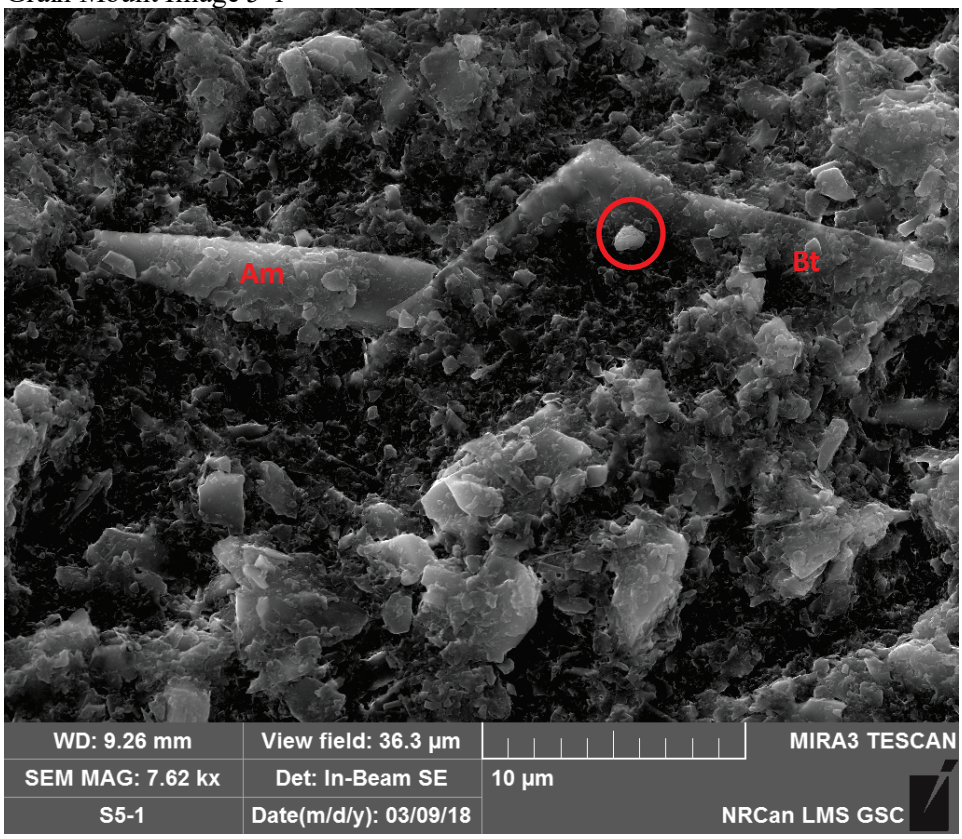

Figure A-15. BSE-FE micrograph of grain mount (unoriented), showing biotite platelets covering silt-size grains of amphibole (Am) and biotite (Bt). Circled grain is a clay-size iron oxide mineral.

Grain Mount Image 5-5

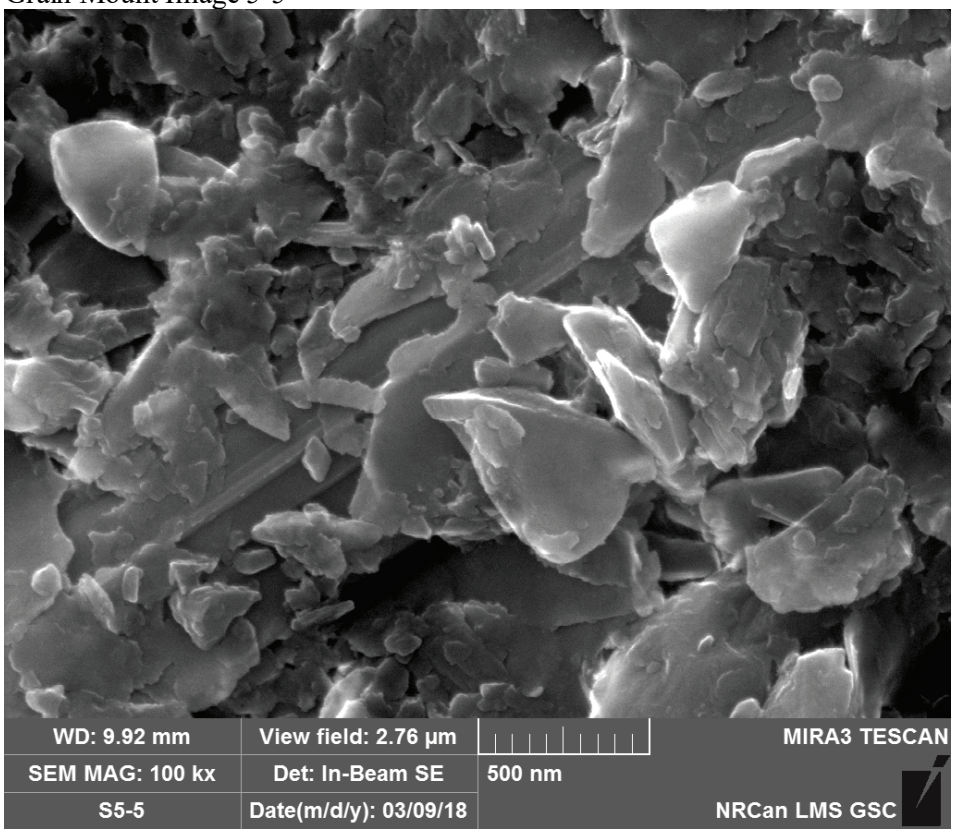

Figure A-16. BSE-FE micrograph of grain mount (unoriented) showing biotite platelets at the nanoscale.

Sample 13 – depth range: 32.72 – 32.77 m

Image 13-1-B

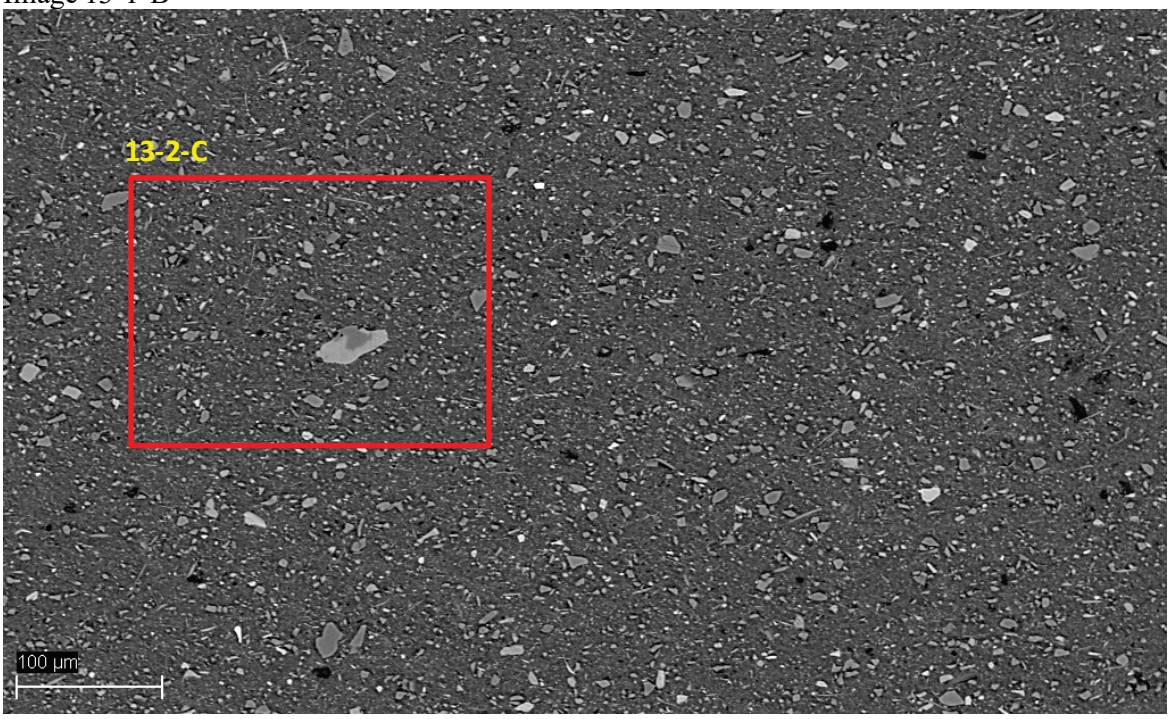

Figure A-17. BSE micrograph showing massive texture of sediment, with an absence of laminae or lenses. Grain size ranges from coarse silt (50 µm) to clay (≤2 µm).

Image 13-1-C

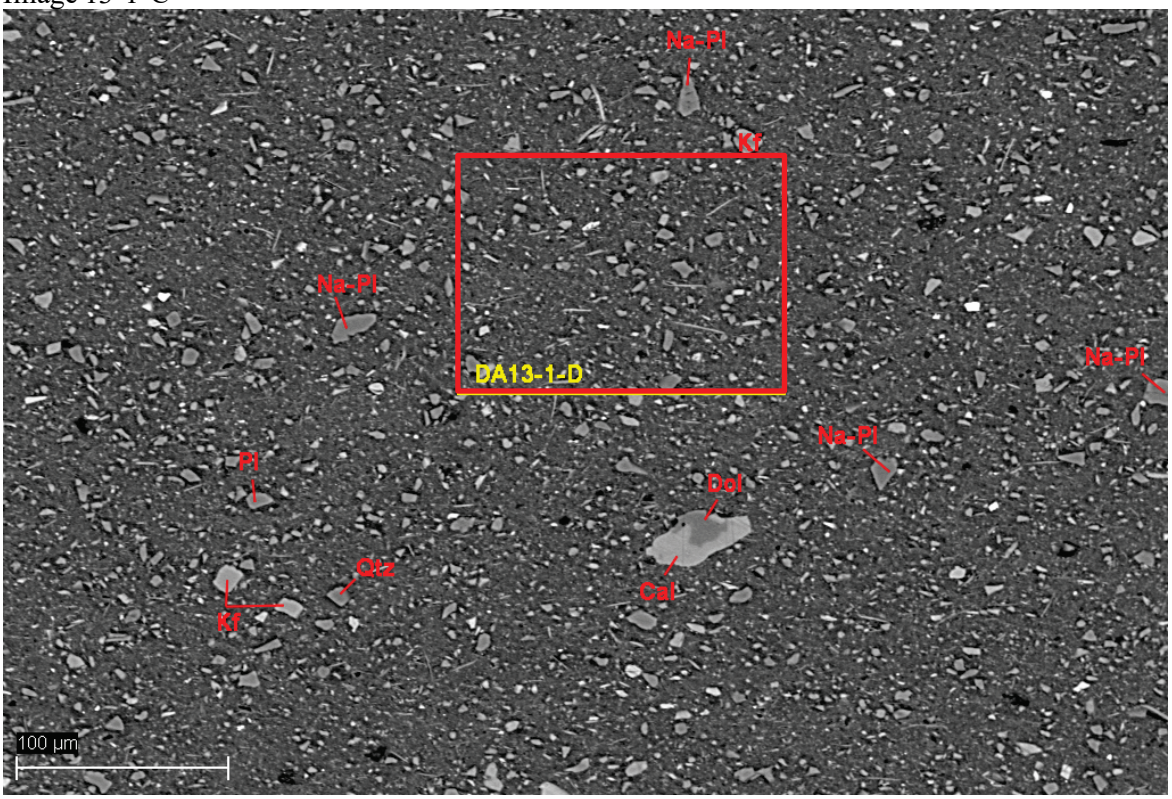

Figure A-18. BSE micrograph showing detail of area boxed in Figure A-17 (Cal=calcite, Dol=dolomite, Kf=potassium feldspar, NA-Pl=sodic plagioclase, Pl=plagioclase).

Image 13-1-D

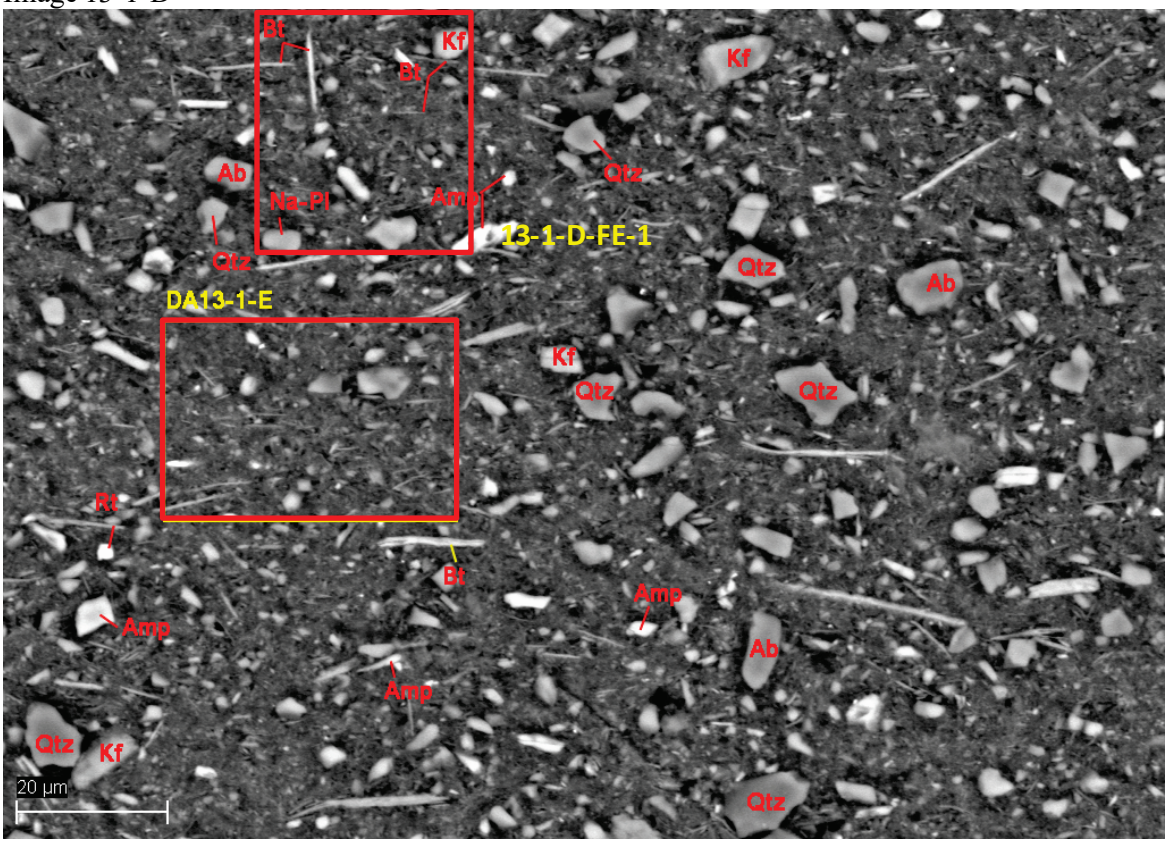

Figure A-19. BSE micrograph of area boxed in Figure A-18 showing fairly consistent horizontal to sub-horizontal alignment of silt-size biotite grains (Ab=albite, Am=Amphibole, Ap=apatite, Bt=biotite, Kf=potassium feldspar, Na-Pl=sodic plagioclase, Pl=plagioclase, Qtz=Quartz).

Image 13-1-D-FE-1

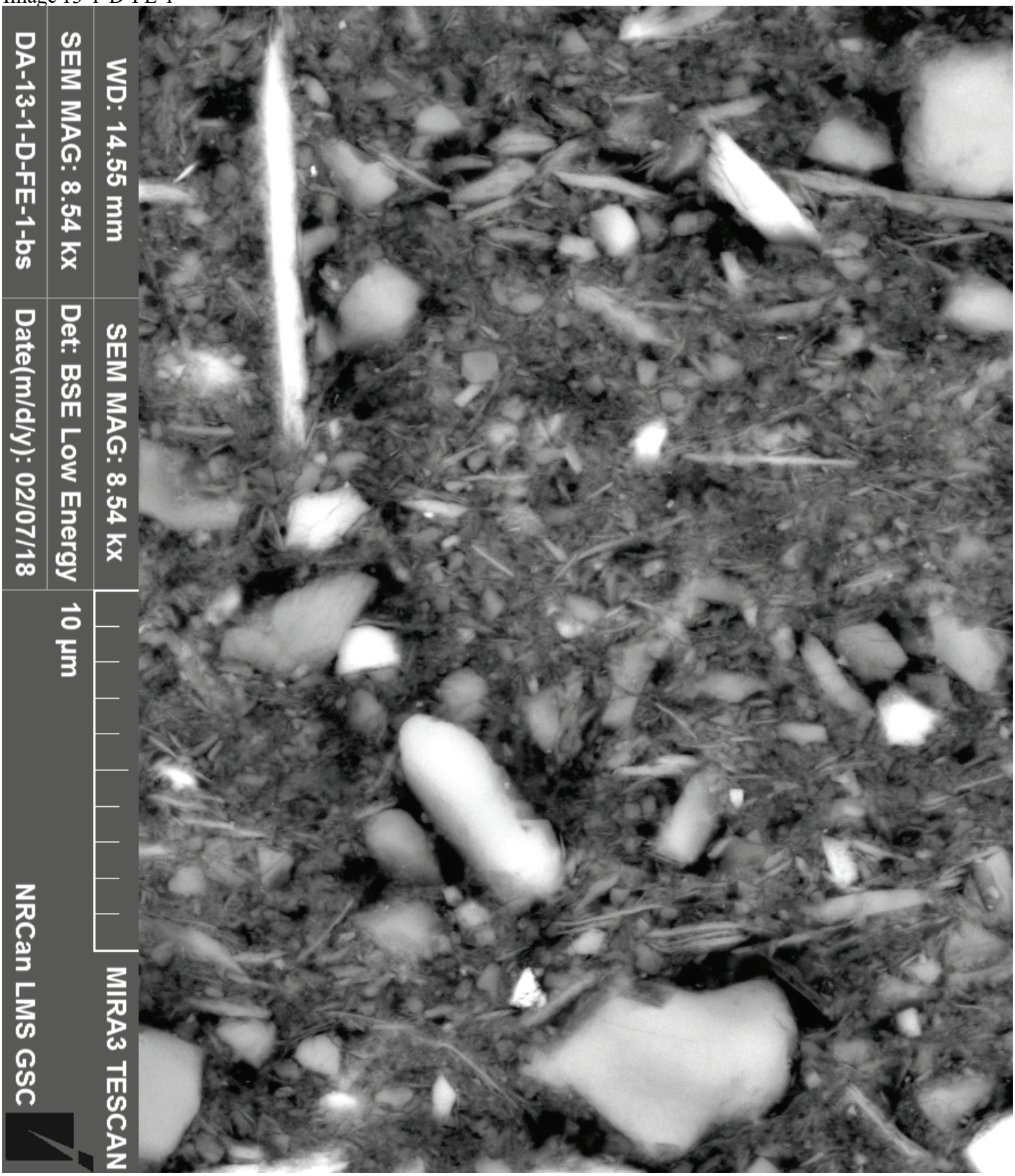

Figure A-20. BSE-FE micrograph of area boxed in Figure A-19, showing some alignment of clay-size biotite grains, with more randomly-oriented silt-size grains. Image is rotated to show the upward direction.

Image 13-1-E

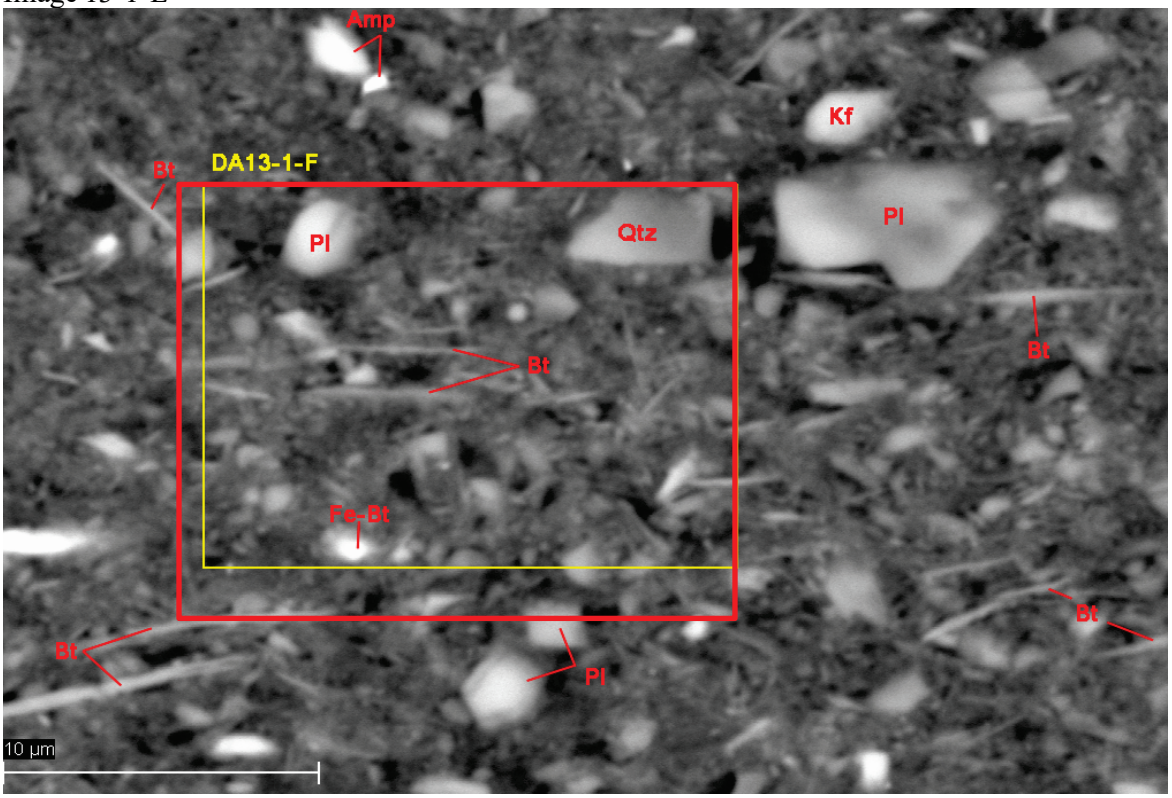

Figure A-21. BSE micrograph showing detail of area boxed in Figure A-19 (Am=amphibole, Bt=biotite, Fe-Bt=iron rich biotite, Kf=potassium feldspar, Pl=plagioclase, Qtz=Quartz).

Image 13-1-F

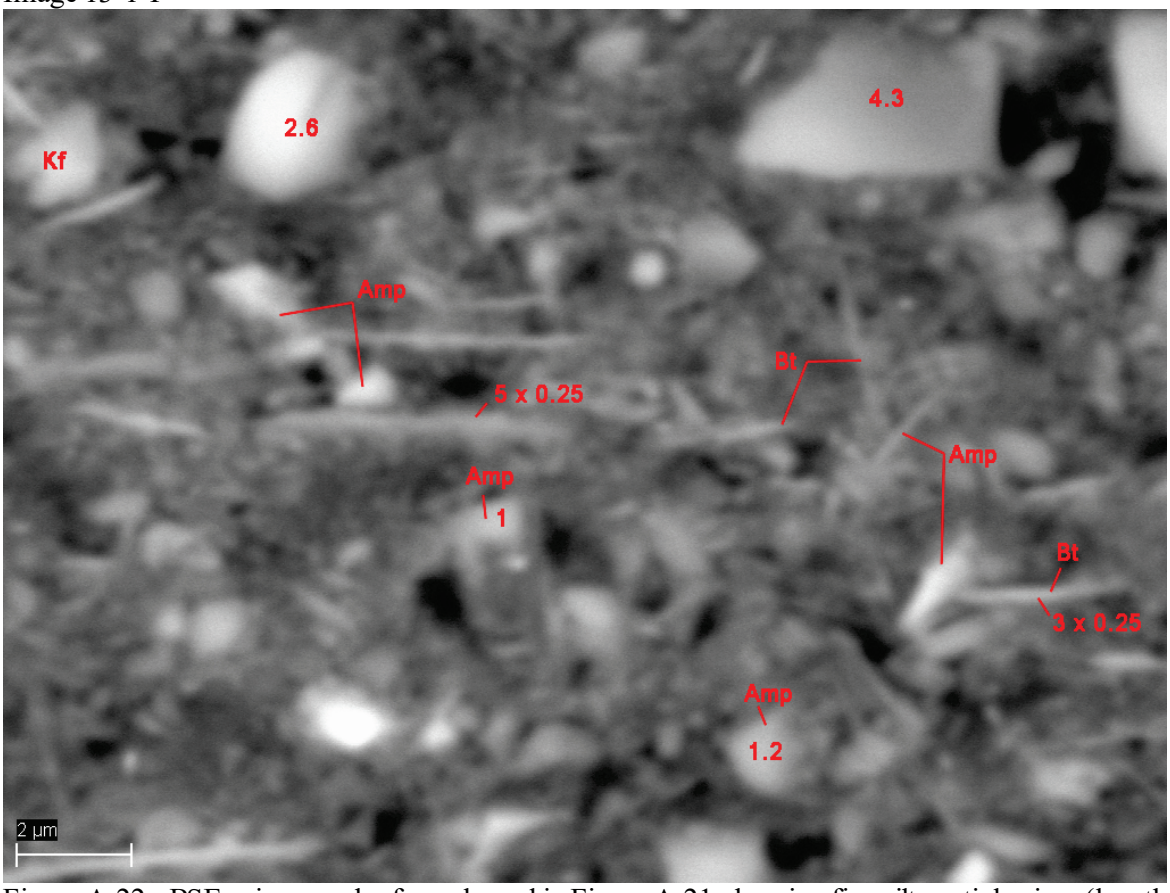

Figure A-22. BSE micrograph of area boxed in Figure A-21 showing fine silt particle sizes (length x width, in microns) in clay matrix (Am=amphibole, Bt=biotite, Kf=potassium feldspar).

Image 13-1-D-FE-5

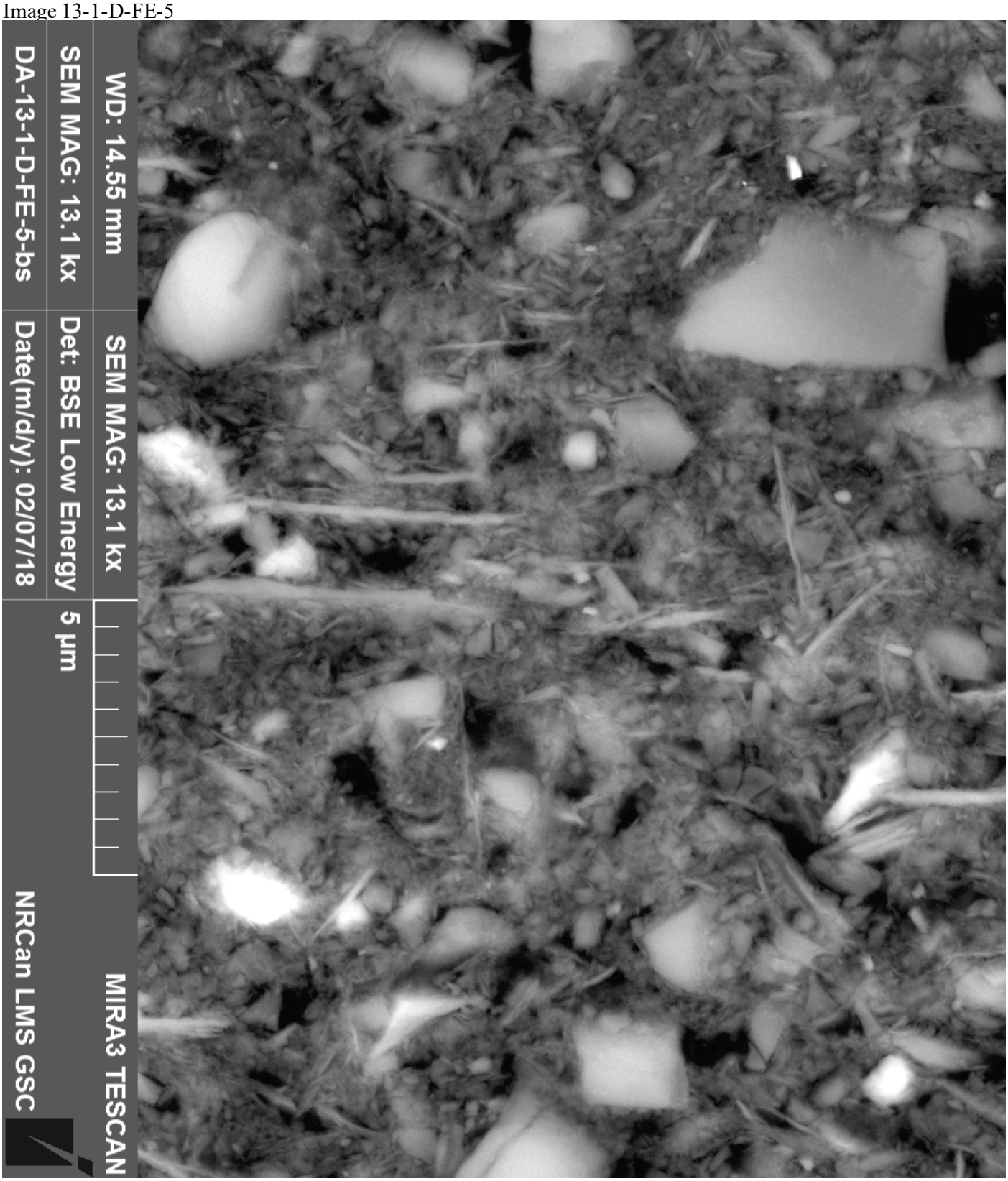

Figure A-23. Higher resolution image of Figure A-22 captured in BSE mode with the FE-SEM. Horizontal alignment of silt-size biotite grains is visible. Clay-size biotite grains appear more randomly-oriented, although many are also oriented parallel to bedding.

Image 13-2-A

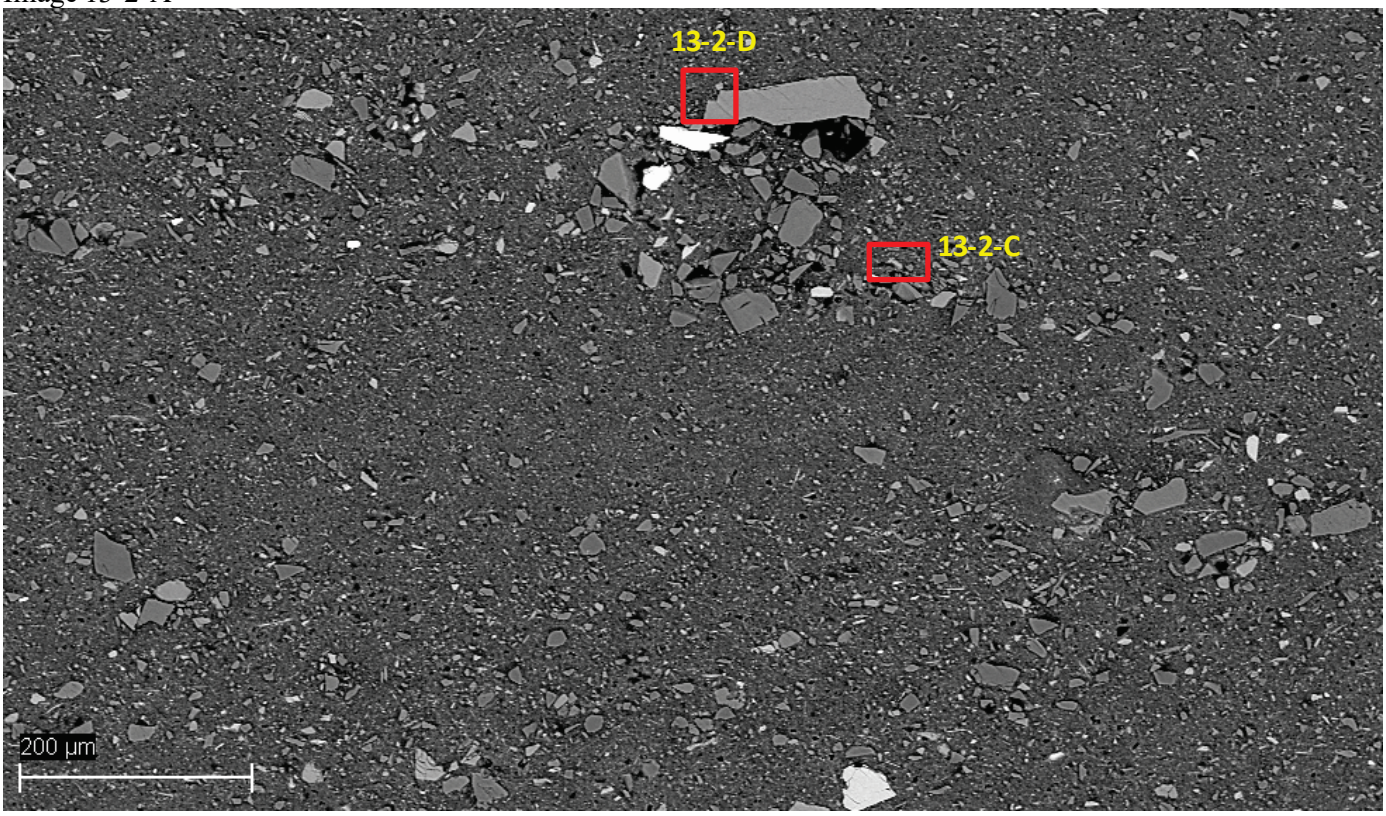

Figure A-24. BSE micrograph showing a coarse lens consisting of angular to sub-angular grains within a fine-grained matrix. Largest particle is fine sand-size (potassium feldspar).

Image 13-2-C

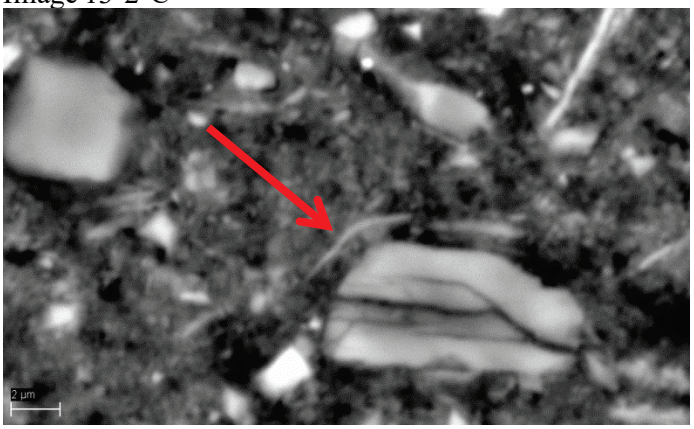

Figure A-25. Biotite curving or draping around a larger plagioclase grain suggests deformation due to compaction.

Image 13-2-D

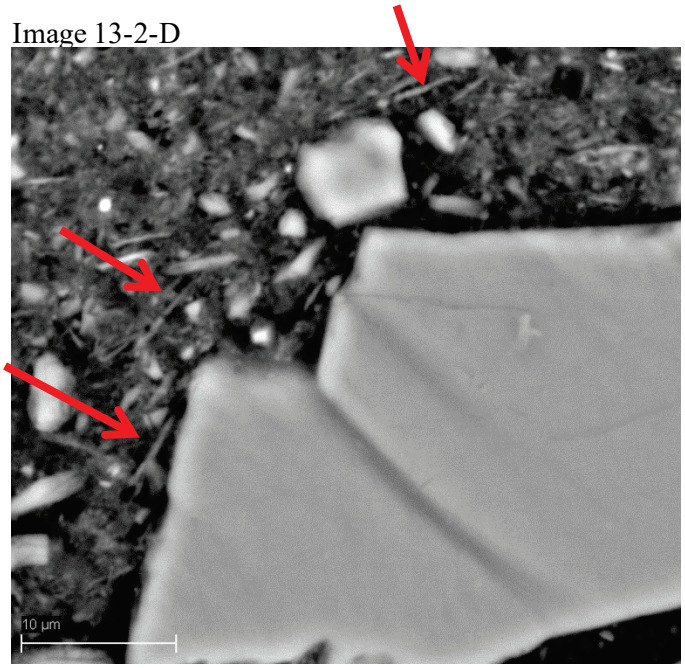

Figure A-26. Biotite grains showing alignment around potassium feldspar grain.

Image 13-3-B

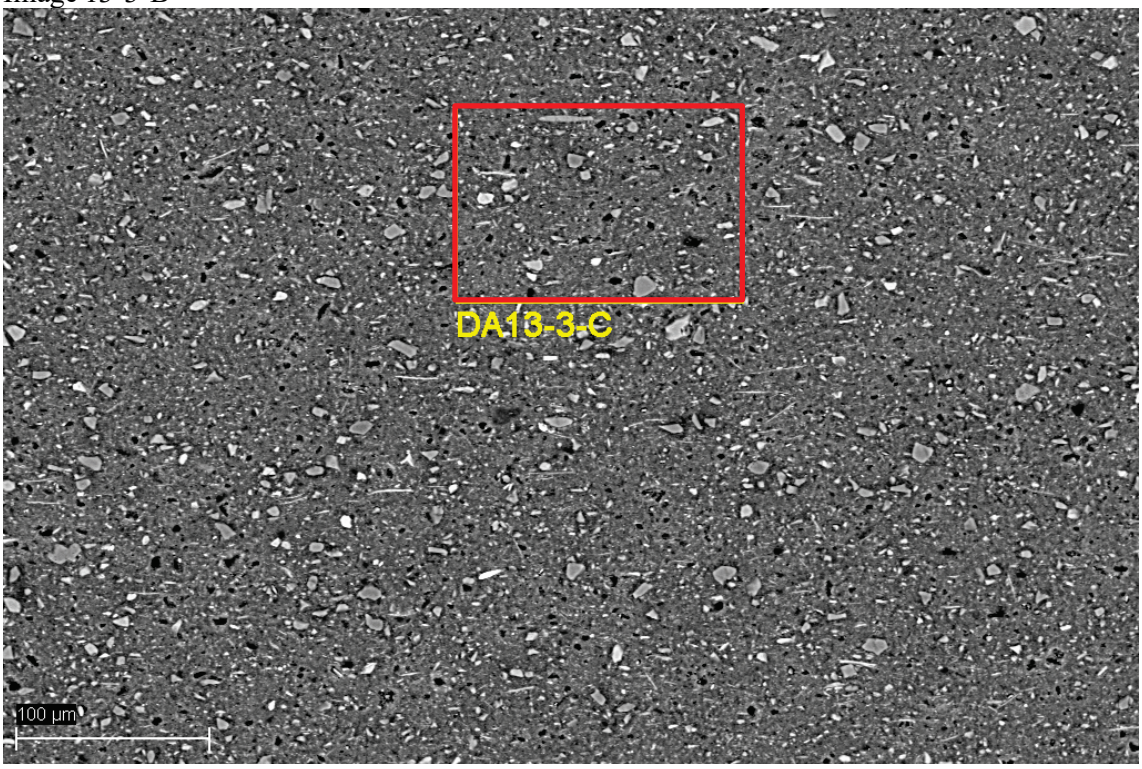

Figure A-27. BSE micrograph showing silt-size grains randomly distributed in a clay-size matrix. Biotite platelets and oblong sub-angular grains appear more horizontally to sub-horizontally aligned than in Sample 5.

Image 13-3-F

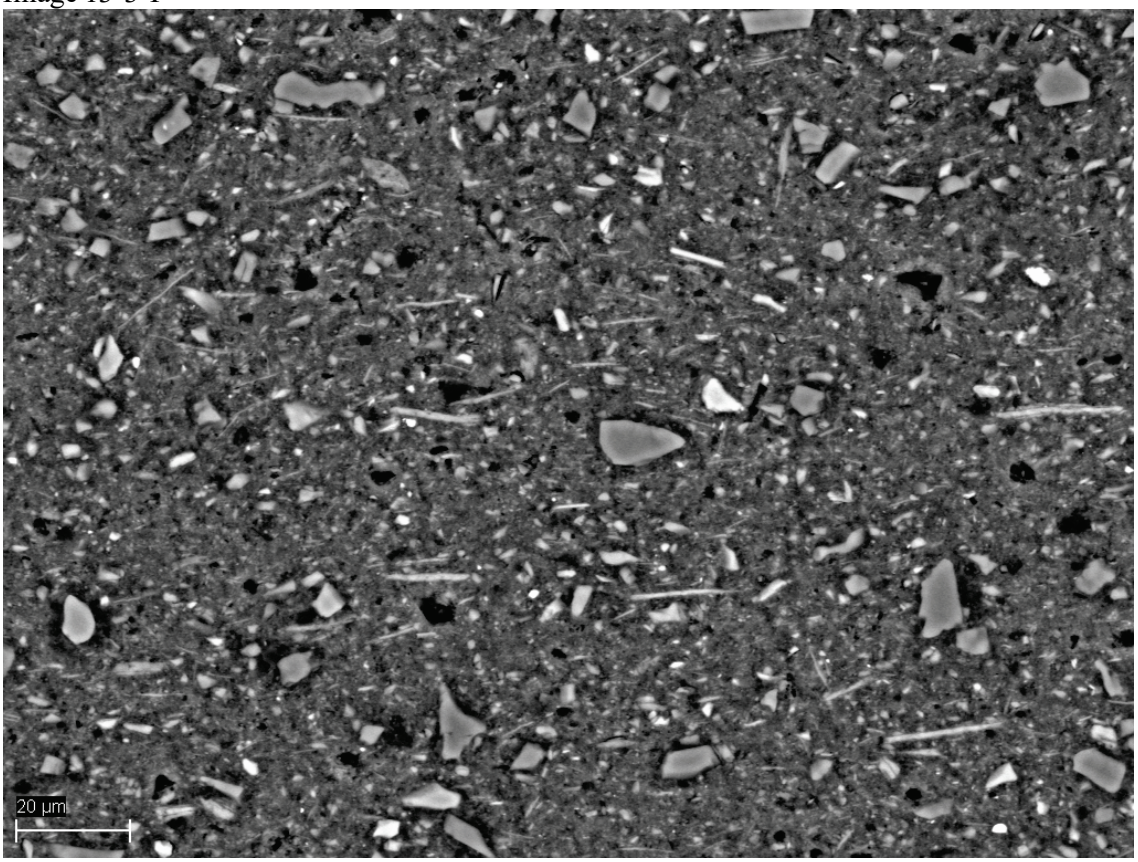

Figure A-28. BSE micrograph captured in an area just below Figure A-27 showing horizontally to sub-horizontally aligned biotite grains.

Image 13-3-C

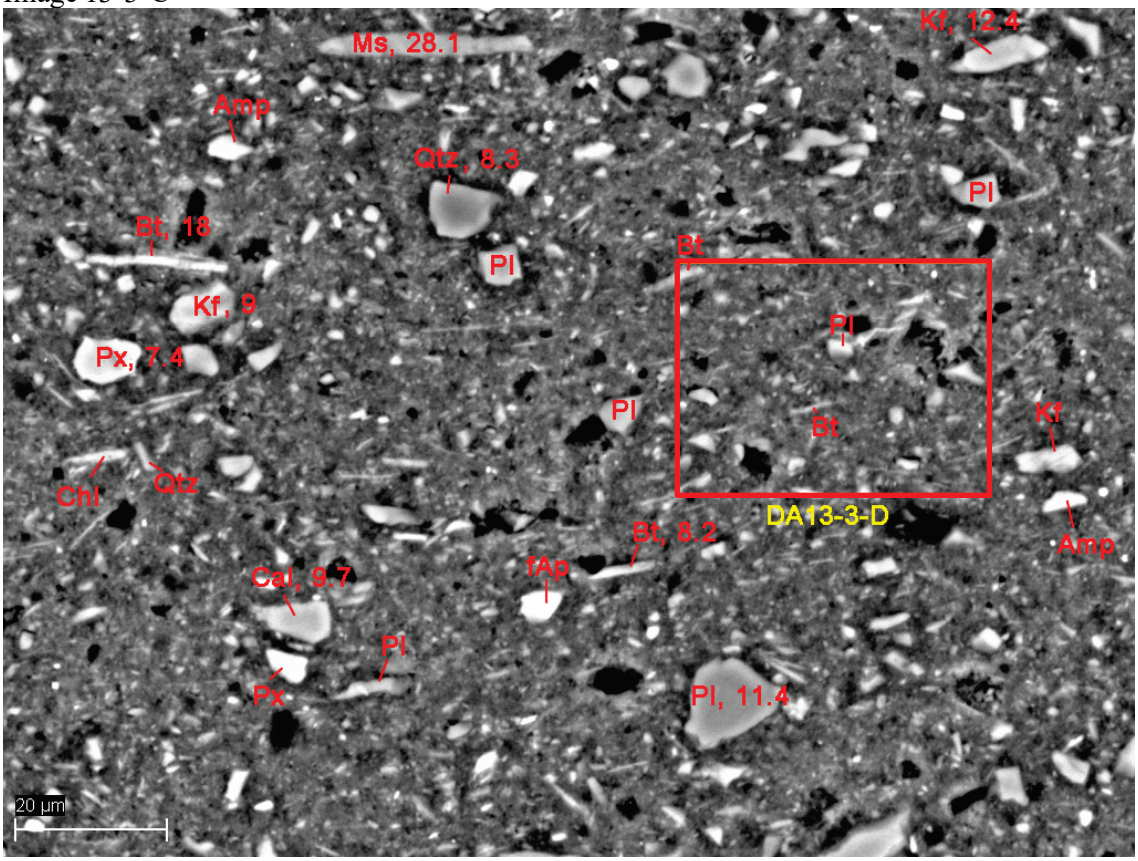

Figure A-29. BSE micrograph showing detail of area boxed in Figure A-27. Numbers show grain sizes in µm (Am=Amphibole, Bt=biotite, Cal=calcite, Chl=chlorite, fAp=fluoroapatite, Kf=potassium feldspar, Ms=muscovite mica, Pl=plagioclase, Px=pyroxene, Qtz=Quartz). Numerous black pits are visible in the thin section and are an artefact of thin section preparation.

Image 13-3-D

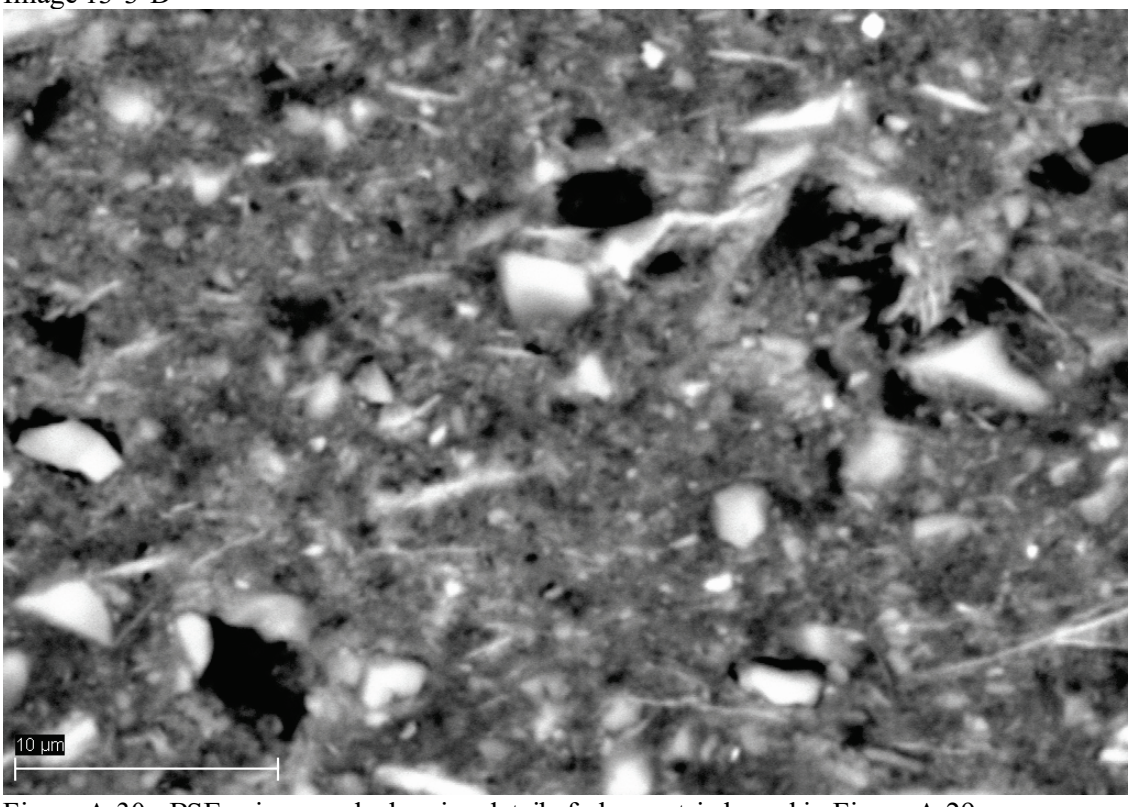

Figure A-30. BSE micrograph showing detail of clay matrix boxed in Figure A-29.

Grain Mount Image 13-5

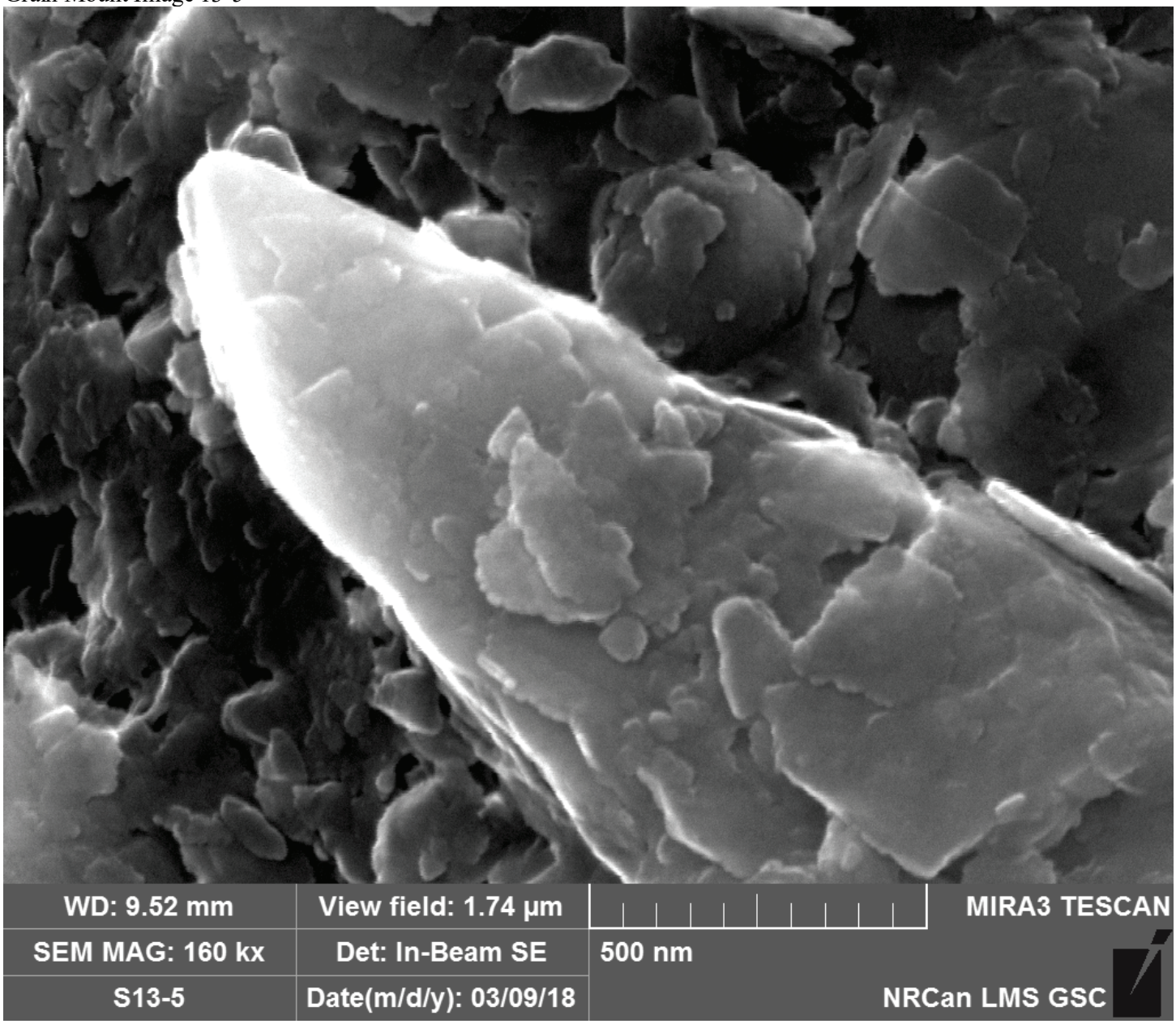

Figure A-31. SE-FE micrograph of grain mount (unoriented) showing a fine silt-size grain with plates appearing to flake off. Flaking of these plates may be a contributing source of clay-size grains. Thicknesses of flakes are approximately 10 nm.

Sample 21 – depth range: 59.55 – 59.59 m

Image 21-A2-1-A

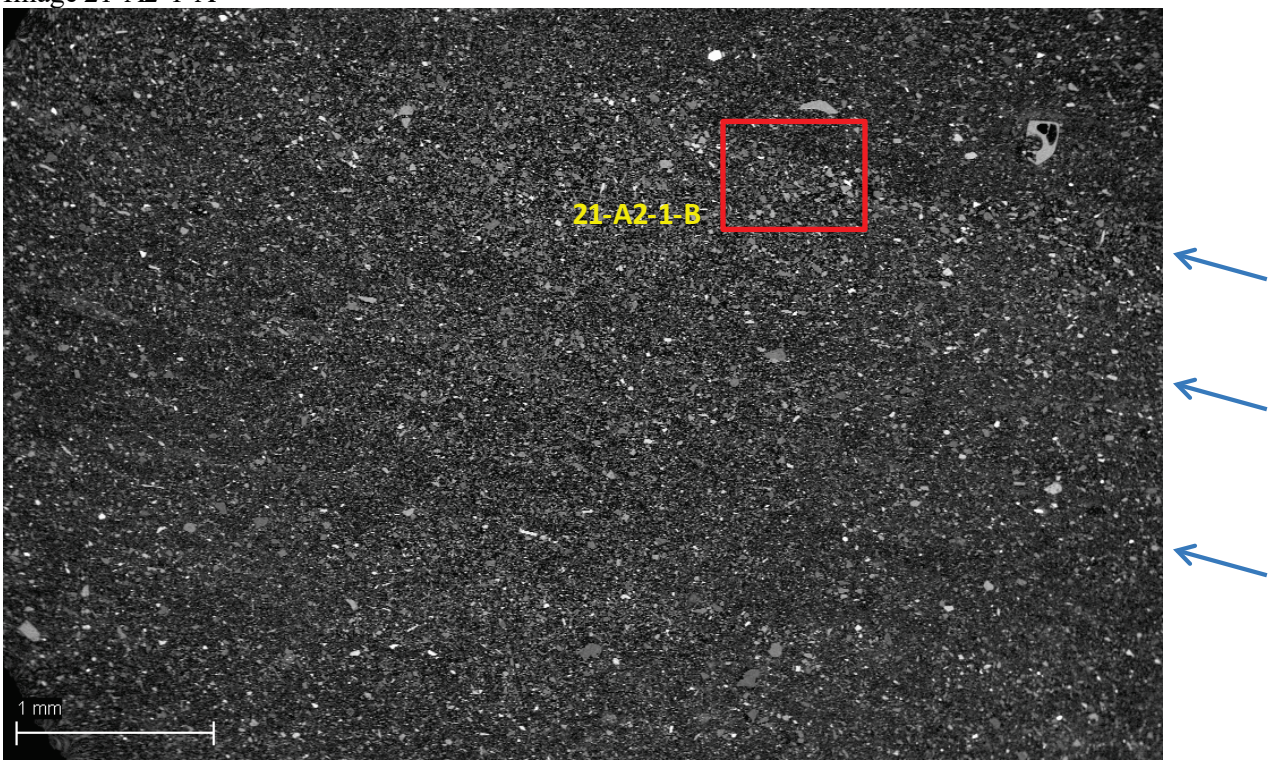

Figure A-32. BSE micrograph showing interstratified coarse (light) and fine (dark) sub-horizontal laminae. The contacts between the coarse and fine laminae are diffuse and generally indicated by arrows.

Image 21-A2-1-B

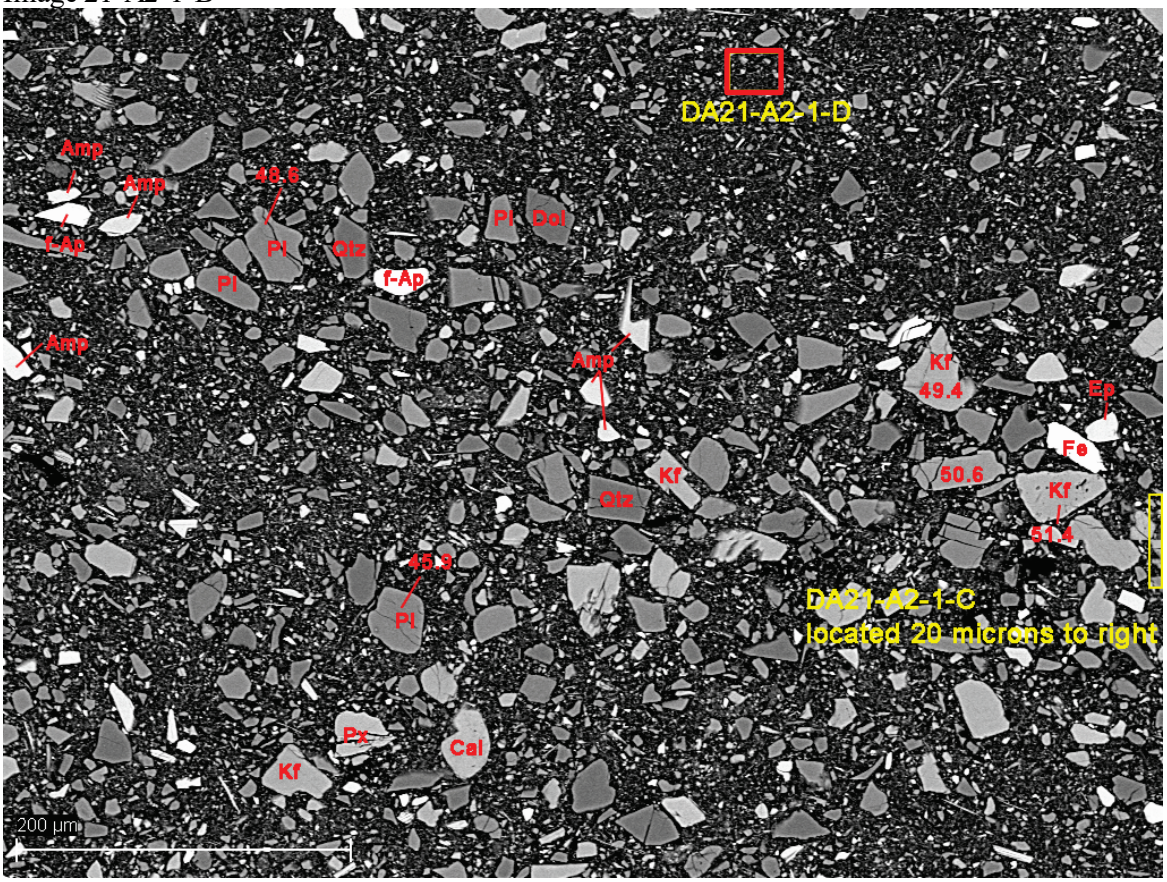

Figure A-33. BSE micrograph showing detail of area boxed in Figure A-32. Silt-rich (i.e., coarse) laminae are composed of angular to sub-angular, medium to coarse silt-size grains that are matrix-supported (Am=amphibole, Cal=calcite, Dol-dolomite, Ep=Epidote, Fe=iron oxide, fAp=fluoroapatite, Kf=potassium feldspar, Pl=plagioclase, Px=pyroxene).

Image 21-A2-1-D

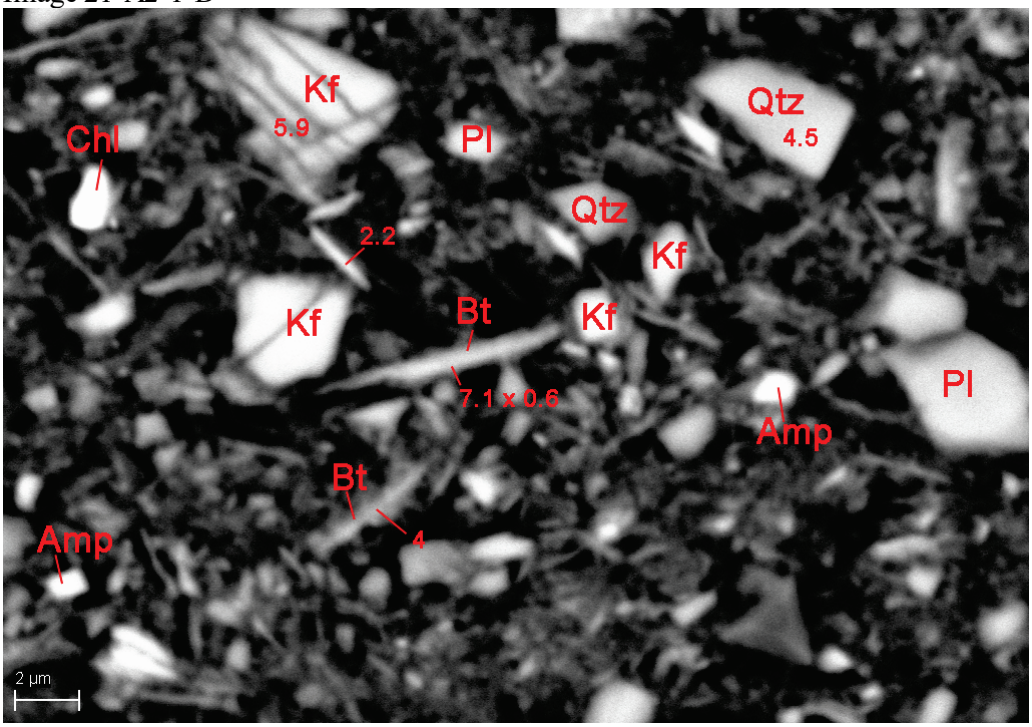

Figure A-34. BSE micrograph showing detail of dark laminae boxed in Figure A-33, composed largely of matrix material. Larger grains are fine to very fine silt (lengths shown in µm) (Am=amphibole, Bt=biotite, Chl=chlorite, Kf=potassium feldspar, Pl=plagioclase, Qtz=quartz).

Image 21-B1-2-A

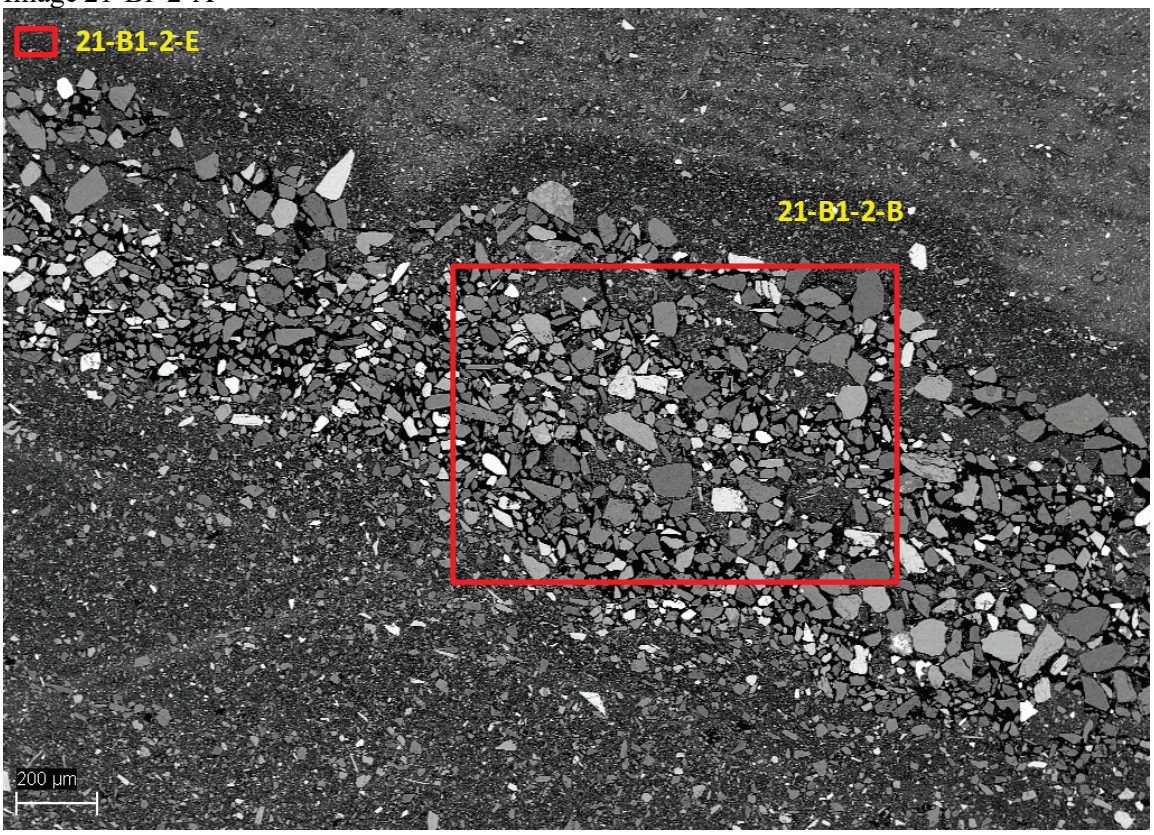

Figure A-35. BSE micrograph showing a coarse band within a finer-grained matrix.

Image 21-B1-2-B

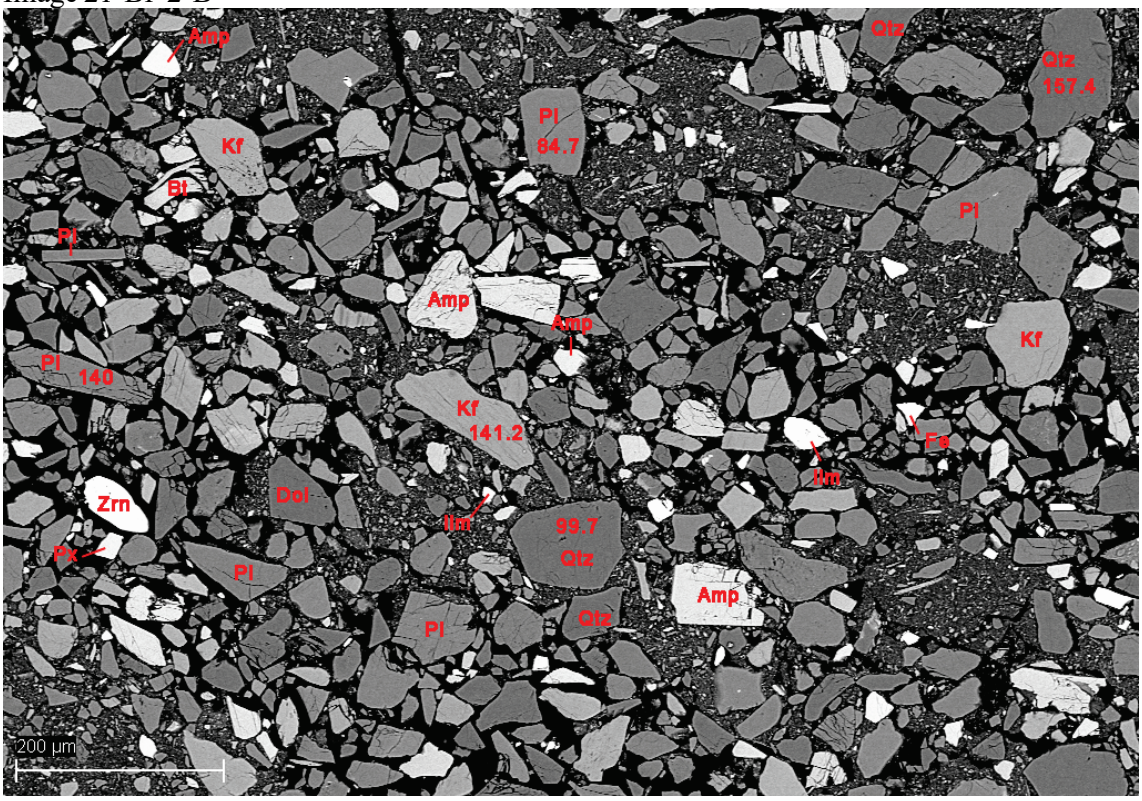

Figure A-36. BSE micrograph showing detail of larger boxed area in Figure A-35. The clast-supported lamina contains angular to sub-angular grains that are up to fine sand-size. Numbers on selected grains represent grain lengths in µm (Am=amphibole, Dol=dolomite, Fe=iron oxide, Ilm=ilmenite, Kf=potassium feldspar, Pl=plagioclase, Px=pyroxene, Qtz=quartz, Zrn=zircon).

Image 21-B1-2-E

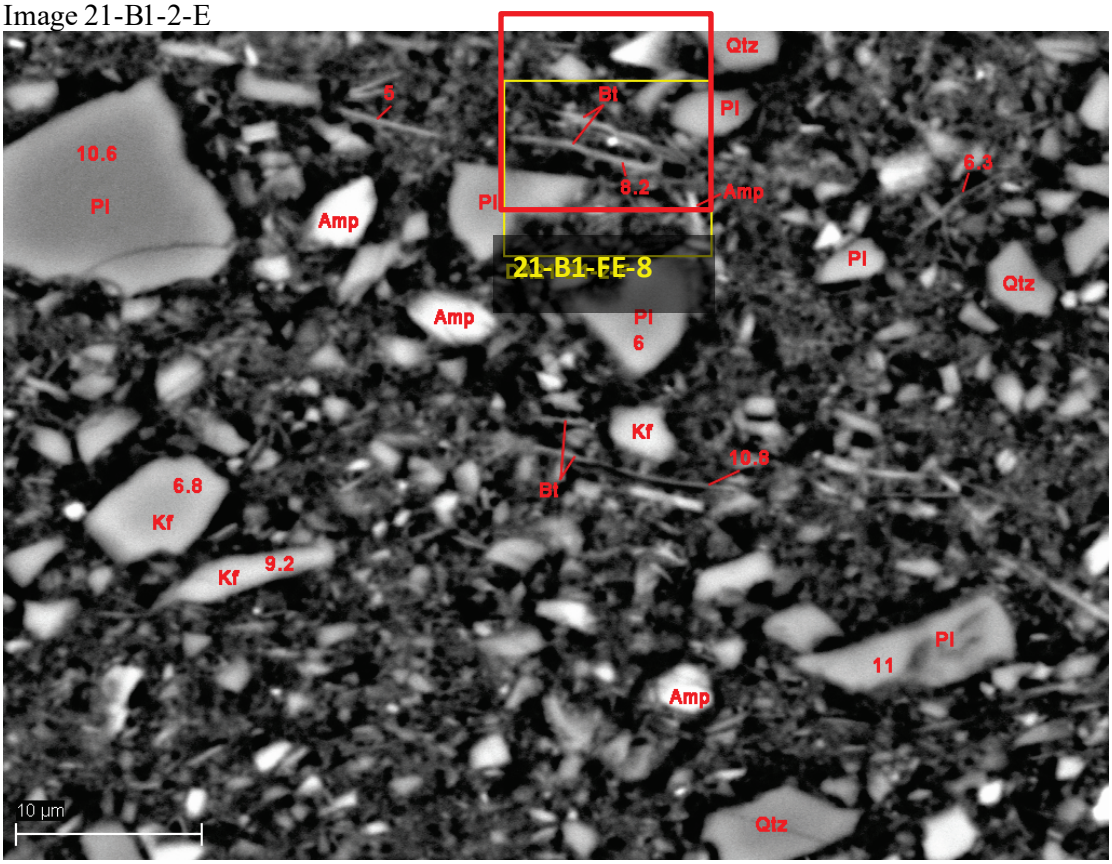

Figure A-37. BSE micrograph of smaller area boxed in Figure A-35, showing matrix around coarse lamina. Numbers on selected grains represent lengths in µm (Am=amphibole, Kf=potassium feldspar, Pl=plagioclase, Qtz=quartz).

Image 21-B1-FE-8

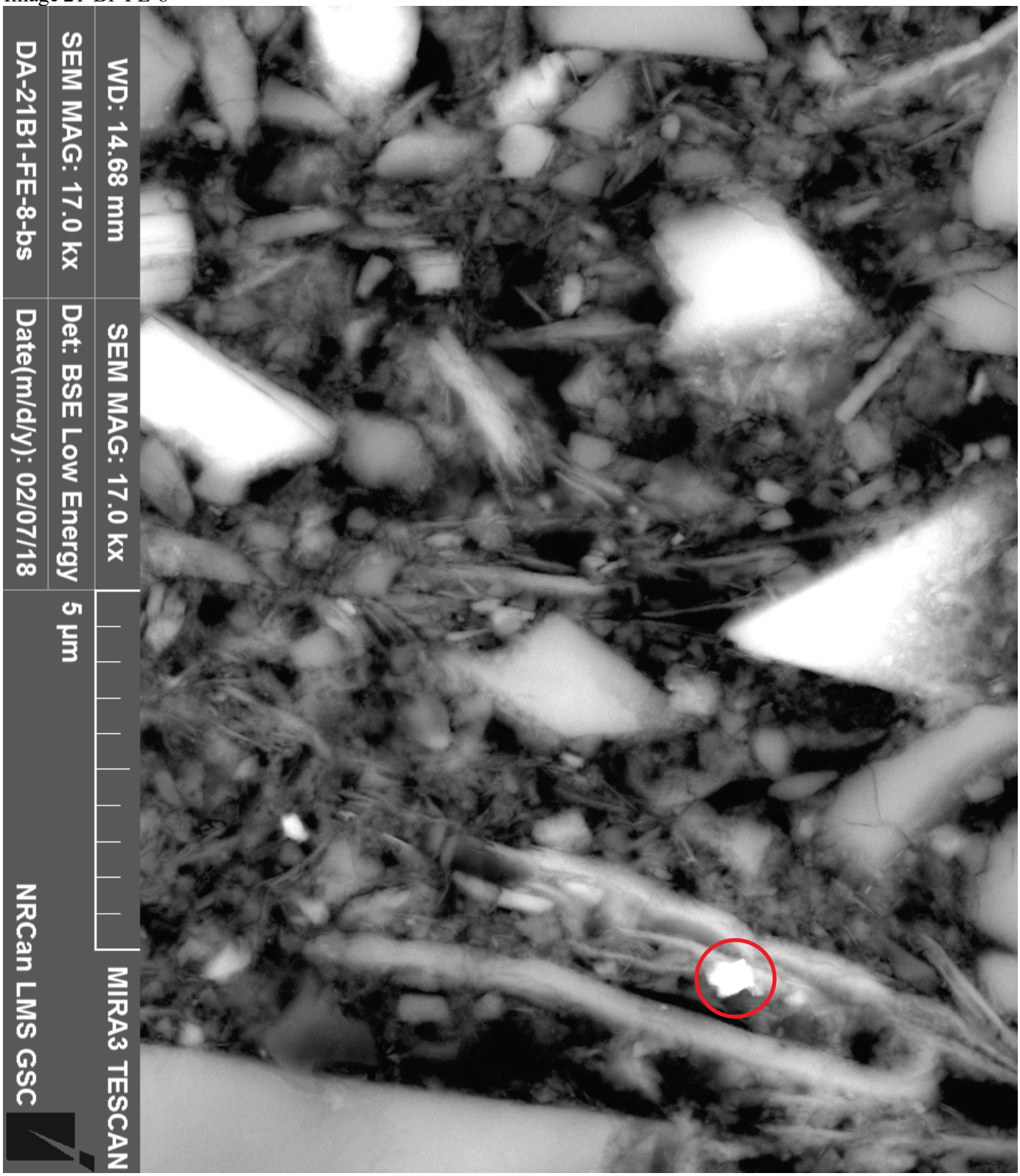

Figure A-38. BSE-FE micrograph of area boxed in Figure A-37. Circled grain between two biotite grains is a clay-size iron oxide mineral. Image is rotated to show the upward direction.

Image 21-B1-1-A

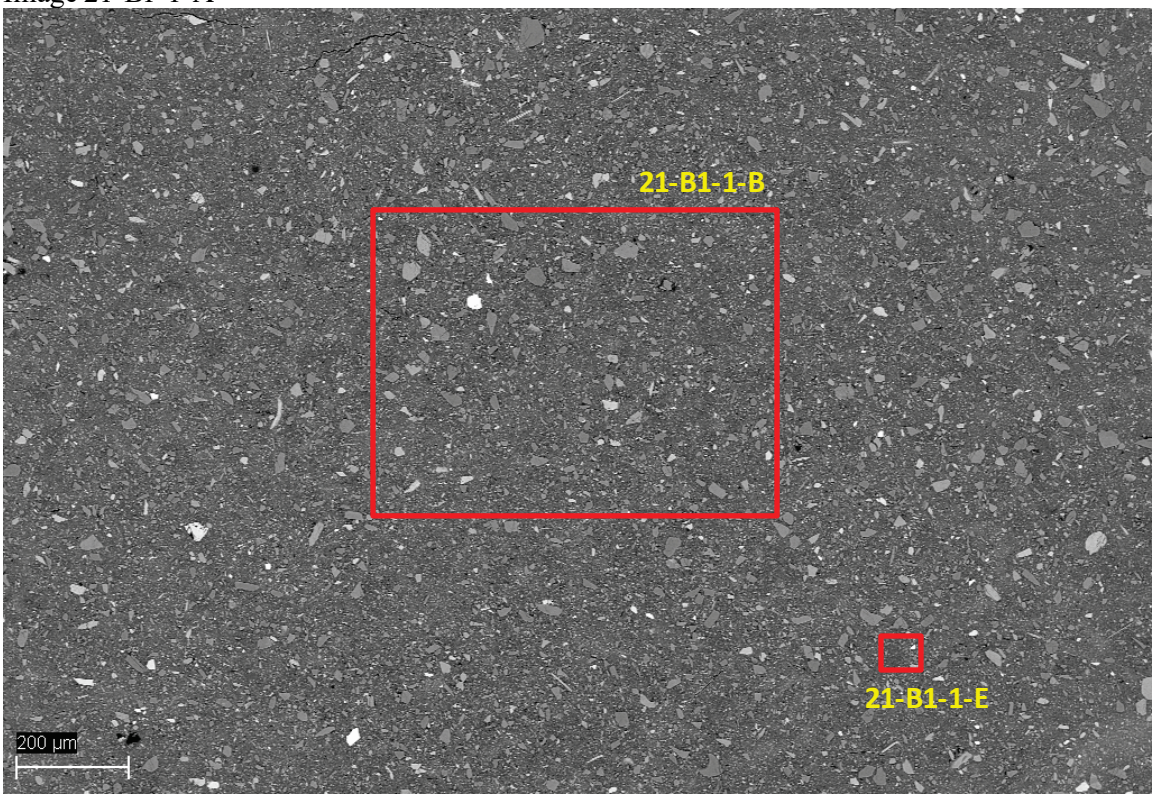

Figure A-39. BSE micrograph showing massive texture, without visible banding or lenses.

Image 21-B1-1-B

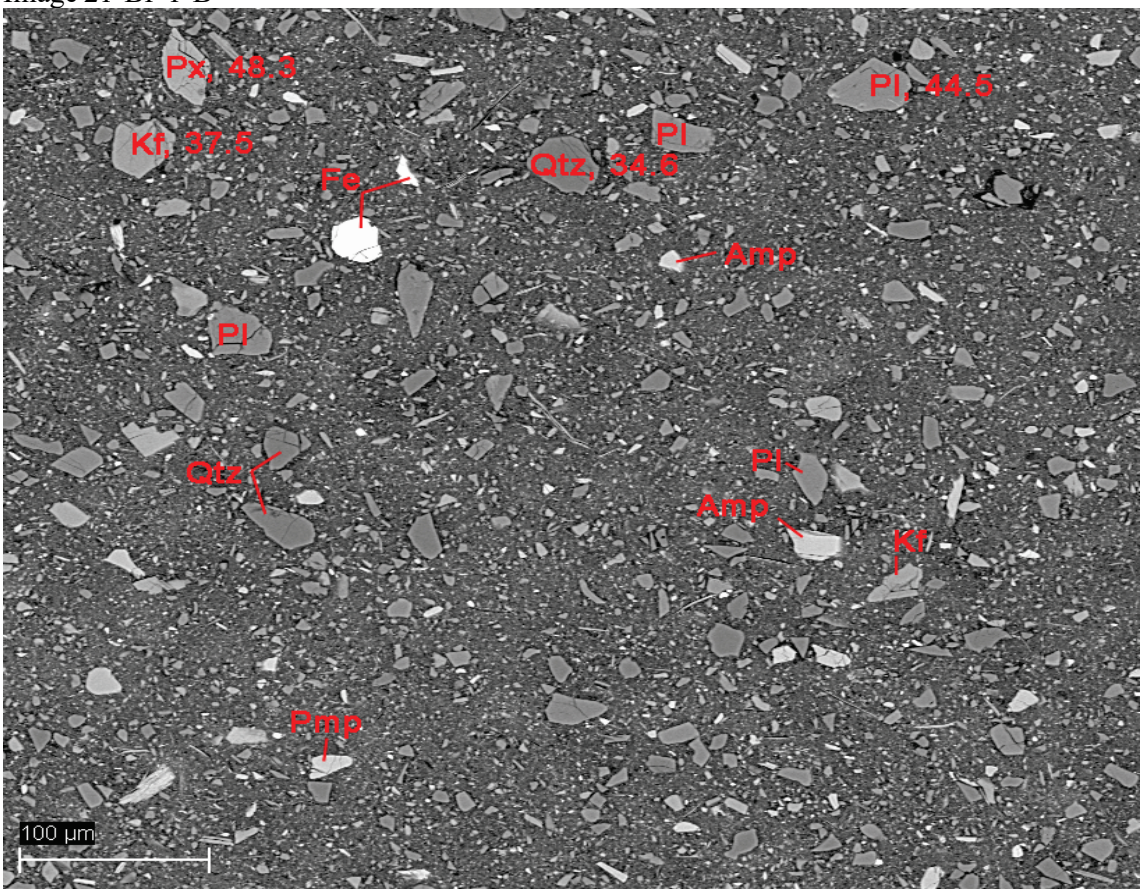

Figure A-40. BSE micrograph of area boxed in Figure A-39 showing random orientation of angular to sub-angular silt-size clasts (Amp=amphibole, Pmp=pumpellyite(?) – an epidote-group mineral, Fe=iron oxide, Kf=potassium feldspar, Pl=plagioclase, Px=pyroxene, Qtz=quartz).

Image 21-B1-1-E

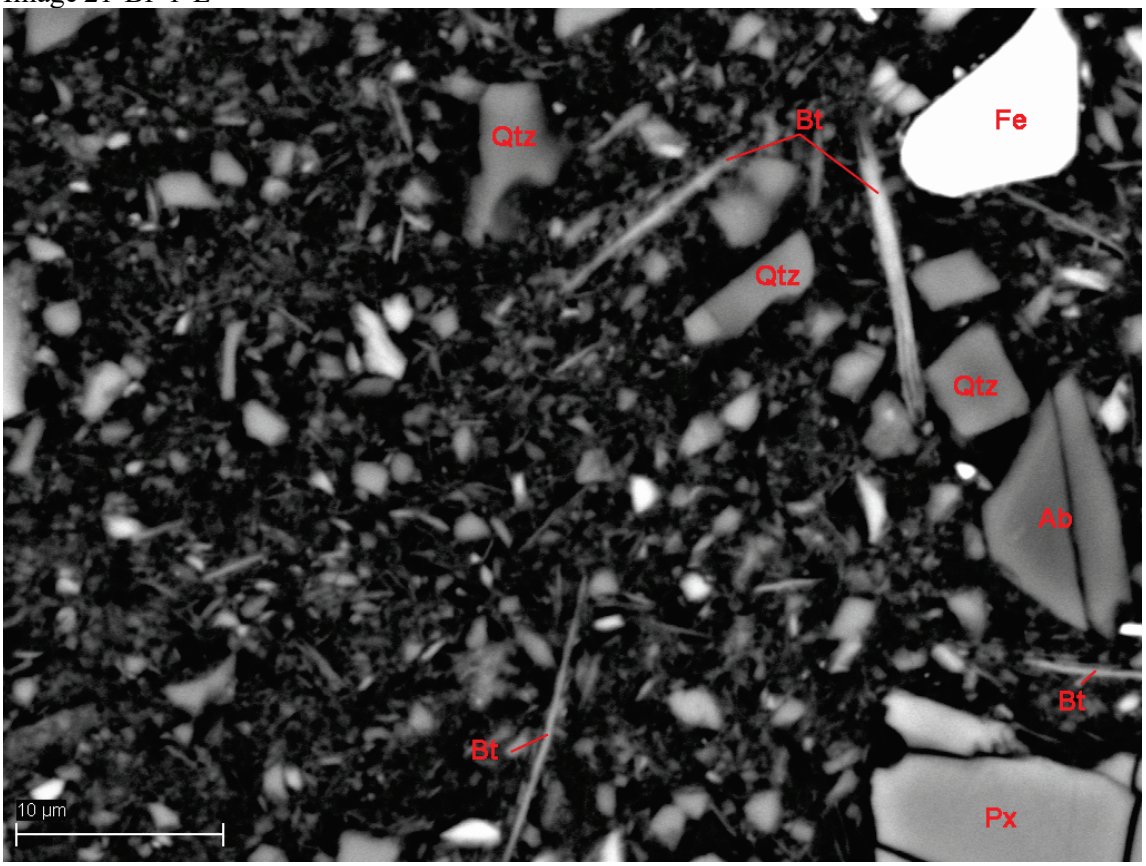

Figure A-41. BSE micrograph of matrix boxed in Figure A-39. Silt- and clay-size grains appear randomly-oriented (Ab=albite, Bt=biotite, Fe=iron oxide, Px=pyroxene, Qtz=quartz).

Image 21-A1-biotite

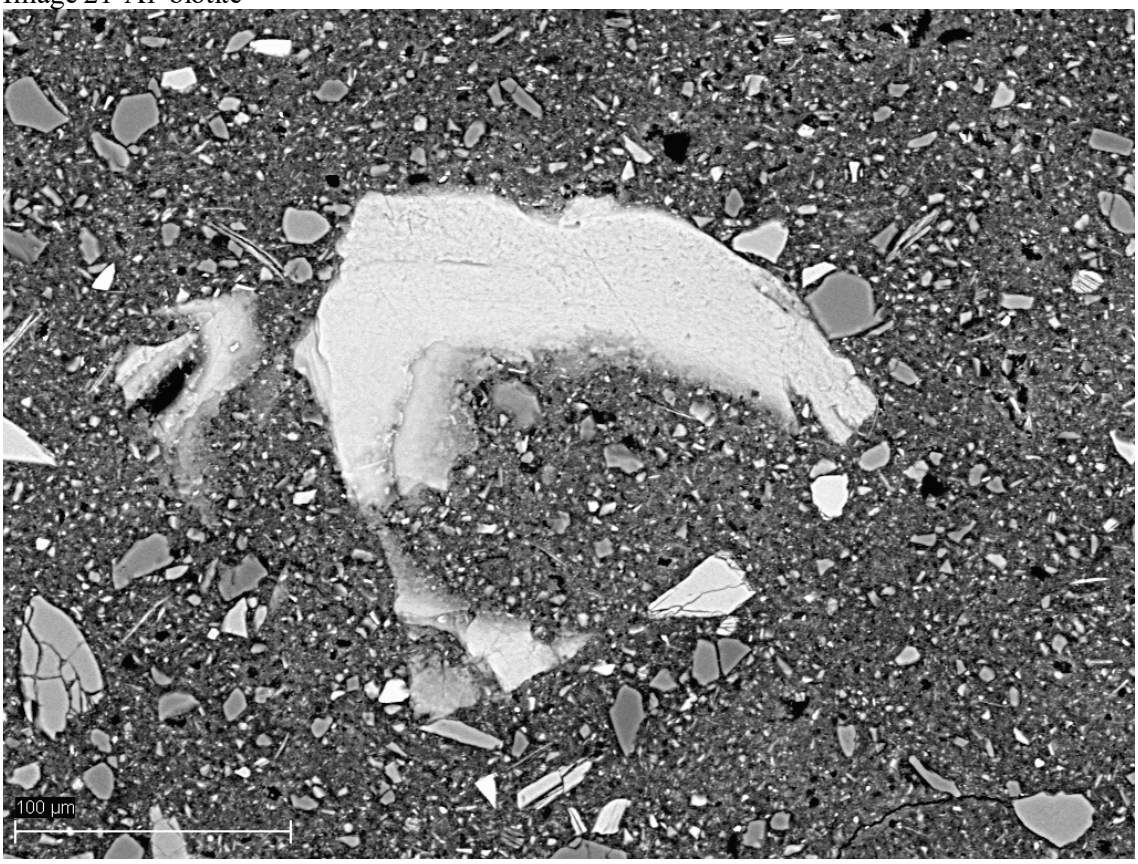

Figure A-42. BSE micrograph showing fine sand-size, detrital biotite grain.

Image 21-B2-1-A

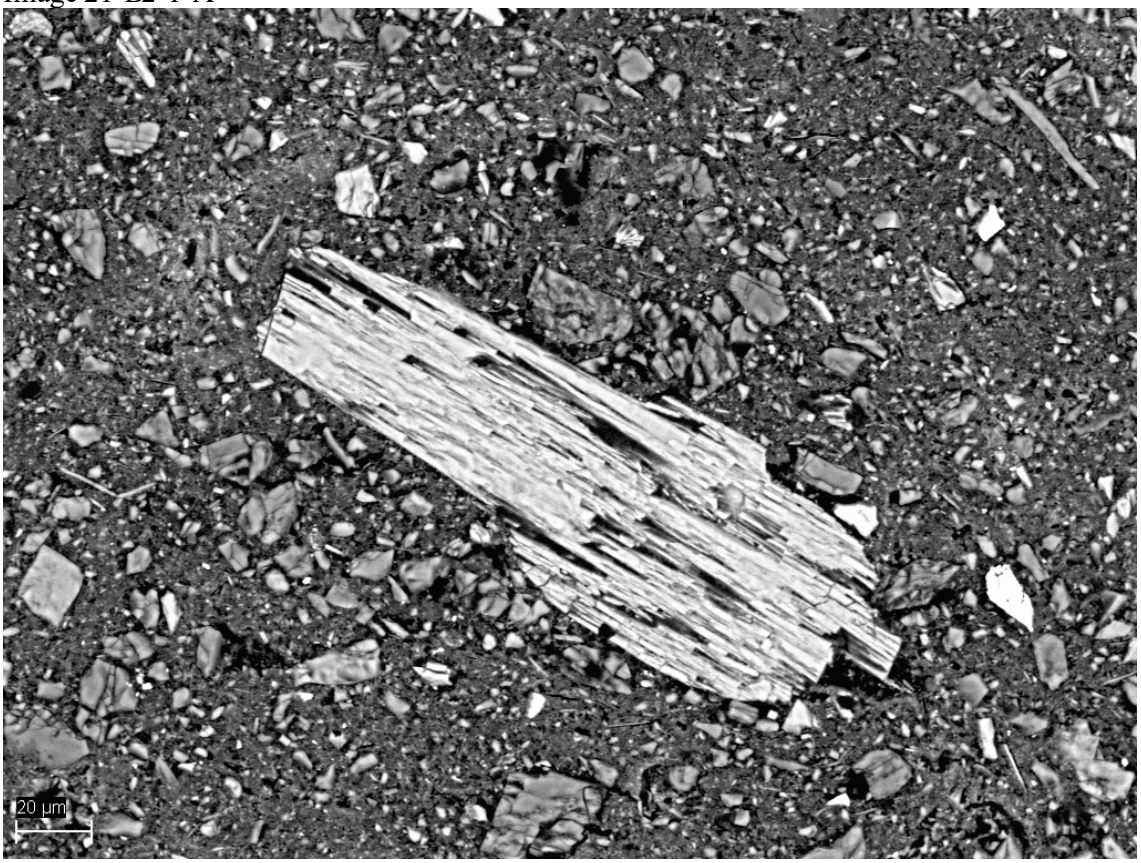

Figure A-43. BSE micrograph showing fine sand-size, detrital amphibole grain.

Image 21-B1-FE-1

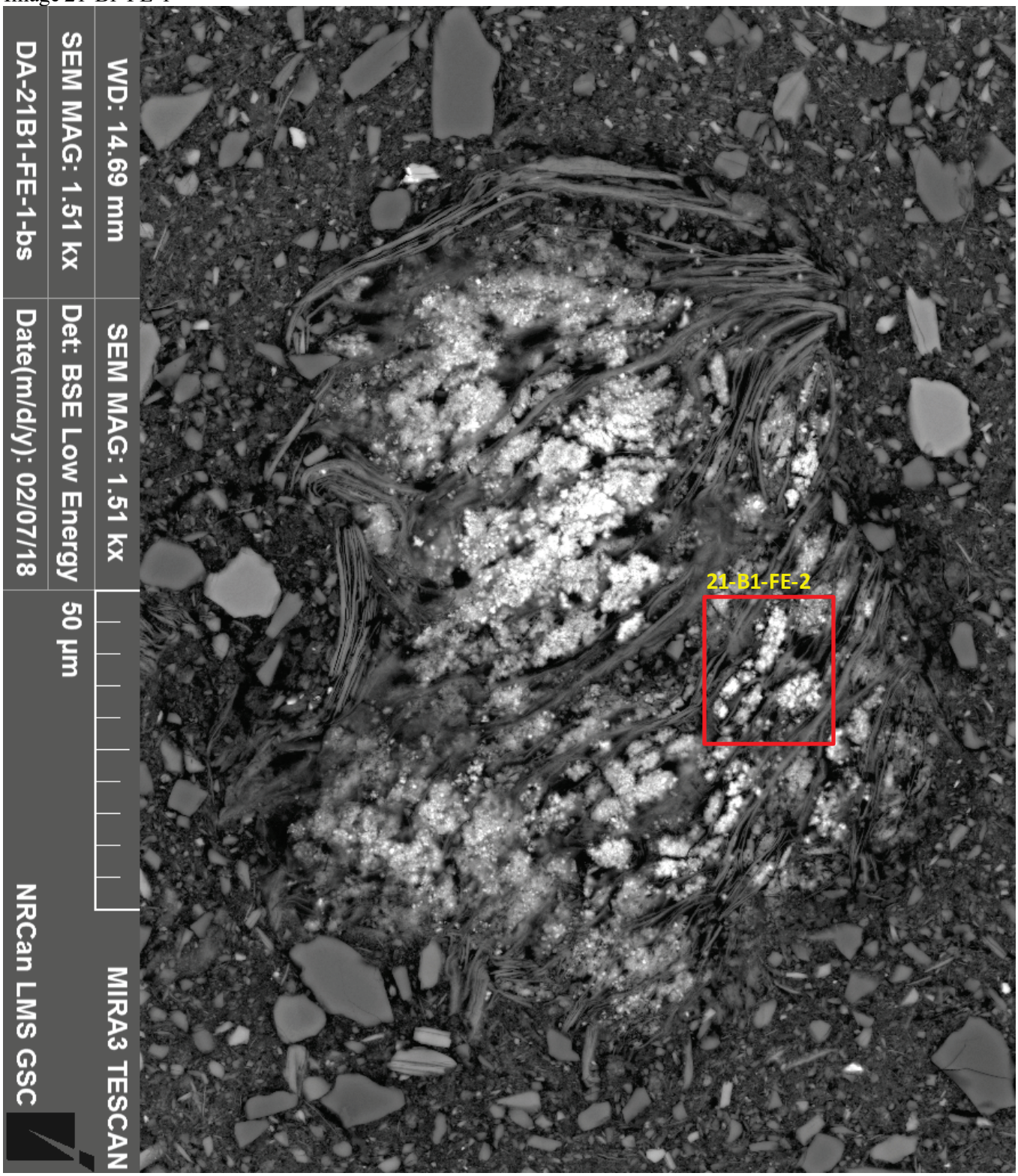

Figure A-44. BSE-FE micrograph showing iron sulfide crystals within chlorite grains. Image is rotated to show the upward direction.

Image 21-B1-FE-2

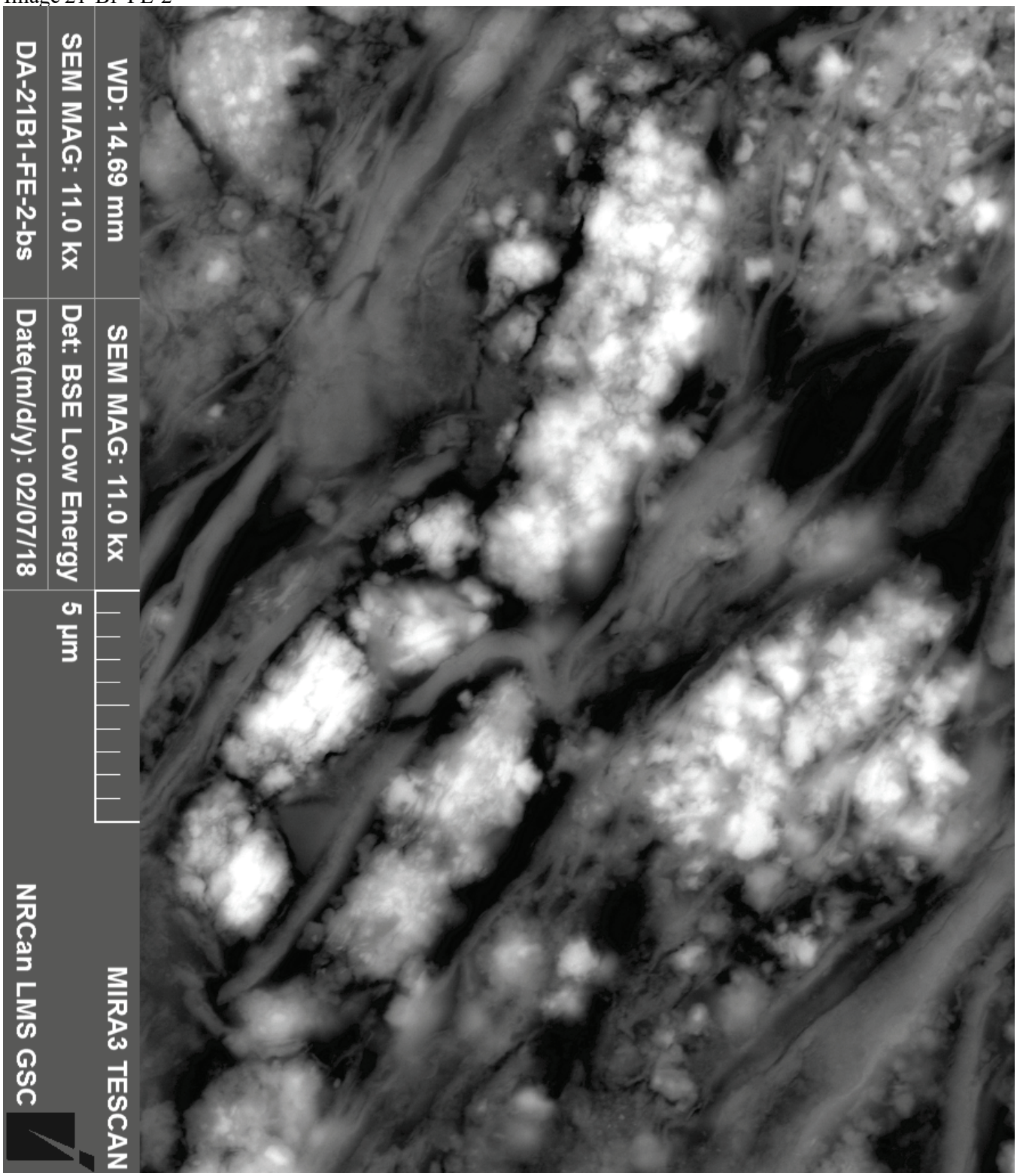

Figure A-45. BSE-FE micrograph showing detail of area boxed in Figure A-44. Image is rotated to show the upward direction.

Image 21-B1-FE-3

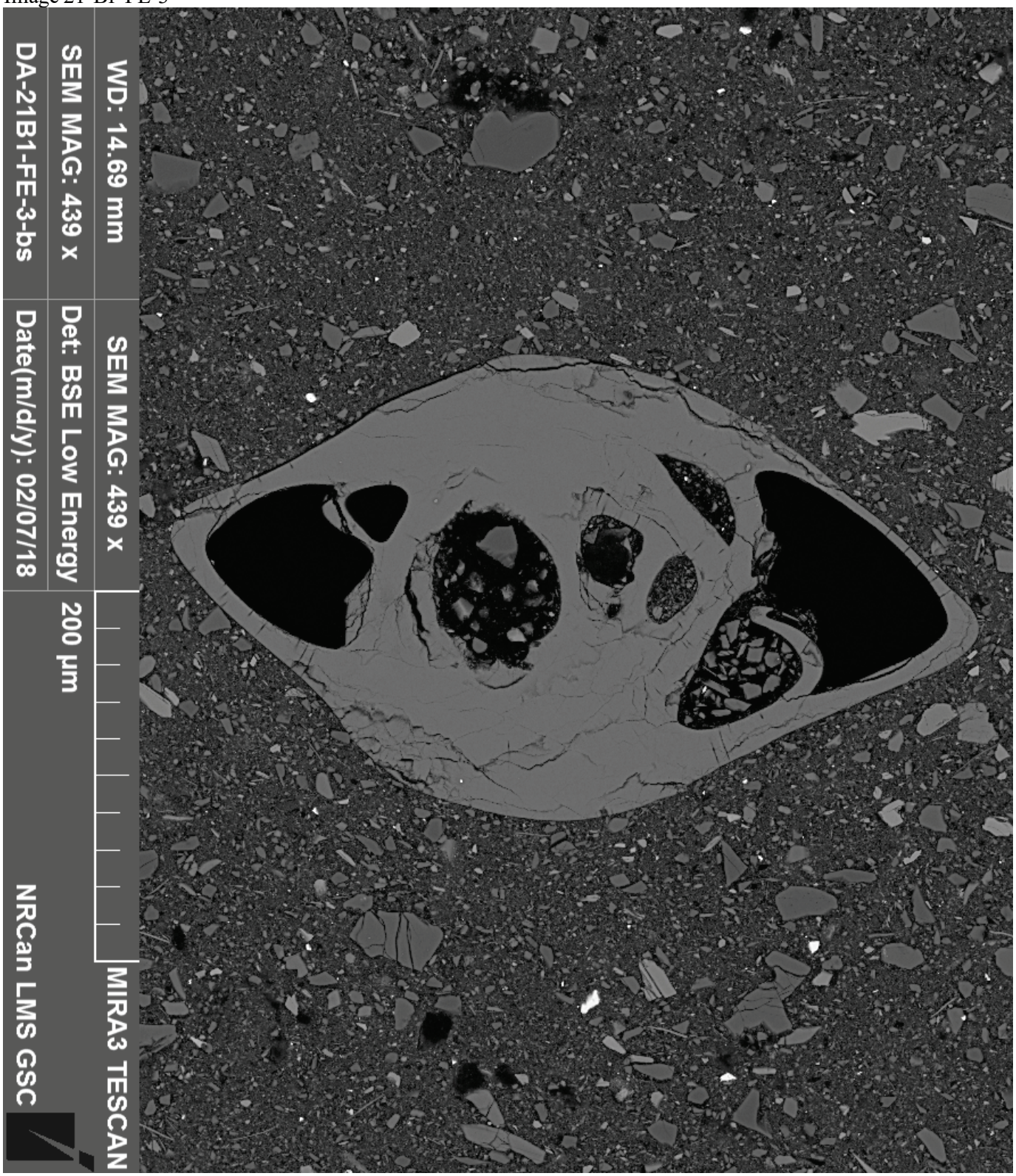

Figure A-46. BSE-FE micrograph showing calcite grain (shell fragment) containing silt- and clay-size infill. Image is rotated to show the upward direction.

Grain Mount Image 21-2

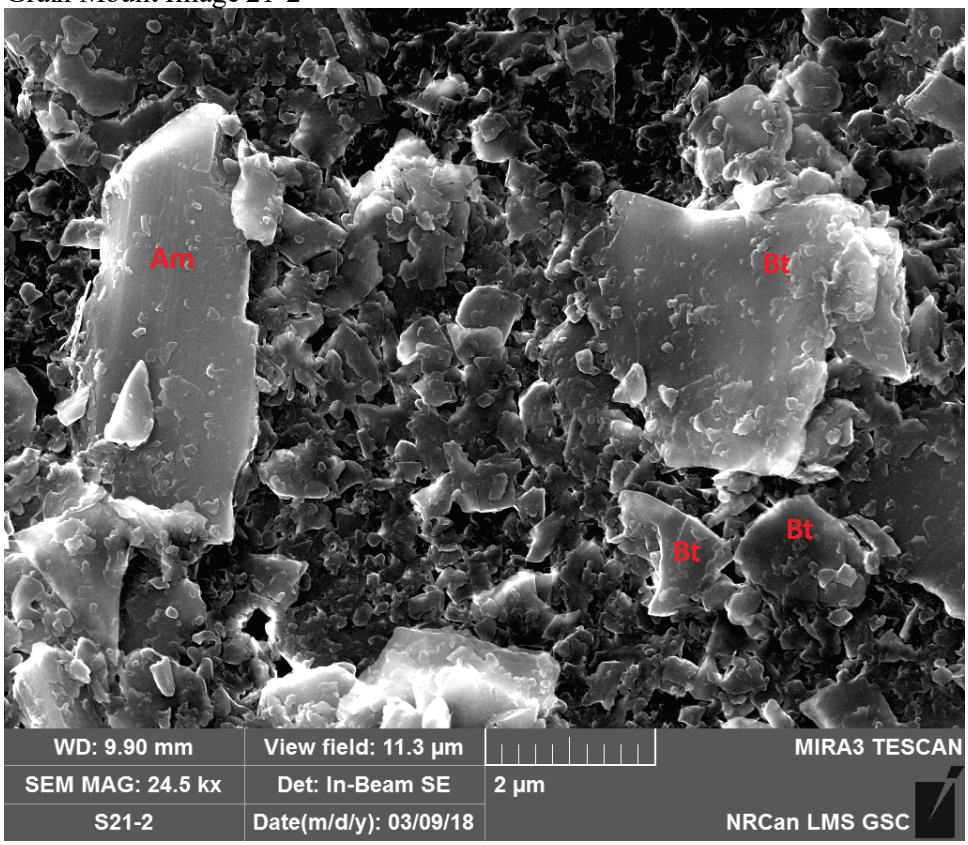

Figure A-47. BSE-FE micrograph of grain mount (unoriented) showing fine silt-size grains of amphibole (Am) and biotite (Bt) coated with clay-size platelets.

Grain Mount Image 21-8

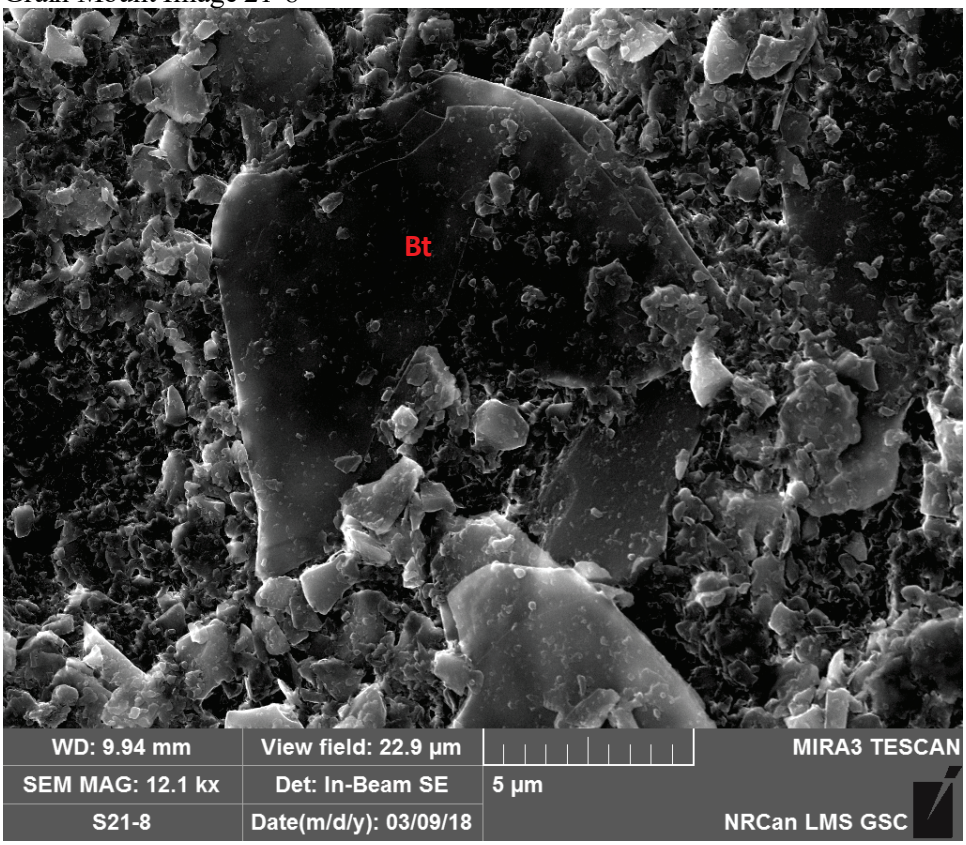

Figure A-48. BSE-FE micrograph of grain mount (unoriented) showing silt-size biotite (Bt) grain with flaking clay-size biotite platelets.